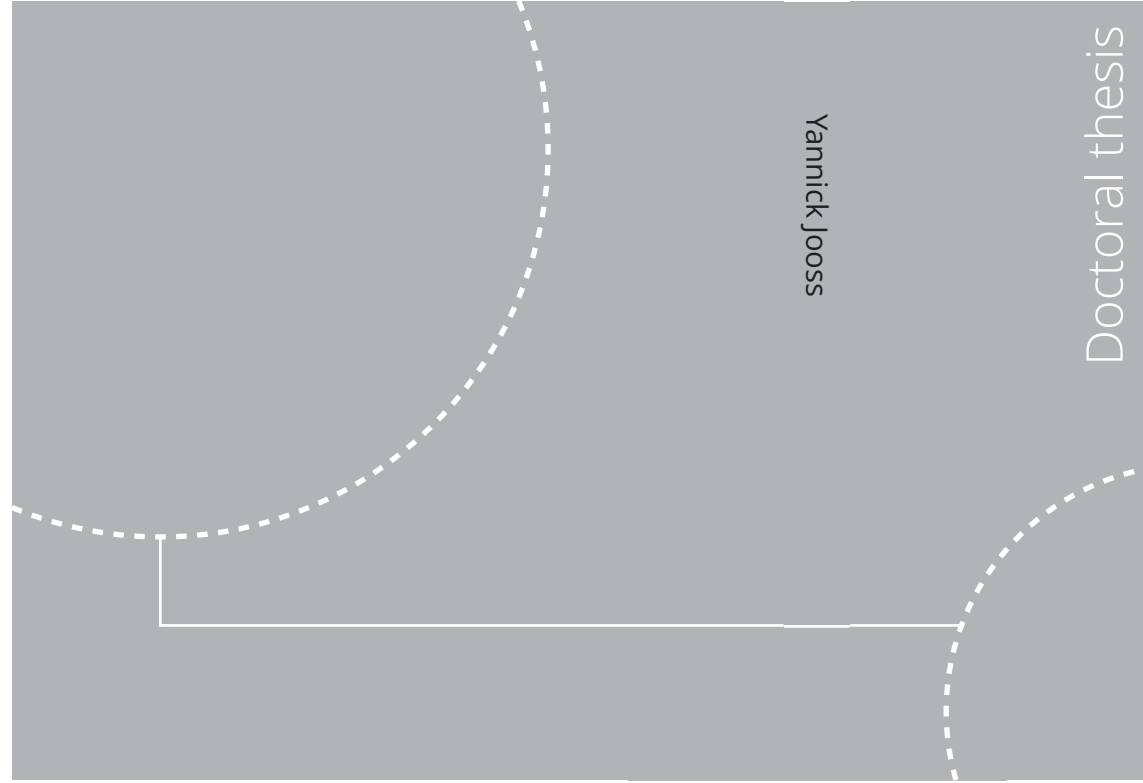


ISBN 978-82-326-6089-6 (printed ver.)
ISBN 978-82-326-6717-8 (electronic ver.)
ISSN 1503-8181 (printed ver.)
ISSN 2703-8084 (electronic ver.)



Doctoral theses at NTNU, 2022:283

Yannick Jooss

A fluid mechanic view on urban
wind energy

Doctoral theses at NTNU, 2022:283

NTNU
Norwegian University of
Science and Technology
Thesis for the degree of
Philosophiae Doctor
Faculty of Engineering
Department of Energy and Process Engineering

 **NTNU**
Norwegian University of
Science and Technology

 NTNU

 **NTNU**
Norwegian University of
Science and Technology

Yannick Jooss

A fluid mechanic view on urban wind energy

Thesis for the degree of Philosophiae Doctor

Trondheim, September 2022

Norwegian University of Science and Technology
Faculty of Engineering
Department of Energy and Process Engineering



Norwegian University of
Science and Technology

NTNU

Norwegian University of Science and Technology

Thesis for the degree of Philosophiae Doctor

Faculty of Engineering

Department of Energy and Process Engineering

© Yannick Jooss

ISBN 978-82-326-6089-6 (printed ver.)

ISBN 978-82-326-6717-8 (electronic ver.)

ISSN 1503-8181 (printed ver.)

ISSN 2703-8084 (electronic ver.)

Doctoral theses at NTNU, 2022:283



Printed by Skipnes Kommunikasjon AS

Abstract

The world energy demand is rising with an increasing need for renewable and sustainable energy sources. Wind energy plays a key role in this transition. Urban areas are largely unexploited for wind energy extraction. Urban wind energy offers great potential as a decentralized renewable energy source. However, one of the main issues to date is a limited understanding of the urban wind resources. The flow in an urban environment is naturally sheared, as part of the atmospheric boundary layer, and in addition, highly turbulent, due to the many obstructions in the flow. This thesis aims to contribute to an improved understanding of the urban wind resources. Specifically, the performance and flow field of a roof-mounted vertical axis wind turbine is examined, as well as the interaction of freestream turbulence and a turbulent boundary layer.

The thesis presents experimental work in which these problems are investigated on a lab-scale. Experiments are conducted in a wind tunnel and a water channel, enabling controlled flow conditions. Specific parameters in the flow, such as turbulence intensity and velocity shear, are deliberately varied using active grids. The flow is primarily evaluated with Particle Image Velocimetry and Laser Doppler Velocimetry, complemented by Constant Temperature Anemometry and surface pressure measurements. Two model buildings are placed in the flow, represented by surface-mounted cubes. A drag-driven vertical axis wind turbine of the Savonius type is positioned on the roof of the model buildings and its power output is measured. Both the streamwise position and the height of the turbine above the roof are varied, and the impact on the flow field and power output is assessed. In addition, the influence of varying wind directions and vertically sheared inflow on the turbine performance are examined. The influence of turbulence intensity is

investigated fundamentally on the evolution of a turbulent boundary layer and on the flow around the model buildings. Again, the impact on the turbine's power output at various positions is evaluated.

It is demonstrated that a turbulent boundary layer is not permanently matured ahead of its natural evolution by the presence of freestream turbulence and that the relative state of evolution of both the boundary layer and the freestream turbulence has to be considered when assessing the turbulent boundary layer. A key finding is the substantial impact of a roof-mounted wind turbine on the flow field and, thus, on the available power. This suggests that in contrast to common practice, including an actual turbine in the analysis is significant. A central high turbine position is found to maximize the power output for a uniform wind rose. However, for individual wind directions, the ideal turbine position and height vary. Turbulence intensity has a significant impact on the flow around the model buildings and consequently also on the power output of the turbine. High levels of turbulence intensity reduce flow separation on top of the building, resulting in higher velocities where the turbine is placed and, thus, higher power output. Conversely, velocity shear has only limited influence on the flow field and power output of the roof-mounted turbine. Overall, a methodology to assess a roof-mounted vertical axis wind turbine in a controlled environment was developed, examining the influence of various parameters, such as inflow conditions and turbine position.

Preface

This thesis is submitted to the Norwegian University of Science and Technology (NTNU) for partial fulfilment of the requirements for the degree of philosophiae doctor. The doctoral work has been carried out in the Thermo Fluids Group at the Department of Energy and Process Engineering (EPT) from February 2019 to July 2022. The work has been supervised by Tania Bracchi and co-supervised by R. Jason Hearst.

The research was funded by the Department of Energy & Process Engineering at NTNU.

The thesis is made up of three chapters and four scientific papers. The first two chapters introduce the research topic, relevant literature and the experimental methodology as well as motivate the study. The research articles are summarized in chapter three and are included in full text at the end of the thesis.

Article I

Spatial development of a turbulent boundary layer subjected to freestream turbulence

Yannick Jooss, Leon Li, Tania Bracchi and R. Jason Hearst

Journal of Fluid Mechanics, **911**, A4, (2021)

<https://doi.org/10.1017/jfm.2020.967>

Authors' contributions: Y.J. and R.J.H. created the research plan. Y.J. and L.L. designed and built the set-up and conducted all experiments. Y.J. performed the analysis and wrote the manuscript. All authors contributed to the editing of the manuscript.

*Article II***Flow field and performance of a vertical axis wind turbine on model buildings**

Yannick Jooss, Roberto Bolis, Tania Bracchi and R. Jason Hearst
Flow, **2**, E10, (2022)

<https://doi.org/10.1017/flo.2022.3>

Authors' contributions: Y.J., T.B. and R.J.H. created the research plan. Y.J. and R.B. designed and built the set-up and conducted all experiments. Y.J. performed the analysis and wrote the manuscript. All authors contributed to the editing of the manuscript.

*Article III***Influence of position and wind direction on the performance of a roof-mounted vertical axis wind turbine**

Yannick Jooss, Eivind Berg Rønning, R. Jason Hearst and Tania Bracchi
Under consideration for publication in *Journal of Wind Engineering & Industrial Aerodynamics*

Authors' contributions: Y.J., R.J.H. and T.B. created the research plan. Y.J. and E.B.R. designed and built the set-up and conducted all experiments. Y.J. performed the analysis and wrote the manuscript. All authors contributed to the editing of the manuscript.

*Article IV***Influence of incoming turbulence and shear on the flow field and performance of a lab-scale roof-mounted vertical axis wind turbine**

Yannick Jooss, R. Jason Hearst and Tania Bracchi
Under consideration for publication in *Wind Energy*

Authors' contributions: Y.J., R.J.H. and T.B. created the research plan. Y.J. designed and built the set-up and conducted all experiments. Y.J. performed the analysis and wrote the manuscript. All authors contributed to the editing of the manuscript.

Additional abstracts and conference presentations not formally included in the thesis:

Evaluation of an urban environment regarding the potential placement of wind turbines

Yannick Jooss, Are Simonsen, Simen Havneraas Røstum, Lars Roar Sætran, R. Jason Hearst and Tania Bracchi

15th EAWE PhD Seminar, Nantes, France, October 2019

Development of a turbulent boundary layer subjected to free-stream turbulence

Yannick Jooss, Leon Li, Tania Bracchi and R. Jason Hearst

72nd American Physical Society Division of Fluid Dynamics Meeting, Seattle, United States, November 2019

Wind field and performance measurements of vertical axis wind turbines on modeled buildings

Yannick Jooss, Roberto Bolis, Tania Bracchi and R. Jason Hearst

Wind Energy Science Conference, Hannover, Germany, May 2021

Acknowledgements

This journey is coming to an end, and it would not have been possible without the help of the people around me. This is to thank them.

First and foremost, I want to thank my supervisors, Tania Bracchi and R. Jason Hearst. Tania, thank you for being the most supportive and kind supervisor one can hope for. Thank you for your guidance and your expertise. Thank you for always believing in me. Jason, thank you for simply being the best and most caring co-supervisor. Thank you for taking me into your group. Thank you for teaching me so much. I am truly grateful to have had two great mentors on my side and, even more important, two great human beings.

A big thank you to the Experimental Fluids Group I had the privilege to be a part of. The way we support each other is special, and I learned so much from each of you. Equally important to me was the amount of fun we had together at work and off, ~~screwing up~~ figuring things out in the lab together, all the tea breaks and the friendly competitions (apologies to everyone I crashed into go-karting). Mamba out!

Thank you also to everyone else I crossed paths with at EPT and who helped me along the way, from technical and administrative staff to the master students that worked on the project with me. This goes especially to the PhDs and Postdocs of the Thermofluids group. Some of which have become close friends over the years (or instantly). Thank you for all the fun lunches, tea breaks, skiing trips, hiking trips, football matches, ping pong matches, dinners, beers and all the other adventures. *All we have to decide is what to do with the time that is given to us.* I loved spending these last three and a half years with you. Chans on me!

I also want to thank my friends and family. Thank you to all my long-time friends from Germany and elsewhere. I am very happy to have each of you in my life. A special thank you to my parents. Without you, none of this would have been possible. Your ever-present support, encouragement and your unconditional love are what got me here.

Finally, I want to thank Clara. Thank you for always being there for me. Thank you for cheering me up when I am down. Thank you for your loyalty and your love. Having you by my side makes life so much easier and so much more fun.

Contents

Abstract	iii
Preface	iv
Acknowledgements	vii
Contents	x
1 Introduction	1
1.1 Motivation	1
1.2 Background	2
1.2.1 Wind turbines	2
1.2.2 Urban wind energy	6
1.2.3 Turbulence and shear	13
1.3 Objectives	22
2 Experimental Methods	25
2.1 Facilities	25
2.2 Active grids	27

2.3	Building and turbine set-up	29
2.4	Power measurements	32
2.5	Flow measurements	35
2.5.1	Particle Image Velocimetry	36
2.5.2	Laser Doppler Velocimetry	38
2.5.3	Constant temperature anemometry	42
2.5.4	Surface pressure measurements	43
3	Summaries of the research articles and future work	45
3.1	Summaries of the articles	45
3.2	Future work	49
	Bibliography	50
	<i>Article I: Spatial development of a turbulent boundary layer subjected to freestream turbulence</i>	69
	<i>Article II: Flow field and performance of a vertical axis wind turbine on model buildings</i>	99
	<i>Article III: Influence of position and wind direction on the performance of a roof-mounted vertical axis wind turbine</i>	121
	<i>Article IV: Influence of incoming turbulence and shear on the flow field and performance of a lab-scale roof-mounted vertical axis wind turbine</i>	141

Chapter 1

Introduction

1.1 Motivation

The energy demand is rising worldwide (IEA, 2020). At the same time, we are facing one of the largest crises in the history of humankind in climate change (IPCC, 2021). Nations worldwide agreed to limit global warming and mitigate its consequences (UNFCCC, 2015). A key to this is the transition to renewable energies (Chang et al., 2017) with the goal to reach a fully renewable supply of energy desirably by mid-century (REN21, 2022). Wind and solar energy are already large contributors, with a global share of 10% together in 2021 (REN21, 2022), which is expected to increase to 30% by 2030 (IEA, 2020). Wind power alone has increased its global capacity by a factor of 3.5 within ten years from 2011 to 2021 (REN21, 2022) and is expected to continue growing substantially (Porté-Agel et al., 2020). It is an attractive source of energy primarily due to its low life-cycle emissions (Veers et al., 2019). In addition, wind energy has reached the status as one of the cheapest technologies for new power plants (REN21, 2017).

Wind turbines have grown in average size over the years (Molina and Enrique Mercado, 2011) and have, in turn, often moved far away from inhabited areas where a big part of the energy is consumed. Thus, approximately 15% to 20% of the construction costs come from transmission infrastructure (Mills et al., 2012). These costs can be reduced with more decentralized energy generation, which offers the potential of clean, reliable and cost-effective energy (Akinyele et al., 2014). With the growing availability of renewable energy systems, urban areas become increasingly relevant as sites of energy generation (Adil and Ko, 2016). Urban energy systems can be

integrated into microgrids as a key component of future smart grids (Laseter, 2011; Karabiber et al., 2013). Thus far, the focus has primarily been on solar energy generation in this context, but in principle, the same can be applied to biomass and on-site micro wind generation once they are widespread in urban environments (Adil and Ko, 2016). Small wind turbines are well suited for placement on or around buildings (KC et al., 2019) and thus offer a great opportunity to include urban wind energy as an additional decentralized renewable energy source (Ataei et al., 2015). However, to date, urban wind power is still only sparsely utilised, even though the yearly installed capacity of small wind turbines has grown continuously in recent years (Pitteloud and Gsänger, 2016).

Widely regarded as the key factor impeding a wider use of urban wind energy is a limited understanding of urban wind resources (Toja-Silva et al., 2015; Stathopoulos et al., 2018; KC et al., 2019; Rezaeiha et al., 2020). The mean wind speeds are generally low with high levels of turbulence intensity (Kooiman and Tullis, 2010). However, regions with high velocities exist locally as well (Stathopoulos et al., 2018). The big variability in wind velocities makes a proper assessment of the urban wind resources even more important. A better understanding of wind flows in complex terrain is identified as one of the grand challenges in wind energy today (Veers et al., 2019). This thesis aims to contribute to that by studying urban wind energy from a fluid mechanic perspective. Urban flows are studied with a particular focus on the wind resource assessment of a roof-mounted vertical axis wind turbine.

1.2 Background

This section provides background information to the articles presented in this thesis. Specifically, basic concepts of wind energy, urban wind energy, and sheared flow subjected to turbulence are introduced.

1.2.1 Wind turbines

Extracting energy from the wind is a technology that has existed for centuries. The first windmills were built more than 1000 years ago, with the purpose of directly powering simple mechanical tasks typically related to agriculture, such as grinding grain or water pumping (Fleming and Probert, 1984). An early example of this from Persia is displayed in figure 1.1.



Figure 1.1: Early windmills from Nashtifan on top of buildings (Firouzi and Firouzi, 2005).

Basic principles

Since then, the technology has evolved and wind energy has become a mainstream source of energy. Wind turbines today convert the energy in the wind to electricity on a large scale, employing electrical generators. The available power in the wind, P_a (W), is defined as:

$$P_a = \frac{1}{2} \rho U^3 A, \quad (1.1)$$

with the wind velocity U (m/s), the rotor swept area A (m) and the density of the air ρ (kg/m³). Wind turbines are placed in the atmospheric boundary layer, where the flow velocity typically increases from the ground upwards. It is important to note that P_a , estimated from undisturbed flow, is not fully available for extraction. The wind turbine itself induces an upstream blockage effect on the flow that decreases the wind velocity and thus also P_a (Medici et al., 2011). In addition, only a fraction of the (reduced) available power in the wind is extracted by a wind turbine (Manwell et al., 2010). The ratio between the mechanical power of a wind turbine to the available power in the wind is expressed by the power coefficient:

$$C_P = \frac{P_m}{P_a}. \quad (1.2)$$

The mechanical power P_m (W) of a wind turbine is the power extracted from the wind by the wind turbine (Bastankhah and Porté-Agel, 2017):

$$P_m = Q\Omega_T, \quad (1.3)$$

where Q (Nm) is the mechanical torque of the turbine shaft and Ω_T (1/s) is the rotational frequency of the wind turbine. The power output of a wind turbine is generally evaluated by looking at power curves across the range of operation, i.e., C_P for different tip speed ratios:

$$\lambda = \frac{\Omega_T r_T}{U}, \quad (1.4)$$

with the turbine radius r_T (m). Today, the vast majority of installations are three-bladed horizontal axis wind turbines (HAWTs), where the blades rotate around a horizontal axis. Their main advantages are a low rotor solidity, which reduces material costs and a high average height of the rotor swept area above the ground (Manwell et al., 2010). In addition, the achieved C_P for three-bladed HAWTs is higher than for other turbine types (Eldridge, 1975).

Vertical axis wind turbines

The earliest devices extracting wind energy were spinning around the vertical axis (see figure 1.1). Vertical axis wind turbines (VAWTs) have historically had lower power coefficients than HAWTs, i.e., they have been less efficient in capturing the power in the wind (Eldridge, 1975). However, they have advantages that make them attractive for specific conditions, often in environments where HAWTs struggle, such as very high wind velocities, highly turbulent flow and rapidly changing wind directions (Aslam Bhutta et al., 2012). VAWTs are omnidirectional, i.e. they function independently of the wind direction (Manwell et al., 2010; Aslam Bhutta et al., 2012). Thus, there is no need for a yaw mechanism. This is especially advantageous in environments with fast-changing wind direction, for example, in complex terrain. Compared to HAWTs, a lower tower is required to access the same rotor swept area above the ground. In addition, it enables the drive train, including generator and gearbox, to be located close to or on the ground, where it can be maintained easily (Manwell et al., 2010). Altogether, this reduces structural loads (Aslam Bhutta et al., 2012). While there is limited variability in the design of HAWTs today, due to decades of optimization, there exist a variety of designs for VAWTs. The most common types are the Savonius and the Darrieus rotor, displayed in figure 1.2. Many other designs, some similar to the displayed, some very different, exist, see e.g. Ragheb (2011) and Aslam Bhutta et al. (2012).

VAWTs can be either lift- or drag-driven. Lift-driven VAWTs utilise lift-generating blades to drive the rotation of the turbine. The most widespread lift-driven VAWT is the Darrieus turbine invented by G. J. M. Darrieus

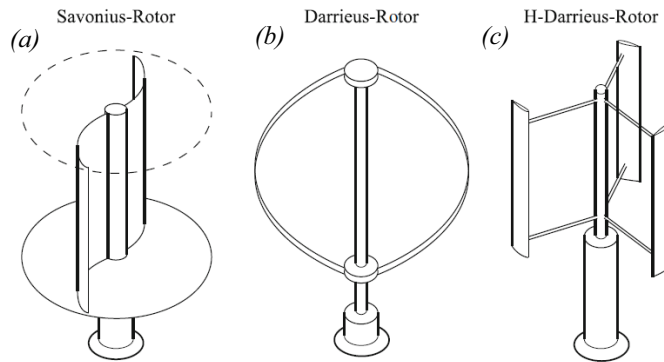


Figure 1.2: Most common types of vertical axis wind turbines (Schaffarczyk, 2014).

in 1931 (De Tavernier et al., 2020). The original design has a Φ -shaped rotor (figure 1.2 (b)). The advantage of this design is that only tension and no bending moments act on the blades (Manwell et al., 2010; De Tavernier et al., 2020). Later on, the H-type Darrieus turbine was developed (figure 1.2 (c)), which simplifies the incorporation of aerodynamic control mechanisms on the blades (Manwell et al., 2010). Many variations of these designs exist, with twisted blades, V-shaped rotors and plenty of other configurations (Manwell et al., 2010; De Tavernier et al., 2020).

The most widespread design for drag-driven VAWTs is the Savonius turbine (figure 1.2 (a)) by S. J. Savonius from 1922 (De Tavernier et al., 2020). In its simplest form, it consists of two semicircular profile buckets with opposing orientation on each side of the axis of rotation. This way, the wind generates a different drag force on the two buckets, which causes the turbine to rotate (Akwa et al., 2012; De Tavernier et al., 2020). The flow dynamics are visualized in figure 1.3. The power coefficient that Savonius turbines achieve is relatively low (Akwa et al., 2012; De Tavernier et al., 2020). Their main advantages lie in their simplicity, i.e., simple construction and, thus, low costs, as well as low angular velocities, and, thus, low noise levels and reduced wear on moving parts (Akwa et al., 2012). A wide range of configurations exists, with or without end plates, varying in the aspect ratio, number and shape of the blades and their relative position to each other (Alexander and Holownia, 1978; Akwa et al., 2012). Kumbernuss et al. (2012) showed that having the two buckets slightly overlapping (see figure 1.3) reduces the starting torque of the turbine. VAWTs generally have received increasing attention again in the context of wind farms (Whittlesey and Dabiri, 2010;

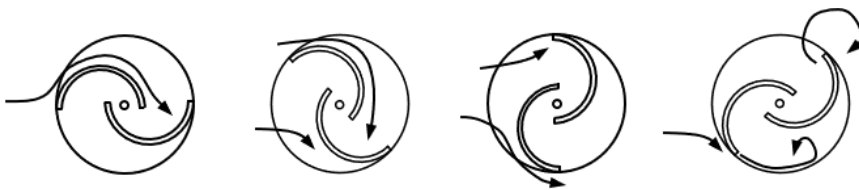


Figure 1.3: Flow around a Savonius rotor based on visualizations by Nakajima et al. (2008).

Dabiri, 2011), offshore floating wind turbines (Borg et al., 2014; Hand and Cashman, 2020) and especially urban wind energy (Kooiman and Tullis, 2010; Toja-Silva et al., 2013; Kumar et al., 2018).

1.2.2 Urban wind energy

Urban wind energy describes the utilization of wind power in urban and suburban areas or simply in the built environment (Stathopoulos et al., 2018). The first devices extracting kinetic energy from the wind were often installed on or around buildings (see figure 1.1). Back then, it was difficult to transmit energy over long distances, meaning the location of the wind turbine was determined based on its application. Since then, the trend in wind energy has gone in a different direction towards larger and higher power turbines (Molina and Enrique Mercado, 2011), typically installed far away from where the energy is consumed. However, recently, the idea of local energy generation from small wind turbines has received increasing attention again (Toja-Silva et al., 2013; Stathopoulos et al., 2018; KC et al., 2019). This way, transmission infrastructure and costs can be reduced. Urban wind energy can be integrated into the power grid but also function independently, for example, in remote areas (Toja-Silva et al., 2013).

Constraints

There are still certain issues impeding a widespread deployment of urban wind energy. These include questions of efficiency, safety, structural integrity, noise, visual impact, environmental impact and connected to all of that, social acceptance (Oppenheim et al., 2004). Wind turbines are generally safe machines held to a high safety standard (IEC, 2013). However, on sites close to people, it becomes even more crucial to avoid failures (Beller, 2011). Often, the issue is not in actual, but rather in perceived safety (Oppenheim et al., 2004). New technologies or technologies in new environments raise concerns that can result in factual cost increases due to increased in-

insurance or permitting costs (Oppenheim et al., 2004). Regarding noise, there are two main sources, mechanical and aerodynamic (Manwell et al., 2010). Mechanical noise is related to the gearbox, generator and potential yaw drives (Wagner et al., 1996). Aerodynamic noise originates from the interaction of the blades with the flow and can reach noise levels comparable to city traffic for small wind turbines (Oppenheim et al., 2004). The aerodynamic noise is strongly dependent on the tip speed ratio (equation 1.4) of the blades (Wagner et al., 1996). The visual impact of a wind turbine is a largely subjective matter, but there are certain parameters to consider, such as alteration, consistency and degradation of the viewshed, as well as conflict with public reference and guideline compatibility (Manwell et al., 2010). In an urban environment, where man-made objects such as buildings dominate the environment already, it can be argued that the alteration and degradation of the viewshed are lower, while the consistency is higher. Public preference and guideline compatibility are more complicated parameters to satisfy in an urban environment. The environmental impact of wind turbines, particularly on wildlife, is an important factor to consider before any wind turbine installation (Saidur et al., 2011). The relative impact is smaller for installations in urban regions, where the environment is already substantially impacted by human life and the wind turbine size is usually small compared to the buildings (Toja-Silva et al., 2013). A more detailed overview of political, economic, social and environmental issues to consider regarding urban wind energy is provided in Stankovic et al. (2009).

Urban wind resources

Widely regarded as the key issue of urban wind energy today is an insufficient understanding of urban wind resources (Toja-Silva et al., 2015; Stathopoulos et al., 2018; KC et al., 2019; Rezaeiha et al., 2020). The available power in the wind scales with the velocity cubed (see equation 1.1). Thus, it is important to understand the local variations of wind velocity in an urban environment (Beller, 2011; Ishugah et al., 2014). The atmospheric boundary layer is altered by the geographical topology as well as roughness elements, such as plant canopies, buildings and wind turbines (Porté-Agel et al., 2020). An urban environment presents a high level of complexity, with obstacles, such as buildings, of various sizes influencing the flow. Above an urban environment a so-called urban boundary layer evolves (Oke, 1976, 1988; Wang et al., 2014), illustrated in figure 1.4. The urban canopy layer reaches from the ground to approximately building height (Oke, 1976). Here, the flow is strongly dependent on the local topology, resulting in large variations in the flow and overall low mean wind velocities (Kooiman and Tullis, 2010; KC

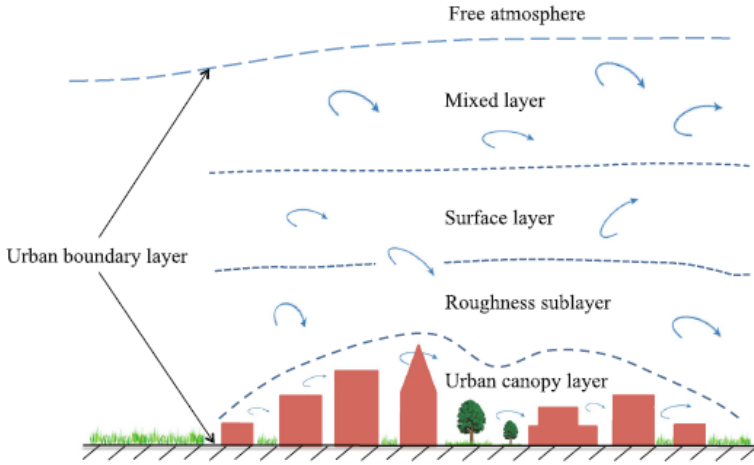


Figure 1.4: The urban boundary layer from Wang et al. (2014), based on the definition by Oke (1976) and Oke (1988).

et al., 2019). Above the urban canopy layer, the roughness sublayer is situated, extending from roof height to approximately 2 to 5 building heights (Raupach et al., 1991; Roth, 2000). Some homogenization of the flow occurs in the roughness sublayer, but the flow remains affected by individual roughness elements such as buildings (Wang et al., 2014). Farther up in the surface layer, the impact of individual roughness elements becomes insignificant, and the flow becomes homogeneous horizontally, and above that in the mixed layer, also approximately homogeneous vertically (Wang et al., 2014). Purely from the perspective of available wind power and consistency of the wind resources, it would be desirable to place the wind turbine high up in the mixed layer or at least the surface layer. However, large installations in the urban environment are not realistic due to the above-listed design constraints, especially visual impact, public acceptance and often limited availability of space. Even placing large-scale wind turbines in proximity to inhabited areas has proven to be difficult (Cohen et al., 2014). Thus, wind turbines in the urban environment are, on average, relatively small, i.e. small rotor swept area A , thus making high wind velocities even more important. To ensure high enough velocities, the urban canopy layer is mostly avoided, resulting in urban wind turbines largely placed in the roughness sublayer (Millward-Hopkins et al., 2012).

The roughness sublayer is characterized by high velocity fluctuations

$$u' = u - U, \quad (1.5)$$

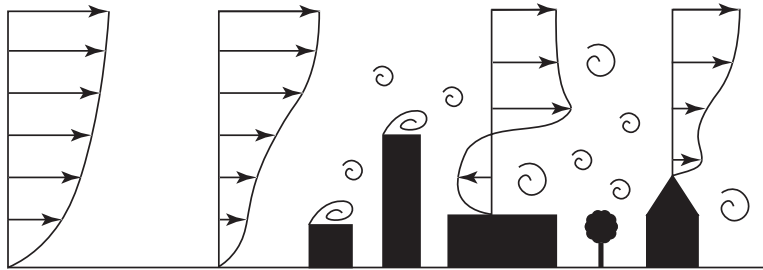


Figure 1.5: Schematic display of the complexity that makes up the urban wind field.

i.e., the difference between the instantaneous velocity u (m/s) and the mean (time-averaged) velocity U (m/s). Typically the level of the fluctuations is expressed relative to the mean velocity, u'/U , referred to as the turbulence intensity. While, in the atmospheric boundary layer u'/U is typically around 5% to 15% (Mücke et al., 2011), these values increase in the roughness sublayer up to 20% to 40% (Roth, 2000). In addition, the flow in the roughness sublayer is sheared vertically. Wagner et al. (2009) showed in their 2340 independent field measurements that, unlike typically assumed, the atmospheric boundary layer does not generally follow a power law or a logarithmic profile. They classified their measurements from 40 m to 160 m above the ground into 173 different wind profiles and found a wide range of vertical shear between approximately $\Delta U(z)/U_{\text{ref}} = 6\%$ and 63% from bottom to top, with a reference velocity U_{ref} taken at 80 m. Similar vertical gradients were observed in an urban environment by Li et al. (2010) with measurements extending from the urban canopy layer into the roughness sublayer.

The flow in the roughness sublayer is not as chaotic and inhomogeneous as in the urban canopy layer, but it is still governed by local obstructions, such as buildings. Most building geometries feature sharp edges. At these sharp edges, the flow is prone to separate, resulting in regions of low velocity and highly turbulent flow close to the building (Mertens, 2006). The flow is deflected around these regions, leading to strongly skewed flow. Large wake regions with reduced and highly fluctuating flow velocities form downstream of buildings. Considering that an urban environment typically features buildings of various shapes and sizes in a non-uniform arrangement, it is apparent that the urban wind resources feature a high level of complexity (illustrated in figure 1.5). Evaluating the urban wind resources appropriately thus presents a major challenge.



Figure 1.6: From left to right: Bahrain World Trade Center with building integrated wind turbines ([Atkins, 2008](#)), Roof-mounted wind turbines on the Greenpeace headquarters in Hamburg ([Neuhauser, 2016](#)), stand-alone turbines besides houses in residential area in Illinois ([EcoPlanetEnergy, 2011](#)).

Urban wind turbines

To harvest the urban wind resources various types of wind turbines are utilised. Three general categories of urban wind turbines are distinguished ([Campbell et al., 2001](#); [Stankovic et al., 2009](#); [Beller, 2011](#); [Ishugah et al., 2014](#)), illustrated in figure 1.6:

- Full building integration → The building is designed to integrate the wind turbine, most famously in the Bahrain World Trade Center (left in figure 1.6).
- Building-mounted → The turbine is retrofitted to existing buildings, typically roof-mounted (middle in figure 1.6).
- Stand-alone → Wind turbines in the urban environment, independent of building structures (right in figure 1.6).

The focus in this study is primarily on roof-mounted wind turbines. Their main advantage, compared to stand-alone turbines, is the employment of the building as a means of elevating the turbine. Full building integration is a promising concept; however, it is primarily an option for new building projects. See, e.g. [Ge et al. \(2021\)](#) for an examination of stand-alone turbines in the proximity of a building and [Mertens \(2006\)](#) and [Haase and Löffström \(2015\)](#) for more details on building integrated wind turbines.

Another area of interest has been finding a suitable wind turbine design for urban environments, considering the unique urban wind resources ([Mertens, 2003](#); [Oppenheim et al., 2004](#); [Dayan, 2006](#); [Beller, 2011](#); [Bertényi et al., 2012](#); [Toja-Silva et al., 2013](#); [Pagnini et al., 2015](#); [Acarer et al., 2020](#)). The

preferred axis of rotation has been discussed extensively. Riegler (2003), Mertens (2003), Kooiman and Tullis (2010), Toja-Silva et al. (2013) and Kumar et al. (2018) suggest that VAWTs are better suited for the urban environment compared to HAWTs. Kooiman and Tullis (2010) and Toja-Silva et al. (2013) point to the omnidirectionality of VAWTs as a significant advantage due to the fast-changing wind conditions in urban areas. Mertens (2003) note that lift-driven VAWTs are superior in skewed flow, typically observed above buildings. Pagnini et al. (2015) compared the performance of a HAWT and VAWT in a full-scale urban environment. While the HAWT yielded a higher power output, it was also more susceptible to gusts and changes in wind direction, leading to significantly increased maintenance for the HAWT.

Roof-mounted wind turbines

Studies on roof-mounted wind turbines have been primarily conducted as investigations of different roof and building shapes (Ledo et al., 2011; Abohela et al., 2013; Toja-Silva et al., 2015, 2016; Shahizare et al., 2016; Zhou et al., 2017; Dar et al., 2022) and the ideal position of a wind turbine on a roof (Mertens, 2003, 2006; Ledo et al., 2011; Abohela et al., 2013; Vita et al., 2020; Dar et al., 2022). To examine the ideal building shape and turbine position, typically, studies rely on flow measurements or simulations. Equation 1.1 is utilised to estimate P_a based on local wind velocities. This is a simple approach that gives general insight, independent of the turbine type. However, the interaction of the wind turbine with the flow is neglected in this type of analysis.

Many different roof and building shapes exist in urban environments (see figure 1.5). Abohela et al. (2013) examined the suitability of six different roof shapes, namely, flat, spherical, gabled, pyramidal, vaulted and pitched, for five wind directions. Flow acceleration was detected for every roof shape, most significant for a vaulted roof and lowest for a pyramidal roof. Round roof shapes were found to be most beneficial for potential power extraction, followed by a simple flat roof. Similar conclusions on the ideal roof shape were drawn by Toja-Silva et al. (2015). In addition, the influence of the roof edge geometry was investigated. Again round shapes were found to be beneficial for the wind velocities above the roof, whereas a railing had a negative impact. Dar et al. (2022) examined the influence of the roof shape on the performance of a roof-mounted HAWT. The ratio between turbine and building size d_T/h was 0.26, with a hub height $0.22h$ above the building. The worst performance was recorded for a fenced roof edge, which also showed the greatest variability dependent on the streamwise

turbine position. A regular sharp roof edge yielded higher power output for all streamwise positions. Rounding off the roof edge reduced the variability significantly, resulting in increased power output on the downstream half of the building compared to the sharp-edged roof. [Ledo et al. \(2011\)](#) applied the question of ideal roof shape to an array of buildings with flat, gabled and pyramidal roofs. They found the highest velocities and lowest turbulence intensities above flat roofs and, thus, recommended flat roof buildings for the installation of roof-mounted wind turbines.

Possibly the most important and certainly the most practical question is where to place a wind turbine on a building. Unfavourable placement of wind turbines has led to many installations performing poorly or even experiencing reduced durability ([Smith et al., 2012](#)). [Mertens \(2003\)](#) determined a central turbine position on a flat roof building preferable compared to a position at the edge or in the corner. [Abohela et al. \(2013\)](#) found that for flat, spherical and vaulted roof shapes, a relatively central position is ideal, whereas for gabled and pitched roofs, a corner position, and for pyramidal roofs, an edge position yielded the highest wind velocities. Turbine positions below 0.3 building heights h above the roof were not considered due to high u'/U here. For most examined roof shapes and wind directions, the ideal height was found at that lower limit of $1.3h$ above the ground, with few exceptions reaching up to $1.6h$. Similarly, [Vita et al. \(2020\)](#) concluded from their flow analysis above a high-rise building that locations close to the roof (<0.3 building widths) are possibly problematic due to low velocities and high u'/U . However, they rightfully point out that elevating the wind turbine further than that can cause significant complications, potentially leading to structural issues. Thus, a careful consideration of all potential turbine heights, including regions close to the roof, is important.

[Dar et al. \(2022\)](#) examined hub heights of $0.22h$ (i.e. the rotor swept area extends down to $0.09h$ above the roof) for a HAWT and found a position close to the upstream edge ($\approx 0.13h$ to $0.27h$ downstream) to be ideal. [Zhang et al. \(2022\)](#) used actuator disk models on a building array with a turbine size of $d_T/h = 0.25$ at three different hub heights between $0.375h$ and $0.875h$ above the roof. Independent of height, turbines on the first building row yielded the highest estimated power output, whereas on the second building row, the turbines performed worst. Downstream of that, the power output became approximately constant. The question of ideal turbine position is multifaceted. Depending on the model building(s) and turbine representation, or lack thereof, the conclusions vary.

Modeling of urban environments

To study urban flows experimentally or numerically, some representation of the urban environment is required. There are different approaches to modelling an urban environment, varying in level of complexity. This can range from case studies, reproducing a close approximation of reality (Yang et al., 2016; Al-Quraan et al., 2016; Hertwig et al., 2021) to simplified geometries arranged in arrays (Ledo et al., 2011; Millward-Hopkins et al., 2012; Vita et al., 2020; Ferreira and Ganapathisubramani, 2021; Zhang et al., 2022) or examined individually (Abohela et al., 2013; Toja-Silva et al., 2015; Ge et al., 2021; Dar et al., 2022). The simplest building geometry is a cube. Thus, cubes have been utilised heavily in this context, e.g. by Ge et al. (2021), Ferreira and Ganapathisubramani (2021), and Zhang et al. (2022), as well as as a base geometry for Abohela et al. (2013), Toja-Silva et al. (2015) and Dar et al. (2022). Besides their simplicity, cubes have the advantage of being an extensively studied flow problem. The flow around a single surface-mounted cube in two different orientations for uniform inflow and submerged in a boundary layer was studied by Castro and Robins (1977). Oriented parallel with the main flow direction, the flow was shown to separate at the windward top edge of the cube, resulting in very low momentum, partly recirculating, flow close to the roof, followed by a strong shear layer above. Rotating the cube by 45° shrank this low velocity region along the centre line of the cube significantly. The influence of freestream turbulence intensity u'_∞/U_∞ on the flow around a surface-mounted cube has been investigated by Yakhot et al. (2006) and Hearst et al. (2016). Increasing u'_∞/U_∞ was found to decrease the size of the recirculation region forming on top of the cube.

1.2.3 Turbulence and shear

As described above, the urban wind resources are characterized by high levels of turbulence intensity, interacting with a naturally sheared urban boundary layer flow. These interactions are complex; thus, the focus here will be a simplified look at the effect of freestream turbulence (FST) on a turbulent boundary layer (TBL). In addition, the generation of FST and sheared flows and their general impact will be discussed.

Turbulence

The study of turbulence dates back more than a century (Reynolds, 1883; Prandtl, 1904); nevertheless, it is still a large ongoing research field today (Smits and Marusic, 2013; Duraisamy et al., 2019) and remains relevant for

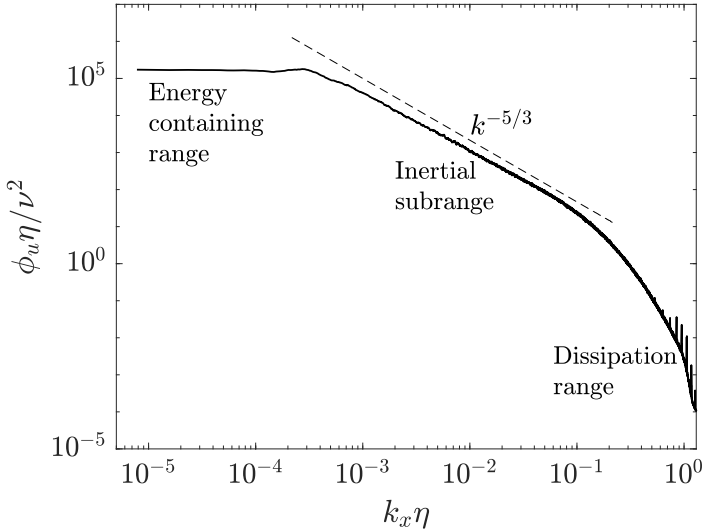


Figure 1.7: Example spectral distribution of energy of the streamwise velocity fluctuations of data from original Constant Temperature Anemometry measurements.

many modern-day problems (Davidson, 2015), such as atmospheric flows, the flow around aeroplanes, ships, vehicles, wind turbines and many more. The most fundamental form of turbulence is homogeneous isotropic turbulence (HIT), with turbulent statistics that are invariant under translations, rotations, and reflections of the coordinate axis (Pope, 2000). A range of scales exists in HIT ranging from the largest scales in the energy containing range to the smallest scales, where energy is dissipated. This concept is visualized by the spectral distribution of energy, ϕ_u , for the streamwise velocity fluctuations in figure 1.7. It is normalized by the Kolmogorov length scale η , representative of the smallest scales and the kinematic viscosity ν , and plotted against the wave number k_x normalized by η . The wave number is inversely proportional to the length scales in the flow. If the separation between the largest and smallest scales is large enough, an intermediate region arises, the inertial sub-range, where energy is transported from larger scales to smaller scales. The inertial sub-range is characterized by an intermediate length scale, the Taylor microscale λ_∞ . The associated Reynolds number is $Re_\lambda = \frac{u'_\infty \lambda_\infty}{\nu}$. A greater Re_λ indicates a larger separation of scales.

To study HIT, it is often either simulated, e.g. as box turbulence, or generated experimentally on a lab-scale. There exist various methods to approximate HIT experimentally, the most prominent being grid turbulence. The grids typically consist of crossing bars spaced apart by a constant mesh length M . The bars block the flow and generate wakes, whereas, through the openings, the flow accelerates. These high and low velocity regions mix downstream of the grid and generate turbulence. Close to the grid, the flow is inhomogeneous, and anisotropic (Ertuğ et al., 2010), i.e., the relative position to the grid bars determines the turbulent statistics. However, going far enough downstream of the grid, $x/M \gtrsim 30$, the turbulence statistics become approximately homogeneous and isotropic (Comte-Bellot and Corrsin, 1966). To generate a larger separation of scales and, thus, higher Re_λ and u'_∞/U_∞ , Makita (1991) came up with a so-called active grid. That is, rotating rods equipped with a series of wings, controlled individually by electrical motors (see example figure 1.8). The wings are typically oscillated at an assigned amplitude or rotated within a set range of random frequencies. Larssen and Devenport (2011) and Hearst and Lavoie (2015) showed that the mean rotational velocity of the grid Ω_G has a dominant influence on the turbulence statistics. A lower Ω_G yields higher Re_λ and u'_∞/U_∞ . The same can be achieved by an increase of U_∞ , indicating that Ω_G relative to U_∞ is what governs the turbulence generation. While being susceptible to slight anisotropy (Mydlarski and Warhaft, 1996; Sharp et al., 2009; Hearst and Lavoie, 2015), active grids have proven to generate significantly higher Re_λ and u'_∞/U_∞ than passive grids (Mydlarski and Warhaft, 1996; Larssen and Devenport, 2011) and enable a decoupling of u'_∞/U_∞ and $L_{u,\infty}$ (Hearst and Lavoie, 2015). Active grids have been successful in expanding the parameter space of lab-scale turbulence (Mydlarski and Warhaft, 1996; Larssen and Devenport, 2011) and in tailoring the velocity profile and turbulence statistics e.g. for atmospheric flows (Knebel et al., 2011) and wind turbines (Hearst and Ganapathisubramani, 2017).

Wall-bounded shear flow

Shear flows frequently occur in nature, e.g., in the atmospheric boundary layer, in ocean currents and in pipe or channel flow. A prominent type of shear flow is wall-bounded flow, which occurs whenever the flow is confined by at least one solid boundary (Smits and Marusic, 2013). A boundary layer evolves, where the velocity changes from zero at the wall to the freestream velocity. An example of this is the atmospheric boundary layer, where the flow is confined by the ground at the bottom while flowing freely at the top. A boundary layer can be laminar or turbulent, depending on the ratio

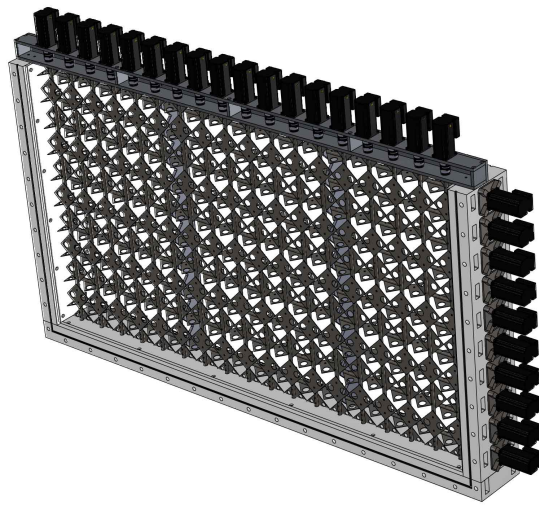


Figure 1.8: 3D model of the active grid in the water channel facility in the Fluid Mechanics Laboratory at the Norwegian University of Science and Technology.

between inertial and viscous forces, described by the Reynolds number,

$$Re = \frac{\mathcal{U}\mathcal{L}}{\nu}, \quad (1.6)$$

where \mathcal{U} (m/s) is the characteristic velocity scale, \mathcal{L} (m) is the characteristic length scale. Most real-world flows have a turbulent boundary layer, making it a much studied problem (Clauser, 1956; Coles, 1956; Robinson, 1991; Hutchins and Marusic, 2007; Schlatter and Örlü, 2010). TBL velocity profiles are typically expressed in so-called wall coordinates, $y^+ = \frac{yU_\tau}{\nu}$ and $U^+ = \frac{U}{U_\tau}$, where $U_\tau = \sqrt{\frac{\tau_w}{\rho}}$ is the friction velocity with the wall shear stress τ_w . An illustrative velocity profile of a canonical TBL is depicted in figure 1.9. The boundary layer thickness δ is typically determined as the point where the mean streamwise velocity reaches 99% of the freestream velocity. To characterize a TBL, the friction Reynolds number $Re_\tau = \frac{U_\tau\delta}{\nu}$ is used. Velocity profiles in a TBL are self-similar near the wall in the viscous sublayer $y^+ \lesssim 5$, the logarithmic region and the buffer layer in between them. In the viscous sublayer, the velocity profile follows $U^+ = y^+$, while in the logarithmic region, it is described by $U^+ = \frac{1}{\kappa}\ln(y^+) + C^+$, with the von Kármán constant κ and the additive constant C^+ . In between the logarithmic layer and the freestream, large-scale mixing leads to a velocity deficit, the so-called wake region (Coles, 1956). Everything outside the viscous sublayer and the buffer layer can be described by the composite profile by Coles (1956), with the wake function \mathcal{W} described by Chauhan et al. (2009):

$$U^+ = \frac{1}{\kappa}\ln(y^+) + C^+ + \frac{2\Pi}{\kappa}\mathcal{W}\left(\frac{y^+}{Re_\tau}\right), \quad (1.7)$$

where Π is Coles' wake parameter, indicating the strength of the wake region. Coles (1956) and Marusic et al. (2010) suggest that Π is around 0.55 for high Reynolds numbers. The variance profile in a TBL, u'^2/U_τ^2 (figure 1.9) exhibits a peak close to the wall at $y^+ \approx 15$, that increases in magnitude with increasing Re_τ (Marusic et al., 2010). Also, the outer region in the variance profile, by some considered an outer peak, grows with Re_τ , whereas the viscous sublayer is unaffected. Hutchins and Marusic (2007) introduced spectrograms to gain insight into the energy distribution in a TBL. Spectrograms are contourmaps showing the energy content across different scales, along a geometrical space. In the context of boundary layers, that is pre-multiplied energy spectra in wall coordinates $\phi^+ = \phi_u k_x / U_\tau^2$, for wave lengths $\zeta^+ = 2\pi U_\tau / k_x \nu$, at different wall-normal positions y^+ across the boundary layer. Hutchins and Marusic (2007) observed, that for sufficiently

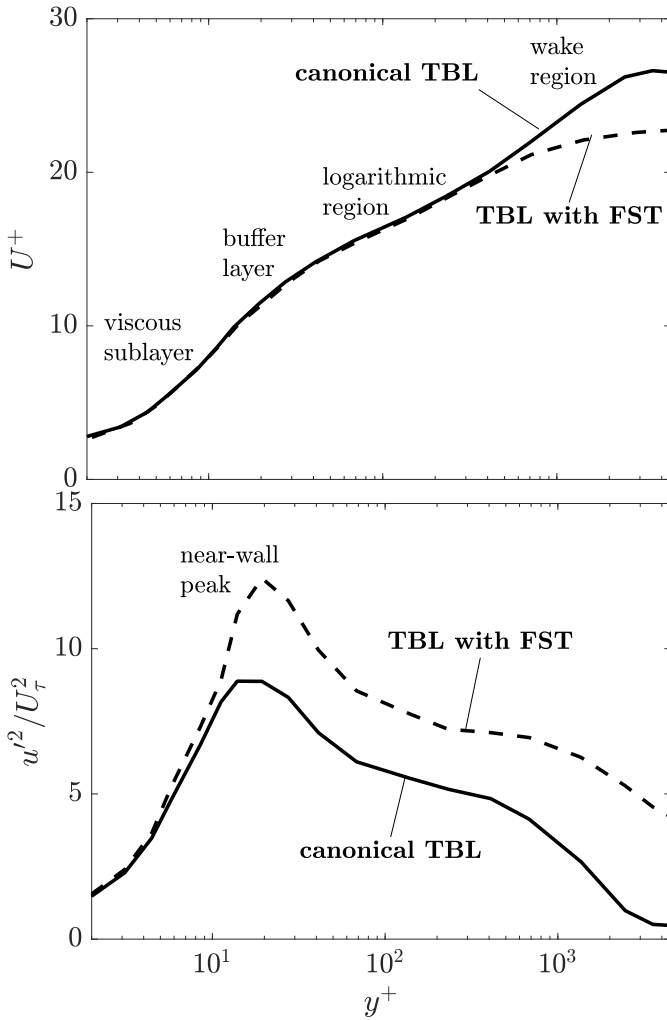


Figure 1.9: Example turbulent boundary layer velocity and variance profiles, with and without freestream turbulence of data from original Laser Doppler Velocimetry measurements.

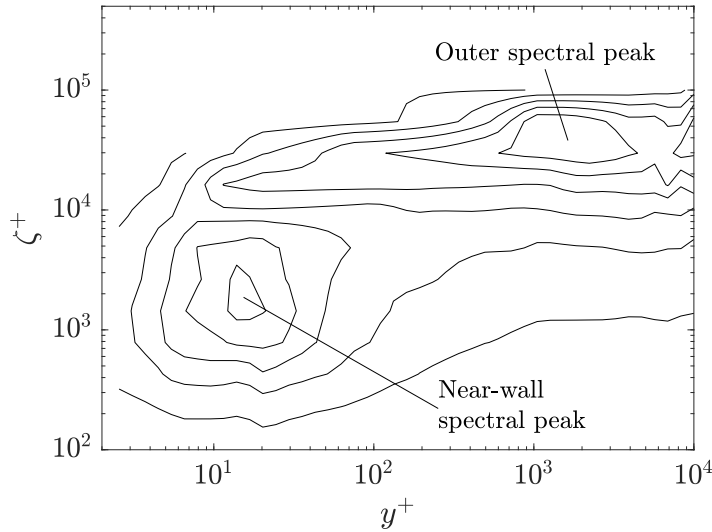


Figure 1.10: Example of a TBL spectrogram showing an outer spectral peak of data from original Laser Doppler Velocimetry measurements. The contour lines represent constant levels of ϕ^+ with maxima at the marked peaks, decreasing outwards from there.

high Re_τ ($=7300$ in their study), an outer spectral peak emerges in addition to the near-wall spectral peak. This is illustrated in figure 1.10. As a TBL evolves spatially, Re_τ grows and features, such as a growing near-wall variance peak and the emergence of an outer spectral peak, can be observed (Vincenti et al., 2013; Marusic et al., 2015).

Turbulent boundary layers subjected to freestream turbulence

Often, the flow outside of the TBL is also turbulent which adds complexity to the problem, with two interacting flows. This has been studied, dating back to the seminal works by Hancock and Bradshaw (1983, 1989). The FST was generated with a passive grid in a wind tunnel, and it was shown that FST increases the size of the TBL and the irregularity of its interface, as illustrated in figure 1.11. It was concluded that the TBL is influenced by the freestream turbulence intensity u'_∞/U_∞ , as well as the integral length scale $L_{u,\infty}$, which they summarized in the empirical parameter $\beta = \frac{u'_\infty/U_\infty}{L_{u,\infty}/\delta+2}$. Blair (1983a,b) and Castro (1984) found in similar studies that increasing levels of FST lead to an increase of skin friction. Blair (1983b) also reported a suppression of the wake region for turbulence

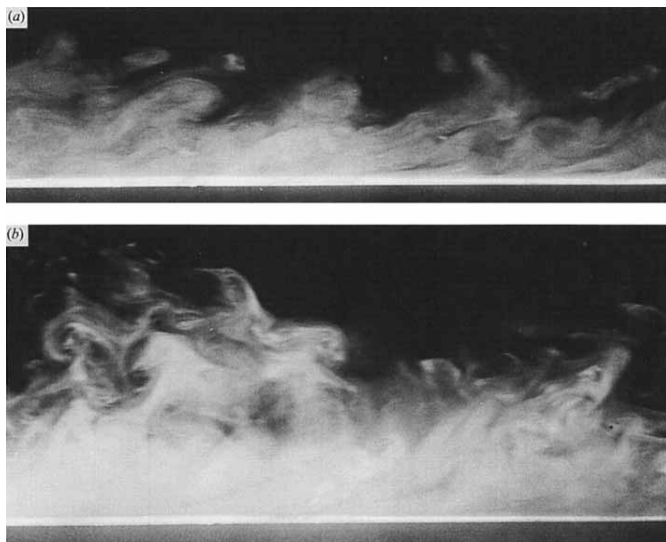


Figure 1.11: Smoke visualizations of a turbulent boundary layer (a) without freestream turbulence and (b) subjected to freestream turbulence (Hancock and Bradshaw, 1989).

intensities greater than approximately 5%. This is illustrated in figure 1.9 in comparison to a canonical TBL. At the same time, the viscous sublayer and the logarithmic layer remain unaffected. A limitation of some of these early studies was the level of u'_{∞}/U_{∞} that was achievable with passive grids. Maximum values of around 7% were recorded and in order to reach that, it was partly necessary to measure close to the grid (Hancock and Bradshaw, 1983, 1989; Castro, 1984), i.e., significantly upstream of $x/M = 30$, where the flow typically still is inhomogeneous (Comte-Bellot and Corrsin, 1966; Ertunç et al., 2010). To overcome some of these limitations, various approaches were employed to study this problem, such as other turbulence generating devices, e.g., crossflow jets (Thole and Bogard, 1996) and active grids (Sharp et al., 2009; Dogan et al., 2016, 2017, 2019; Esteban et al., 2017; Hearst et al., 2018), as well as direct numerical simulation (DNS) (Wu et al., 2019; You and Zaki, 2019; Kozul et al., 2020). These confirmed the increased boundary layer thickness, the suppression of the wake region and the increase of skin friction with increasing u'_{∞}/U_{∞} . Esteban et al. (2017) specifically reaffirmed the increase of U_{τ} with oil film interferometry measurements. Dogan et al. (2016) showed that in the presence of FST, Π is reduced well below the value of a canonical TBL, down to $\Pi = -0.52$. In addition, they found that the near-wall peak in the variance profile scales

with u'_∞/U_∞ (see figure 1.9). Sharp et al. (2009) first observed the emergence of an outer spectral peak in the pre-multiplied energy spectrograms (see figure 1.10) forced by the FST at significantly lower Re_τ than for a canonical TBL. The near-wall spectral peak remained unaffected. Dogan et al. (2016), Hearst et al. (2018) and You and Zaki (2019) confirmed this finding. Dogan et al. (2016) showed that the magnitude of the outer spectral peak scales with u'_∞/U_∞ . Hearst et al. (2018) found that the outer spectral peak results from the large scales penetrating the TBL. In addition, Hearst et al. (2018) decoupled u'_∞/U_∞ and $L_{u,\infty}$ and found that for changes up to 65% of $L_{u,\infty}$, there was no influence of $L_{u,\infty}$ on the features of the TBL at fixed u'_∞/U_∞ . Wu et al. (2019) took a closer look at the interface between FST and a TBL and found that it is largely governed by the large-scale motions of the TBL. Kozul et al. (2020) studied the temporal response of a TBL to FST and characterized the problem based on the relative large-eddy turnover time e , which is a measure of the relative fluctuating strain rate between TBL and FST (Hancock and Bradshaw, 1989). They found that the impact of the FST on the TBL depends on the magnitude of e . Overall, it can be stated that the TBL is, at least momentarily, matured ahead of its natural evolution by the presence of the FST. Largely unexplored is the spatial evolution of a TBL subjected to FST. All experimental studies on the matter were single position measurements, i.e. the TBL was examined at one streamwise position.

Influence of turbulence and shear on wind turbines

Being placed in the atmospheric boundary layer, wind turbines are naturally subjected to FST and sheared flow. This has been studied, e.g., by Elliott and Cadogan (1990), Medici and Alfredsson (2006), Wagner et al. (2009), Choukulkar et al. (2016), Bartl et al. (2018), Kavari et al. (2019), Li et al. (2020) and Gambuzza and Ganapathisubramani (2021). Generally, a faster recovery of the wake deficit was found for increased FST (Medici and Alfredsson, 2006; Bartl et al., 2018; Li et al., 2020), while sheared inflow had only limited influence on the wake characteristics (Bartl et al., 2018; Li et al., 2020). Freestream turbulence intensities are further amplified in an urban environment by the presence of buildings and other obstructions to the flow (Roth, 2000). Thus, the impact of FST has been of particular interest for VAWTs, often employed in urban environments (Kooiman and Tullis, 2010; Danao et al., 2013; Scheurich and Brown, 2013; Wekesa et al., 2016; Loganathan et al., 2017; Aliferis et al., 2019). Reduced power coefficients for increased FST were found by Danao et al. (2013), Scheurich and Brown (2013), Loganathan et al. (2017) and Aliferis et al. (2019), whereas

Wekesa et al. (2016) found an increase in C_P for low wind velocities and a decrease for high velocities. Kooiman and Tullis (2010) found that the turbine performance is relatively unaffected up to $u'_\infty/U_\infty = 15\%$. For higher FST levels, the performance was found to decrease linearly with increasing u'_∞/U_∞ . In addition, the flow in an urban environment is regularly deflected by obstructions, such as buildings, resulting in skewed flow (Mertens, 2006). Simão Ferreira et al. (2006) observed a performance increase of a VAWT for skew angles up to 30° to 40° , with decreasing performance for higher angles. Largely unexplored is the combined influence of FST and shear on the wind resources above a building.

1.3 Objectives

Urban wind energy is a promising concept with the potential to contribute to decentralized green energy generation. However, one of the major factors hindering its widespread employment is a limited understanding of the urban wind resources (Stathopoulos et al., 2018; KC et al., 2019). This study aims to address this, specifically by examining the siting of roof-mounted wind turbines in various flow conditions. The research can be divided into four guiding questions, addressed in articles I, II, III, IV:

I *How does a turbulent boundary layer subjected to freestream turbulence evolve spatially?*

Wind turbines are generally placed in the atmospheric boundary layer. In urban environments, this is complemented by high levels of turbulence intensity (KC et al., 2019). Article I investigates a simplified version of this background flow. TBLs have been studied extensively on a fundamental level (see Smits et al. (2011) for a summary) and also the influence of FST on them has been documented (e.g., Hancock and Bradshaw (1989); Dogan et al. (2016)). It was shown that the FST matures the TBL ahead of its natural evolution (Dogan et al., 2016; Hearst et al., 2018). The question remains if this enhanced evolution was permanent. Article I examines the spatial development of a TBL subjected to FST and, thus, addresses this question.

II *What is the flow field around a roof-mounted vertical axis wind turbine, and how does that affect its performance?*

To evaluate the potential power output of a roof-mounted wind turbine, it is common practice to estimate the available power P_a based on the local wind velocity (see equation 1.1), obtained, e.g., from

wind tunnel measurements (Al-Quraan et al., 2016; Vita et al., 2020) or simulations (Abohela et al., 2013; Toja-Silva et al., 2015). [Article II](#) investigates the flow field around a roof-mounted VAWT on two model buildings and shows how the turbine interacts with the flow at various positions on the roof. The variety of flow conditions a roof-mounted wind turbine experiences is illustrated. Simultaneously, the power output of the turbine is measured, and thus, the impact of the turbine position and the corresponding flow conditions on the turbine performance are evaluated.

III *What is the impact of wind direction and turbine position on the performance of a roof-mounted vertical axis wind turbine?*

Expanding on [Article II](#), [Article III](#) investigates the performance of a roof-mounted VAWT at various positions for different wind directions through direct measurements of the power output. This is an attempt to answer the ever-present question of the ideal position of a roof-mounted wind turbine. With six turbine positions, including two different heights, subjected to five different wind directions, [Article III](#) explores a large parameter space for this research question. Recommendations on the ideal position are deduced for individual wind directions and turbine heights as well as holistically, independent of wind direction and/or turbine height.

IV *What is the influence of freestream turbulence and shear on the flow around a roof-mounted vertical axis wind turbine, and how is its performance affected by them?*

Urban flows are characterized by high levels of FST and shear. Combining [Article I](#) and [Article II](#), [Article IV](#) investigates how the flow field around two model buildings is affected by incoming turbulence and shear. This enables a controlled analysis of the flow around individual buildings in realistic urban flow conditions, essentially decoupling individual buildings from their surroundings. Again, the power output of a roof-mounted VAWT at various positions on the buildings is measured, examining how it is affected by the different inflow conditions.

Chapter 2

Experimental Methods

This chapter describes the methodology used in this study. The facilities, experimental set-ups and measurement techniques are documented.

2.1 Facilities

Two facilities have been used in this study. The experiments for [Article I](#) were conducted in the water channel, while the experiments for articles [II](#), [III](#) and [IV](#) all took place in the large-scale wind tunnel. Both facilities are part of the Fluid Mechanics Laboratory at the Norwegian University of Science and Technology.

Water channel

The water channel facility is a relatively new facility, operational since 2019. A schematic of the facility is presented in figure [2.1](#). The test section spans $11\text{ m} \times 1.8\text{ m} \times 1\text{ m}$ (length \times width \times height) with a maximum fillable water height of 0.8 m. Including the settling chamber and end tank, the water channel has a maximum capacity of 65 tons of water. The flow is driven by two Siemens 1AV2186B 3-phase squirrel-cage thrusters connected to a composite 4-bladed counter-rotating Kaplan propeller set with a total power of 56 kW and controlled by two variable frequency drives. The propellers are placed in the two return pipes that feed the water to the settling chamber through two 90° elbows. Here the flow streams through a porous outlet diffuser into the settling chamber, breaking the momentum of the flow with an adjustable surface plate. This is followed by multiple screens, a honeycomb, and a 4:1 contraction to condition the flow, i.e., make it homogeneous, approximately isotropic and reduce the velocity fluctuations.

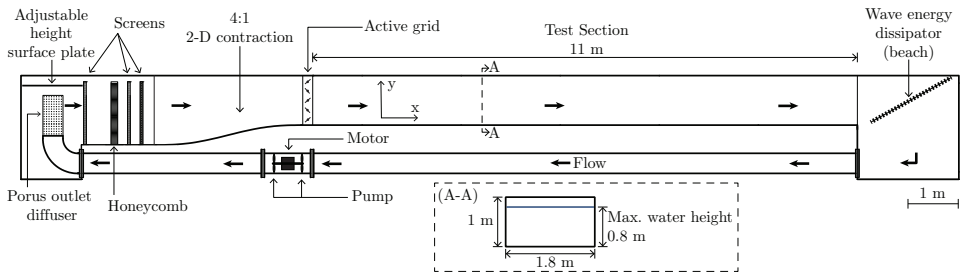


Figure 2.1: Water channel facility in the Fluid Mechanics Laboratory at the Norwegian University of Science and Technology.

Immediately upstream of the test section, the water channel is equipped with a built-in active grid, which can be used to tailor the incoming flow. More details on the active grid and its actuation are provided in section 2.2. Downstream of the test section, a beach is installed to dissipate excess wave energy. From the end tank, the water is sucked back into the return pipes. To measure the freestream velocity in the water channel, a Höntzsch ZS25 vane wheel flow meter is used. Temperature changes in the water are tracked with a T-type thermocouple.

Wind tunnel

The large-scale wind tunnel at the Norwegian University of Science and Technology has existed for decades and over the years has yielded both high quality fundamental fluid mechanic research (e.g. Pearson et al. (2002); Krogstad and Davidson (2010, 2011)), as well as cutting edge research in the field of wind energy (e.g. Adaramola and Krogstad (2011); Krogstad and Eriksen (2013); Bartl et al. (2018)). It is a closed loop recirculating wind tunnel with a 11.15 m \times 2.71 m \times 1.80 m (length \times width \times height) test section. A schematic of the wind tunnel is displayed in figure 2.2. It is powered by a 220 kW radial fan downstream of the test section. The rotational velocity of the fan, and thus the flow velocity in the test section, can be controlled with a variable frequency drive. The maximum velocity in the test section is approximately 23 m/s. The flow is directed with guiding vanes and passes through multiple screens and a honeycomb to ensure good flow quality, i.e., homogeneous, isotropic and low turbulence inflow. This is further facilitated by a 4.2:1 contraction immediately upstream of the test section. Since 2021 the wind tunnel features an active grid that can be inserted downstream of the contraction. This was utilised in Article IV to generate varying levels of turbulence intensity and shear. The active

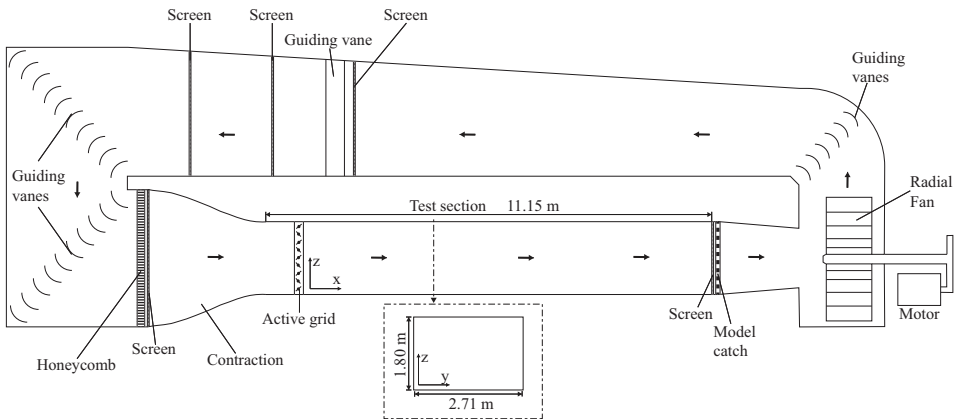


Figure 2.2: Large-scale wind tunnel facility in the Fluid Mechanics Laboratory at the Norwegian University of Science and Technology.

grid and its actuation parameters will be discussed in more detail in section 2.2. For articles II and III a clean inflow configuration was used. The wind tunnel is equipped with a pitot-static tube to measure the freestream velocity and a K-type thermocouple to measure the temperature in the tunnel. In addition, the atmospheric pressure is tracked throughout all experiments with a mercury barometer.

2.2 Active grids

Two active grids have been utilised in the course of this study, the water channel active grid to generate the different levels of freestream turbulence for Article I, and the wind tunnel active grid to generate the different levels of freestream turbulence and vertical shear used in Article IV. Both active grids are modeled after the design of Makita (1991), taking into account experience from previous active grid studies, such as Mydlarski and Warhaft (1996) and Hearst and Lavoie (2015). They are both biplanar grids; that is, the crossing grid bars are slightly offset in the streamwise direction to enable free rotation.

Water channel active grid

The water channel active grid is shown in figure 2.4. It spans the entire test section - 1.8 m \times 1.0 m (width \times height). The grid contains 10 horizontal and 18 vertical individually controlled bars, giving 28 degrees of freedom. The bars are circular with a diameter of 12 mm and are spaced apart by the grid mesh length $M = 100$ mm. Each bar is equipped with a series of square

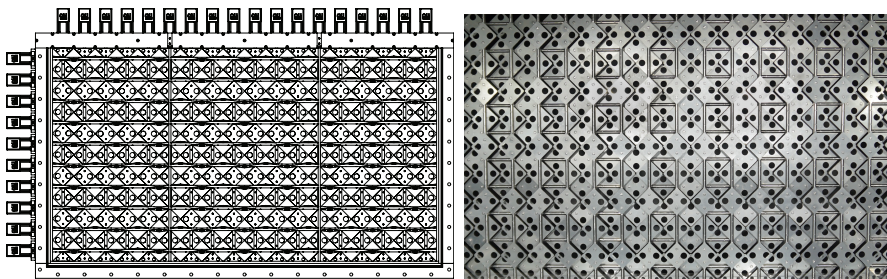


Figure 2.3: Water channel active grid schematic and and picture at full blockage taken from the test section.

wings mounted on alternating sides of the bars along the diagonal of the wing. Each wing is 100 mm along the diagonal and has two 24 mm circular holes to avoid maximum blockage of the flow through the grid. Along the edges, the remaining space is filled with triangular half wings with only one hole. The horizontal bars are supported with bearings through two additional equidistantly spaced support structures inside the grid. The total minimum and maximum blockage of the grid are 23% and 82%, respectively. For a more detailed description of the design of the water channel active grid, see [Li \(2022\)](#).

Wind tunnel active grid

The wind tunnel active grid is displayed in figure [2.4](#). Its dimensions are 2.71 m \times 1.80 m (width \times height), filling the entire cross-section of the wind tunnel. The grid is constituted of four quadrants, separated by horizontal and vertical support structures, each functionally forming an individual active grid similar to the water channel active grid. The full grid is made up of a total of 90 individually controlled bars, extending from the walls to the centre of the test section, where they sit in a bearing in the support structures. Two additional vertical support structures for the horizontal bars are placed equidistantly in the grid. The bars have a diameter of 12.7 mm and are spaced apart by $M = 100$ mm. They are controlled by stepper motors, 18 on each side and 27 both on top and bottom, giving 90 degrees of freedom. Each bar features square wings with a 97.6 mm diagonal, mounted in the same manner as for the water channel active grid. The wind tunnel active grid wings have no holes, as full blockage is less problematic in air compared to water, thus yielding a maximum blockage of close to 100% and a minimum blockage of 23%.

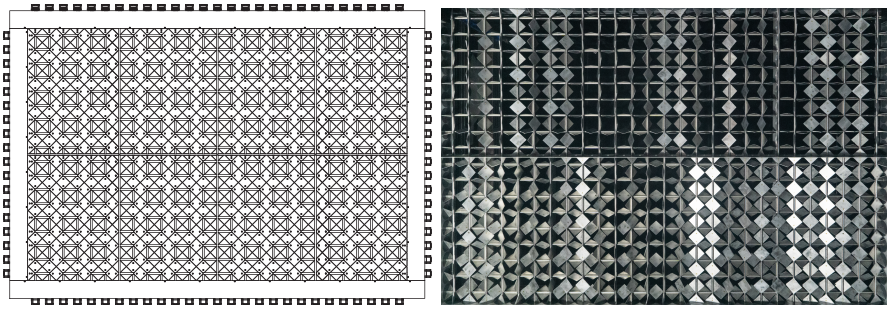


Figure 2.4: Wind tunnel active grid schematic and picture in motion from the test section.

Operation

Both active grids are operated in the same manner. While the water channel active grid is one coherent structure, the wind tunnel active grid consists of four individual active grids essentially. The following description applies to the water channel active grid, as well as every individual wind tunnel active grid quadrant. Each bar is controlled individually by a 28 STM23S-3RE stepper motor equipped with an encoder and a motion controller. A unique ASCII name is assigned to each motor, enabling individual control. The control protocols are written in Matlab with the commands based on the SiTM Command Language (SCL). The classically controlled parameters are rotational speed, acceleration/deceleration and period of actuation. For so-called *random* actuation modes, these quantities are varied randomly within a defined range, ascribed a certain distribution, e.g., top-hat or Gaussian. In articles I and IV, primarily, the rotational speed was varied within a top-hat distribution. A sequence of actuation parameters is generated for every motor, controlling the motion of the wings and thus the inflow condition into the water channel and wind tunnel, respectively. The other actuation mode used in this study is *flapping*, that is, oscillating the wings with a designated amplitude and frequency. By varying the amplitude between bars, a gradient in the velocity field can be generated. To avoid an imprint of one flapping frequency on the flow, the actuation is again varied randomly within a fixed frequency range. More details on the actuation parameters used are provided in the respective articles.

2.3 Building and turbine set-up

In articles II, III and IV, where the flow field and performance of a roof-mounted VAWT are examined, the same basic geometric set-up is used. The

set-up will be described in this section.

Model buildings and turbine positions

Al-Quraan et al. (2016) showed that wind tunnel measurements on geometrically simplified urban environments are a useful tool for wind resource assessment. In the present study, two cube-shaped buildings were used. Representing buildings as cubes has precedence in experimental (Ferreira and Ganapathisubramani, 2021; Dar et al., 2022) and numerical studies (Toja-Silva et al., 2013; Abohela et al., 2013; Ge et al., 2021; Zhang et al., 2022). A schematic of the set-up is shown in figure 2.5. The cubes have a height of $h = 100$ mm and are made out of Ebaboard 0600. They are placed in line with each other, spaced apart by $2h$. For articles II and IV they are aligned with the flow. Using two cubes in line with each other enables the study of a building relatively unaffected by its surroundings, as well as the study of a building in the immediate wake of another building. Martinuzzi and Havel (2000) studied the flow around two cubes in this arrangement for different spacings, with a second study (Martinuzzi and Havel, 2004) focusing specifically on the spacing $s/h = 2$. For $s/h < 1.4$, the flow reattaches somewhere on top of the downstream cube, whereas for $s/h > 3.5$, the flow reattaches in between the cubes. With increasing s/h , the flow conditions around the two cubes become approximately independent. For $s/h = 2$, the flow impinges on the windward top edge of the downstream cube and fluid from the sides is entrained in between the cubes, leading to increased turbulence intensities and vortex shedding. For Article III, the wind direction is varied by rotating the complete set-up in the wind tunnel. On top of the buildings, a VAWT was positioned. It was placed at three streamwise positions on each building (for Article III this also entailed a transverse variation for inflow directions $\neq 0^\circ$). The positions were $0.15h$ from the front edge, centred at $0.5h$ from all edges, and $0.85h$ from the front edge. In articles III and IV the vertical position of the turbine was also varied. Distances of $0.08h$ and $0.16h$ from the roof to the lower edge of the rotor swept area were examined, placing the centre of the rotor swept area $0.23h$ and $0.31h$ above the roof. For Article II only the lower turbine height was used.

Wind turbine

The turbine is a drag-driven VAWT of the Savonius type. The design was deliberately kept simple, as the goal of these studies was not to maximize the energy extraction by means of turbine design optimisation but rather to compare different influencing parameters, such as turbine position, wind

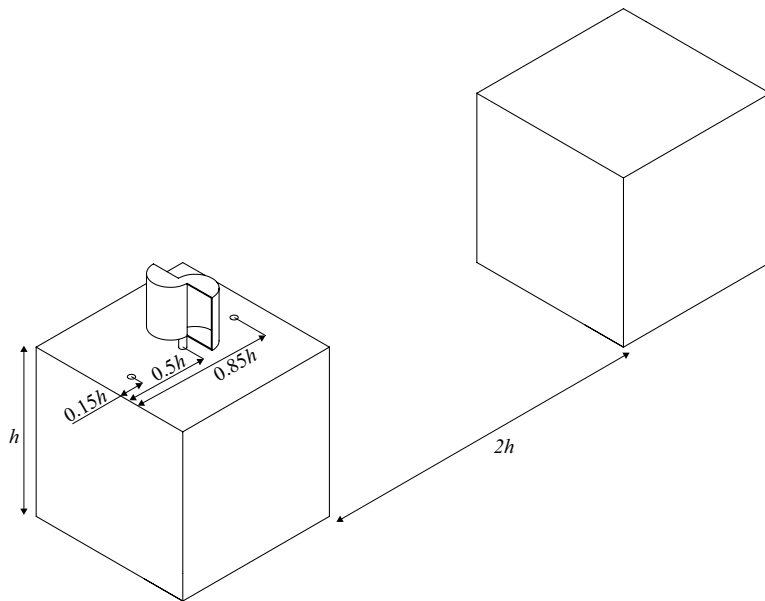


Figure 2.5: Geometric set-up of the two model buildings including the roof-mounted VAWT.

direction and inflow conditions. Moreover, a simple design is easily replicated in both other experimental and numerical studies. A schematic of the turbine is shown in figure 2.6. It has a turbine diameter $d_T = 0.4h$ and a blade height $h_T = 0.3h$. The turbine-to-building size ratio is comparable to real-world examples, e.g., the VAWTs on the Greenpeace headquarters in Hamburg, and similar studies on urban wind energy, e.g. Zhang et al. (2022) and Dar et al. (2022). The turbine design was inspired by seminal works on VAWTs by Alexander and Holownia (1978) and Akwa et al. (2012). The blade cross-section consists of two overlapping semicircles. The overlap is added to reduce the starting torque (Kumbernuss et al., 2012). The bottom and top are covered with semicircular end plates. The turbines were 3D-printed out of polylactide acid (PLA) with a resolution of $20 \mu\text{m}$ along the turbine height and $2 \mu\text{m}$ in all other directions. The turbine shaft has a diameter of $0.04h$ and elevates the turbine $0.08h$ and $0.16h$ above the roof for the low and high turbine positions, respectively. The turbine is significantly scaled down compared to a real full-scale turbine, as commonly done in lab-scale studies of wind turbines (e.g. Cal et al. (2010); Bartl et al. (2012); Bottasso et al. (2014); Naumov et al. (2014); Schottler et al. (2016); Bastankhah and Porté-Agel (2016); Bredmose et al. (2017); Neun-

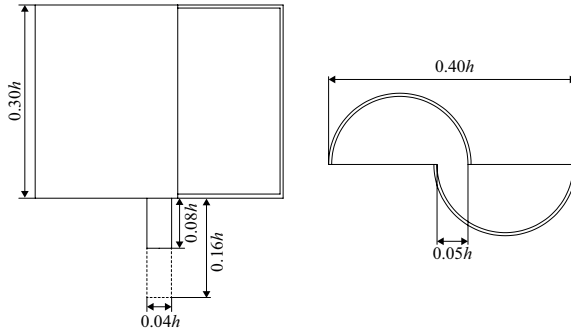


Figure 2.6: Savonius type VAWT used in articles II, III and IV. Note, the low turbine position used in all studies is displayed, with the high turbine position superimposed in dashed lines.

aber et al. (2020); Li et al. (2020); Segalini and Dahlberg (2020); Helvig et al. (2021); Gambuzza and Ganapathisubramani (2021)). Dynamic similarity, i.e., matching Reynolds numbers, is difficult to achieve at lab-scale. The value of these studies is examining the problem at hand in a controlled environment, such as a wind tunnel, and identifying the underlying trends. In this study, the turbine is particularly scaled down to enable a realistic turbine-to-building size ratio while keeping the buildings at a size that allows for the capture of the complete flow field around the set-up with Particle Image Velocimetry (more details in section 2.5.1). Both the model buildings and the turbine are coated with matte black paint to minimize light reflections for the laser-based measurements in articles II and IV.

2.4 Power measurements

To evaluate the performance of the turbine, the power it extracts needs to be measured. Figure 2.7 illustrates the conversion of power in an electricity-producing wind turbine. The available power in the wind, P_a , (see equation 1.1), often used for wind resource assessment, makes the turbine spin, converting the power to mechanical power, P_m . Naturally, not the complete available power can be captured. The conversion factor is the power coefficient, C_P (see equation 1.2). The mechanical power is the product of the mechanical torque, Q , acting on the turbine shaft and the rotational frequency of the turbine, Ω_T (see equation 1.3). The turbine is connected to a generator, where the rotational energy is converted to electrical power, $P_e = VI$, with the terminal voltage, V , and the electrical current, I . To directly evaluate the performance of the turbine, the quantity of interest

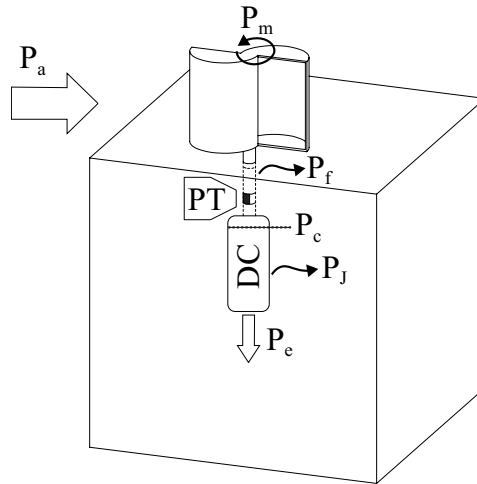


Figure 2.7: Power conversion in a roof-mounted VAWT.

is P_m , as the conversion to P_e includes friction losses, P_f , and, more importantly, electrical losses, P_J , which are highly generator dependent (Kang and Meneveau, 2010). However, measuring P_m directly is difficult, especially for miniature wind turbines, due to very low torque values and spatial constraints (Bastankhah and Porté-Agel, 2017). A way around this is to measure the converted power P_c (W) that is available to the generator. The converted power only differs from the mechanical power by the friction losses; $P_c = P_m - P_f$. It is defined as:

$$P_c = Q_e \Omega_e, \quad (2.1)$$

based on the electromagnetic torque, Q_e (Nm), and the rotational velocity of the armature in the generator, Ω_e (1/s). Since no gear train was used in the present study $\Omega_e = \Omega_T$. Bastankhah and Porté-Agel (2017) showed that measuring P_c and estimating P_f is a reliable way of obtaining P_m , with a good collapse between $P_c + P_f$ and P_m . A brushed DC motor is used as a generator in their study as well as in the present work (10NS61 Athlonix for Article II and 12G88 Athlonix for articles III and IV). The electrical circuit of a DC generator is displayed in figure 2.8. The inductance, L , is only relevant for dynamic changes of I , and is negligible in steady state operation (Hughes and Drury, 2013). The electromagnetic torque is what is left of the mechanical torque on the turbine shaft after the friction losses. In a DC generator, Q_e (Nm) is proportional to the electrical current I (A):

$$Q_e = K_T I, \quad (2.2)$$

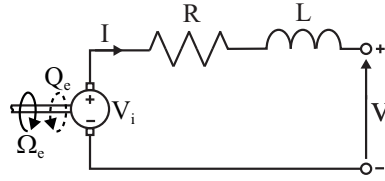


Figure 2.8: Electrical circuit of a DC Generator, adapted from [Bastankhah and Porté-Agel \(2017\)](#).

with the proportionality constant K_T (Nm/A), also known as the torque constant, which can also be expressed as the electromotive force (EMF) constant. The value of K_T is solely dependent on the generator properties and constant across generator operation. The rotation of the armature induces a voltage, V_i (V). The EMF constant relates the rotation of the armature in the generator to the induced voltage:

$$V_i = K_T \Omega_e, \quad (2.3)$$

which is different from the terminal voltage $V = V_i - RI$. This illustrates the issue of measuring P_e directly based on V . Equation 2.2 enables the determination of Q_e , based on a measurement of the electrical current, I . Together with a measurement of $\Omega_e = \Omega_T$, the converted power can be calculated. The realisation of this in the present work is shown schematically in figure 2.9. I is measured over a 0.1 Ohm shunt resistor with an INA219 High Side DC Current Sensor. Ω_T is measured with a reflective object sensor (OPB705WZ). Infrared light is emitted on the turbine shaft, which is made half reflective. The fluctuating reflected light is then collected by a phototransistor, which results in a sinusoidal signal, of which Ω_T can be deduced. To avoid aliasing, the signal is always sampled at a frequency at least double the maximum rotation rate. All signals are collected with a microcontroller (Arduino Uno). This is also used to control the operation of the turbine. A high frequency variable switch (IRF540NPbF) opens and closes at a frequency set in the microcontroller and thus controls I and, in turn, also Ω_T . A similar wind turbine control was used, for example, by [Gambuzza and Ganapathisubramani \(2021\)](#).

The mechanical power is calculated as the sum of P_c and P_f . The friction losses are estimated based on the motor specifications. Finally, the power coefficient, C_P , is calculated (see equation 1.2). The uncertainty of C_P and the tip speed ratio, λ is calculated based on the propagation of random and biased error of all contributing factors. This is given by equation 2.4 for a

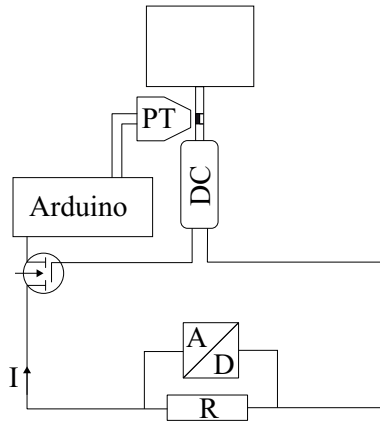


Figure 2.9: Electrical circuit of the current and rotational velocity measurement set-up.

variable $F = x_1^a x_2^b \dots x_n^N$ (Wheeler and Ganji, 1996):

$$\frac{\sigma_F}{F} = \sqrt{\left(a \frac{\sigma_1}{x_1}\right)^2 + \left(b \frac{\sigma_2}{x_2}\right)^2 + \dots + \left(N \frac{\sigma_n}{x_n}\right)^2}, \quad (2.4)$$

where σ_n is the sum of the biased and random error of x_n . The random error in the measurement of Ω_T and I is determined through a convergence measurement. Based on this sampling times of 2 minutes for Ω_T and 1 minute for I were determined. Longer measurements would not have reduced the random error significantly. Bias errors are determined based on manufacturer data of the respective measurement instruments. That does not include potential bias errors introduced by human errors, such as misalignment of the turbine or the cubes. A conscious effort was made to minimize these. Overall this yielded a maximum error of 8.8% for C_P and 3.5% for λ with a 95% confidence interval in [Article II](#). With a refined set-up for [articles III](#) and [IV](#) these were reduced to 3.5% and 1.5% for C_P and λ , respectively. Error bars on λ and C_P are plotted in all power curves, as well as in any other presentation of C_P .

2.5 Flow measurements

To gain a deeper understanding of the mechanisms that govern the wind power extraction and the interaction of FST with an evolving TBL, high-fidelity flow measurements were conducted. The primary measurement techniques used were Particle Image Velocimetry (PIV) for [articles II](#) and [IV](#)

and Laser Doppler Velocimetry (LDV) for [Article I](#). In addition, [Article IV](#) includes hot-wire measurements of the background flow. [Article III](#) primarily focused on wind turbine power measurements (described in section 2.4), complemented by surface pressure measurements on the buildings.

2.5.1 Particle Image Velocimetry

Particle Image Velocimetry is a measurement technique that allows for the measurement of instantaneous velocity fields. In this description, the focus will be on planar PIV (2D), as this is what has been used in the present experimental studies. For more details on PIV the reader is referred to [Raffel et al. \(2018\)](#). The basic elements of PIV are:

- A) Seeding, i.e., tracer particles following the flow
- B) Illumination of the particles
- C) Image acquisition
- D) Processing, i.e. correlating subsequent images

To ensure that tracer particles follow the flow, it is a prerequisite that they are approximately neutrally buoyant, i.e. the particle density approximately matches the fluid density; $\rho_p/\rho_f \approx 1$. That is often difficult to fulfil in gas flows. To assess how well a particle follows the flow, the Stokes number is considered:

$$St = \frac{\tau_p}{\tau_f}, \quad (2.5)$$

which is the ratio between the particle's response time, τ_p (s), and the characteristic time scale of the fluid, τ_f (s), that one desires to resolve. The smaller the Stokes number is, the better the particles follow the flow. For $St < 0.1$ the error due to particle tracing can be deemed negligible ([Raffel et al., 2018](#)).

The particles need to be illuminated to make them visible. The illumination has to be short, i.e., the particle should not move more than one pixel during an illumination. To obtain sufficient light scattering by the particles in such a short time period, the light has to be of high intensity; thus, typically, lasers are utilised as a light source. Optics, such as lenses and mirrors, are used to generate and position a light sheet. A camera, synchronized with the light source, acquires instantaneous images of the illuminated particles in the flow.

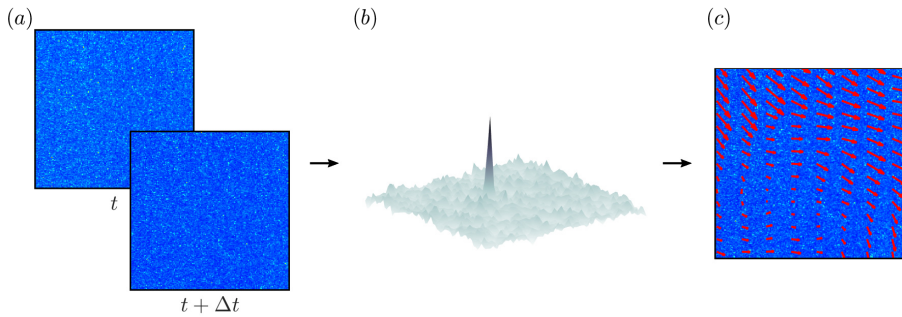


Figure 2.10: Basic principle of Particle Image Velocimetry. (a) Two raw images, (b) Example correlation peak, (c) Resulting vector field.

Figure 2.10 illustrates the path from particle images to a velocity field. Two images are taken in quick succession, with a fixed time delay Δt (figure 2.10 (a)). Image one is then divided into smaller regions or interrogation windows. For every interrogation window, the cross-correlation between two subsequent images reveals the most likely particle displacement. This is indicated by the position of the cross-correlation peak, as displayed in figure 2.10 (b). Based on the displacement and Δt a velocity vector for every interrogation window is calculated. These can be combined to obtain a flow field, as seen in figure 2.10 (c). Finally, these vectors are transformed from image space into physical space based on calibration images taken with a reference scale in the plane of interest. The uncertainty in the velocity based on the cross-correlation is calculated in LaVision DaVis as per Wieneke (2015), Neal et al. (2015) and Sciacchitano and Wieneke (2016). The uncertainty is up to 5% of the freestream velocity in the recirculation region in the worst case and below 1% in the freestream. With averaging over a minimum of 1000 images (2000 images for the more turbulent cases), the uncertainty is reduced to $\approx 1\%$ in the recirculation region and $\approx 0.4\%$ in the freestream. This accounts for the random error associated with the measurement method.

The PIV set-up was slightly different for articles II and IV. This is schematically displayed in figure 2.11. For Article II a dual-pulsed Litron Nd-YAG laser (Nano L200-15 PIV) was used together with two LaVision Imager LX 16 mega-pixel cameras with Sigma DG 180 mm lenses capturing a field of view (FOV) of 200 mm \times 250 mm each. The building set-up used, described in section 2.3, spans 400 mm \times 100 mm, not including the roof-mounted turbine. To capture a full picture of the flowfield around the buildings and the turbine, the flow was measured in three separate acquisitions yielding a

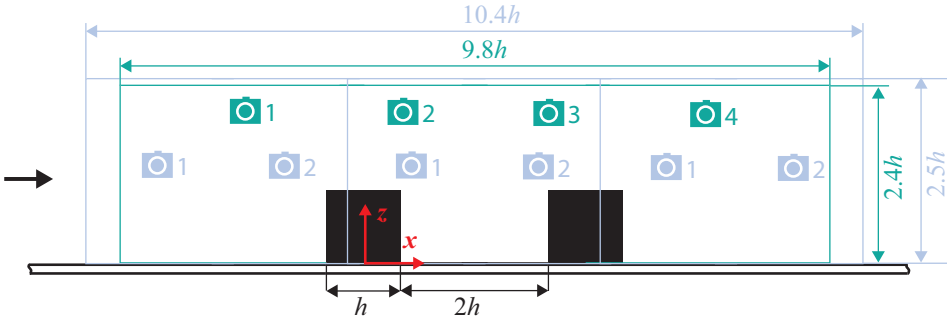


Figure 2.11: PIV set-up for [Article II](#) and [Article IV](#), showing the respective resulting field of views.

total FOV of $1040 \text{ mm} \times 250 \text{ mm}$ ($x \times z$). In [Article IV](#), two Nano L200-15 PIV lasers were used simultaneously, together with two LaVision Imager LX 16 mega-pixel cameras with Nikon 200 mm lenses and two LaVision Imager MX 25 cameras with Zeiss 100 mm lenses. Thus, a total FOV of $980 \text{ mm} \times 240 \text{ mm}$ ($x \times z$) was captured in one acquisition. An overlap of at least 10% was ensured between individual fields for both studies. In [Article IV](#), one calibration for all four cameras was conducted; thus, the vectors were mapped on one global coordinate system. In the overlap region, the velocities were averaged between the two respective cameras. In [Article II](#), a linear weighting was conducted in the overlap region, starting from 0 at the outer edge of the field, up to 1, where the overlap region concludes inside the field. Figure 2.12 illustrates the merging of two fields for one instant in time. In both studies, a clean fit between the fields was achieved, with no apparent discontinuity.

2.5.2 Laser Doppler Velocimetry

Laser Doppler Velocimetry is a non-intrusive point measurement technique based on the Doppler effect. Similar to PIV, the flow needs to be seeded with particles to utilise LDV. For LDV, a small measurement volume is illuminated by two laser beams. Practically this is done by splitting a laser beam in two. The beams are then directed such that they intersect at a certain distance - the focal length f . The region where the beams intersect is the measurement volume. When a particle passes through the measurement volume, it reflects the light partly back to the receiver. This is illustrated schematically in figure 2.13, where the unit vectors e_1 , e_2 and e_s indicate the direction of the light. Considering one beam to begin with, the light moves at a velocity c (m/s) and with a frequency f_1 (1/s) when it hits the

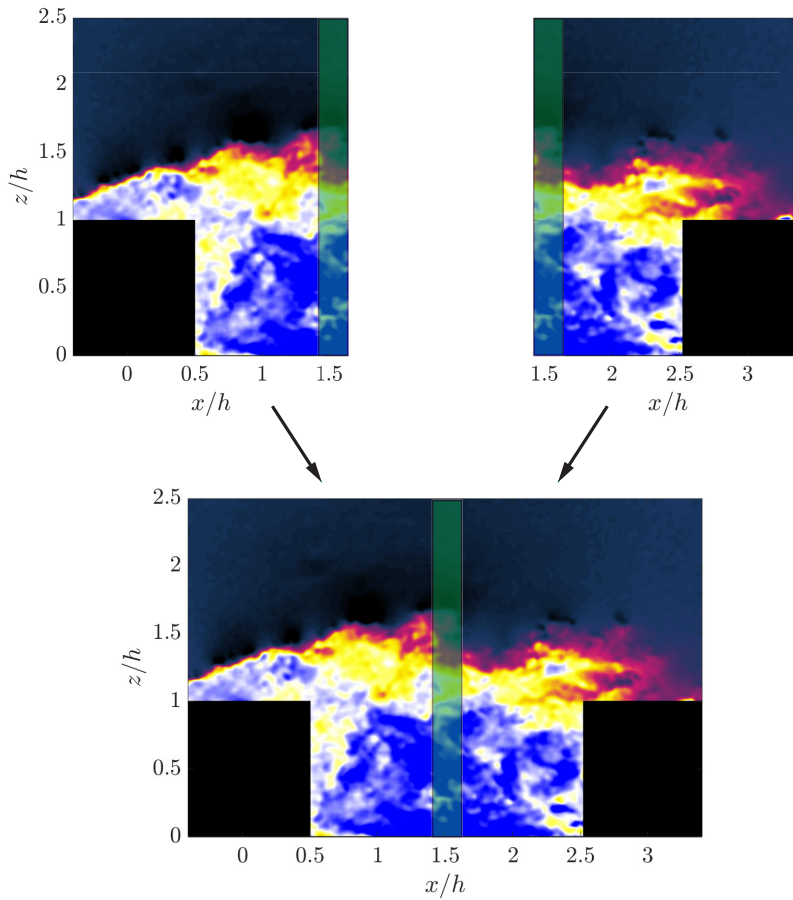


Figure 2.12: Stitching of two instantaneous PIV images. The velocities in the overlap region, marked in green, are averaged (linearly weighted for [Article II](#)) between the two individual fields.

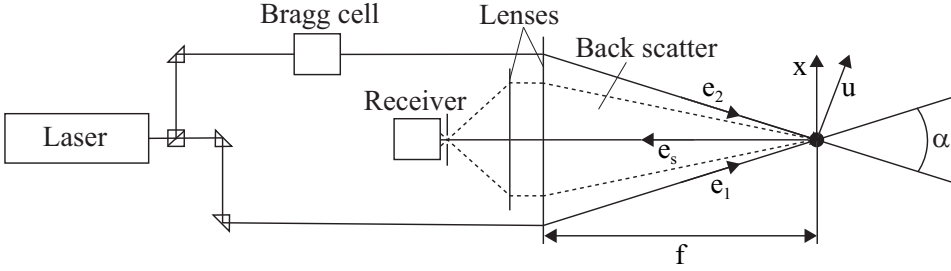


Figure 2.13: Basic principle of Laser Doppler Velocimetry in a back scatter configuration.

seeding particle. However, due to the instantaneous velocity u (m/s) of the seeding particle, the perceived frequency that is scattered back, f_s (1/s), is different. The particle acts as a moving emitter and thus induces the Doppler shift. The returned frequency can be described based on Doppler theory (with $u \ll c$):

$$f_{s,i} = f_i \left[1 + \frac{u}{c} (e_s - e_i) \right], \quad (2.6)$$

with $i = 1$ and 2 for beam one and two, respectively. When two frequencies of different magnitude interfere, a new frequency arises, the Doppler frequency:

$$f_D = f_{s,2} - f_{s,1}. \quad (2.7)$$

Since the two beams originate from the same laser beam, $f_1 = f_2$ and f_D can be reduced to:

$$\begin{aligned} f_D &= f_1 \left[\frac{u}{c} (e_1 - e_2) \right] \\ &= \frac{1}{\Lambda} 2 \sin \left(\frac{\alpha}{2} \right) u_x, \end{aligned} \quad (2.8)$$

with the wavelength of the laser, Λ (m), and the angle between the two incoming beams, α , both known quantities. f_D is much lower than f_1 and can be readily measured from the reflected light. Thus, u_x can be determined:

$$u_x = \frac{\Lambda}{2 \sin \left(\frac{\alpha}{2} \right)} f_D. \quad (2.9)$$

A problem with this formulation is that the direction of u_x is ambiguous. The same Doppler frequency would arise for particles travelling in opposite directions at the same velocity. To avoid this, one of the beams is frequency

shifted by a set frequency, f_0 , using a Bragg cell, yielding:

$$u_x = \frac{\Lambda}{2 \sin\left(\frac{\alpha}{2}\right)} (f_D - f_0). \quad (2.10)$$

To measure multiple velocity components, two additional laser beams at a different wavelength, directed at the same measurement volume, are required. Advantages of LDV are its non-intrusive nature, the absolute linearity of the measurement, i.e., no calibration is required, as well as good temporal resolution. In addition, the small measurement volume allows for fine spatial resolution, e.g., for boundary layer scans. In [Article I](#), a two-component LDV system was used. However, for most measurements, only the streamwise velocity component was acquired. A 60 mm Dantec FiberFlow probe with a beam expander was used with a 500 mm lens, resulting in a measurement volume of $119 \mu\text{m} \times 119 \mu\text{m} \times 1590 \mu\text{m}$ ($dx \times dy \times dz$). The laser wavelength was 514.5 nm, and the data was acquired in backscatter mode, meaning the reflected light was received by the same FiberFlow probe. Each measurement was sampled for 10 minutes. The random error of the LDV measurements was determined based on a 20 minute convergence sample of the most turbulent case. Only a 0.4% variation in the variance was found between individual 10-minute samples and the full sample.

LDV measurements intrinsically entail a velocity bias towards higher velocities ([McLaughlin and Tiederman, 1973](#)). This is caused by an increased volume of fluid passing through the measurement volume for higher velocities. It can be corrected for by weighting the measurements by the transit time Δt , which is the time the respective particle spends in the measurement volume. The transit time is recorded together with f_D . For the mean velocity, this yields:

$$U = \frac{\sum_i u_i \Delta t_i}{\sum_i \Delta t_i}. \quad (2.11)$$

The velocity variance is calculated analogously:

$$u'^2 = \frac{\sum_i (u_i - U)^2 \Delta t_i}{\sum_i \Delta t_i}. \quad (2.12)$$

A drawback of LDV is its non-constant sampling rate. The recordings are determined by particles passing through the measurement volume, which occurs in random time intervals. This complicates spectral analysis. To overcome this, the data is resampled. There are various methods to accomplish this (see e.g. [Boyer and Searby \(1986\)](#); [Adrian and Yao \(1986\)](#);

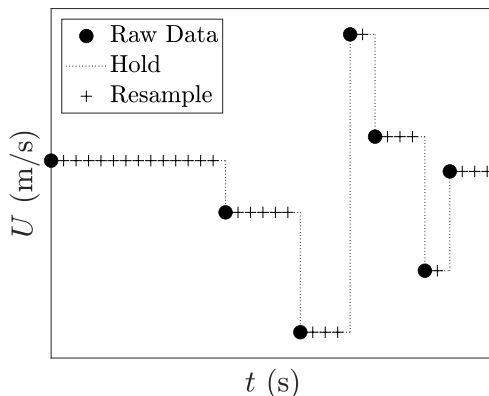


Figure 2.14: Example sample and hold reconstruction.

Ouahabi et al. (1998); Benedict et al. (2000)). In Article I, a simple sample and hold reconstruction was used (Boyer and Searby, 1986; Adrian and Yao, 1986). This is illustrated in figure 2.14. Essentially a sampled value is held until a new value is recorded. Then the data is resampled onto the held function with an equidistant time step. Fast Fourier transforms and correlations can then be computed simply on this uniformly spaced resampled data.

2.5.3 Constant temperature anemometry

The background flow for Article IV is measured with hot-wire anemometry, more specifically Constant Temperature Anemometry (CTA). Since its sole purpose in the present investigation is to provide information on the spectral distribution of energy of the background flow, only a very brief overview will be given here. CTA is a point measurement technique. The basis of CTA is the relation between convective heat transfer and fluid velocity. A sensor is heated and placed in the flow. Typically, very fine wire sensors are used, resulting in high temporal and spatial resolution of the measurement. The heat transfer between the wire and the flow is then related to the flow velocity. The wire is part of a Wheatstone bridge and heated by an electrical current, I . The temperature of the sensor is kept constant by adjusting the bridge voltage, E (V), whenever the flow velocity and thus the heat transfer changes. The bridge voltage thus becomes a measure of the velocity. This relation can be expressed for small cylinders by King's law (King, 1914):

$$E^2 = (T_w - T_f)(A + BU^{0.5}), \quad (2.13)$$

with the wire temperature, T_w (K), fluid temperature, T_f (K), and constants A and B . To solve this for U (m/s) it is typically expressed as a polynomial. In the present study a polynomial of fourth order was used. The hot-wire was calibrated pre- and post-measurements against a Pitot-static tube. The fluid temperature was recorded simultaneously with a Dantec Resistance Temperature Detector, which was used for a temperature correction, as per [Hultmark and Smits \(2010\)](#). The sensor used in this study is a Dantec 55P11 single hot-wire probe with a 5 μm diameter and a length of 1.25 mm. It was operated at a constant overheat ratio of 1.8. The data was sampled at a frequency of 75 kHz with a 30 kHz analog low pass filter to acquire information on the spectral distribution of energy in the flow. This is sufficiently high to resolve the Kolmogorov frequency, which was approximately 10 kHz in the flows in [Article IV](#).

2.5.4 Surface pressure measurements

In [Article III](#), the surface pressure on one of the model buildings was measured to obtain information on the flow patterns for different wind directions. Only a brief description of the methodology is given here, as it is only a complementary measurement for one of the studies. More details on the hardware are found in [Li \(2022\)](#). Sixty-one (61) pressure taps were distributed on the cube and sampled simultaneously (only the 13 pressure taps on the roof of the cube featured in the analysis in [Article III](#)). A Scanivalve MPS4264 miniature pressure scanner was used to measure the pressure. The pressure scanner sampled all ports for 60 s at a frequency of 800 Hz with an accuracy of $\pm 0.20\%$ or 2 Pa. This is sufficiently high to acquire the desired mean static pressure around the cube. The recorded pressures were well within the range of 995 Pa of the pressure scanner. The reference pressure was acquired from the static port of a Pitot-static tube.

Chapter 3

Summaries of the research articles and future work

This thesis contributes to the understanding of urban wind resources. An experimental investigation is presented, ranging from a fundamental level, studying a turbulent boundary layer subjected to freestream turbulence, to the assessment of a model-scale roof-mounted wind turbine in various positions and flow conditions. Chapter 1 outlined the background for the thesis, introducing the relevant research in the field to date and motivated the present work, outlining the research questions. In chapter 2, the experimental methods used to study these questions were presented. This ranged from the geometric set-up of model buildings and turbines and the associated turbine power measurements to the various flow measurement techniques employed. In the following, the research results are presented in the form of four articles. These are briefly summarized here, followed by an outlook of potential future work on the topic.

3.1 Summaries of the articles

[Article I](#)

Spatial development of a turbulent boundary layer subjected to freestream turbulence

Yannick Jooss, Leon Li, Tania Bracchi and R. Jason Hearst
Journal of Fluid Mechanics, **911**, A4, (2021).

Wind turbines are generally placed in the atmospheric boundary layer. In urban environments, the boundary layer flow is additionally subjected to

high levels of turbulence. While the impact of freestream turbulence (FST) on a turbulent boundary layer (TBL) is well documented, the spatial evolution of this flow has not been investigated. FST is known to mature the TBL ahead of its natural evolution, resulting in e.g., in the suppression of the wake region, an increased near-wall variance peak and the emergence of an outer spectral peak. This posed the question of how a TBL would evolve from this matured state. [Article I](#) addresses this with the examination of the spatial development of a TBL subjected to various levels of FST. This is investigated experimentally in a water channel. The FST is generated with an active grid, yielding four levels of u'_{∞}/U_{∞} from 3.2% to 12.5%. The boundary layer is measured with Laser Doppler Velocimetry at three streamwise positions. A distinct influence of the FST on the evolution of the TBL is found in the mean statistics. The initially suppressed wake region reemerges as the TBL evolves and the FST decays. Similarly, the initially increased near-wall variance peak for high u'_{∞}/U_{∞} decreases as the TBL evolves in space. This is also reflected in the spectral distribution of energy. An outer spectral peak imprinted by high u'_{∞}/U_{∞} decreases in a spatially developing TBL. Overall this indicates that the FST does not permanently mature the TBL ahead of its natural evolution. It is explicitly shown that it is insufficient to assess a TBL only based on individual parameters, such as Re_{τ} , u'_{∞}/U_{∞} or $L_{u,\infty}/\delta$, but the relative states of evolution of the TBL and the FST have to be considered as well.

[Article II](#)

Flow field and performance of a vertical axis wind turbine on model buildings

Yannick Jooss, Roberto Bolis, Tania Bracchi and R. Jason Hearst
Flow, **2**, E10, (2022).

This study examines the flow field and performance of a roof-mounted wind turbine on model buildings. Roof-mounted wind turbines are typically placed in the roughness sublayer. Here the flow is strongly dependent on the local topology. Thus, the positioning of a wind turbine on a building has significant implications for the power output of the turbine. To date, this is usually studied by examining the flow around one or multiple buildings, deducing the available power at different locations from the velocity (see equation 1.1). In [Article II](#), a Savonius-type VAWT is placed on model buildings, directly examining the flow around a roof-mounted wind turbine

in a wind tunnel. The flow field is acquired using PIV. Simultaneously the power output of the turbine is measured. Two buildings are examined, one relatively unaffected by its surrounding and one immediately in the wake of the first building. The turbine position is varied, with three positions on each building. The turbine experiences a wide range of flow conditions at the different positions, resulting in high variations in the power output of up to 84%. The highest power output is recorded at the front and centre of the upstream building. On the downstream building, the most downstream location yielded the highest power output. Most significantly, this study demonstrates how the VAWT interacts with the flow. Upstream blockage effects are a known phenomenon for wind turbines, however, this study shows an influence of the roof-mounted VAWT on the flow extending beyond that. The influence depends strongly on the underlying flow conditions and thus on the turbine position. This has a substantial impact on the power output of the turbine itself, showing the significance of including an actual turbine in these kinds of studies.

Article III

Influence of position and wind direction on the performance of a roof-mounted vertical axis wind turbine

Yannick Jooss, Eivind Berg Rønning, R. Jason Hearst and Tania Bracchi
Under consideration for publication in *Journal of Wind Engineering & Industrial Aerodynamics*

The goal of this study is to obtain a better understanding of the ideal position for a roof-mounted VAWT. [Article III](#) builds on the results from [Article II](#). The same principal set-up is employed, consisting of two model buildings and a Savonius-type VAWT. The parameter space is expanded from [Article II](#), by including variations of the turbine height and the wind direction in addition to the different turbine positions. Five different wind directions are simulated by rotating the set-up in the wind tunnel. Together with the three positions on a building and the two examined turbine heights, a total of 30 different cases are explored, with full power curves for each of them. A higher turbine position increases the overall power output and makes it less dependent on its position. Particularly, for wind normal to the faces of a building, the power output is increased compared to the low turbine. For wind along the diagonal of a building, the low turbine position recorded slightly higher power output. Generally, wind along the diagonal

yielded the highest power output. All wind directions considered, assuming a uniform wind rose, the central position on a building is found to be ideal for power extraction.

Article IV

Influence of incoming turbulence and shear on the flow field and performance of a lab-scale roof-mounted vertical axis wind turbine

Yannick Jooss, R. Jason Hearst and Tania Bracchi

Under consideration for publication in *Wind Energy*

In [Article IV](#) the influence of turbulence intensity and velocity shear on a roof-mounted VAWT are examined. The flow in an urban environment is typically sheared and highly turbulent. The interaction of these is complex, as discussed by [Article I](#). The same set-up as in articles [II](#) and [III](#), with two model buildings and a roof-mounted Savonius-type VAWT, is employed. The inflow is varied with an active grid, generating five different inflow conditions with turbulence intensities u'_{∞}/U_{∞} from 0.9% to 11.5% and vertical shear $\Delta U(z)/U_{\infty}$ from 0% to 17%. The power output of the turbine is measured at six streamwise positions and two heights while the flow field is captured with PIV. This totals 60 independent cases, with a full power curve recorded for each of them. It is apparent from this study that the influence of turbulence intensity on the flow field is substantially higher than that of shear. Specifically, the recirculation region above the upstream cube is significantly reduced by increasing levels of u'_{∞}/U_{∞} , leading to higher velocities above the roof of the buildings. This is also reflected in the power measurements, where only limited changes were observed for variations in $\Delta U(z)/U_{\infty}$, while changes in u'_{∞}/U_{∞} affected the turbine performance significantly.

3.2 Future work

This work could be extended in a number of different directions. The study in [Article I](#) could be expanded to more closely match an atmospheric boundary layer and study its evolution. One approach could be to introduce roughness to simulate an urban boundary layer. Another method is to employ an active grid to tailor the inflow to generate a variety of combinations of shear and turbulence intensity ([Hearst and Ganapathisubramani, 2017](#)). Studying the evolution of these kinds of flows is of great relevance to the experimental research of wind turbines and farms. Both turbulence intensity and shear decay in a wind tunnel with increasing distance from their origin. This poses issues for any flow-related study extending over a significant streamwise distance, e.g., the flow around a building array or the study of wind turbine wakes. Exploring the possibilities of an active grid to achieve close to constant shear and turbulence intensity over an extended region would thus be of great relevance.

The set-up used in articles [II](#), [III](#) and [IV](#), employing a direct measurement of the power output of a roof-mounted VAWT, generates a lot of new potential research questions in the field of urban wind energy. The building arrangement could be varied, exploring a different spacing between the buildings, a staggered arrangement, or involving additional buildings. Similarly, the building shape could be varied, examining different aspect ratios and shapes. While some of these configurations have been studied, rarely an actual turbine has been involved. As demonstrated in [Article II](#), this is of great significance and could potentially complement and update some of these studies. Examining the robustness of these findings, specifically the impact of the turbine on the flow field, to different turbine types and different turbine-to-building size ratios would be a logical next step. The flow fields in [Article II](#) (figures 6 and 7) give insight into how the available power in the surrounding of a roof-mounted VAWT, e.g. on a neighbouring building, is affected by the presence of a turbine. To examine this explicitly, a second wind turbine could be introduced, measuring the power output directly. Another direction would be to study the same set-up, employing different measurement techniques; [Articles II](#) and [IV](#) both use planar PIV along the centre line of the set-up. Stereoscopic PIV would be a possibility to also quantify the out-of-plane motion, and with tomographic PIV, a three-dimensional flow field could be assessed to improve the understanding of the full flow field.

Finally, the developed miniature wind turbine set-up could be used to study

different applications. [Dabiri \(2011\)](#) suggests a potential order of magnitude enhancement of wind farm power with counter-rotating VAWTs. This could be studied systematically at lab-scale by multiplying the current set-up, varying parameters such as turbine spacing, size and type, as well as wind direction. VAWTs have also generated increased interest in the context of offshore floating wind turbines ([Borg et al., 2014](#); [Hand and Cashman, 2020](#)). Combining the set-up with a multiple degrees of freedom actuator could enable a controlled study of power extraction with a VAWT in the dynamic environment of a floating platform. With some modifications, the set-up could also be adapted to measure the power output of HAWT.

Bibliography

- I. Abohela, N. Hamza, and S. Dudek. Effect of roof shape, wind direction, building height and urban configuration on the energy yield and positioning of roof mounted wind turbines. *Renewable Energy*, 50:1106–1118, Feb. 2013. ISSN 0960-1481. doi: 10.1016/j.renene.2012.08.068.
- S. Acarer, C. Uyulan, and Z. H. Karadeniz. Optimization of radial inflow wind turbines for urban wind energy harvesting. *Energy*, 202:117772, July 2020. ISSN 0360-5442. doi: 10.1016/j.energy.2020.117772.
- M. S. Adaramola and P. Å. Krogstad. Experimental investigation of wake effects on wind turbine performance. *Renewable Energy*, 36(8):2078–2086, Aug. 2011. ISSN 0960-1481. doi: 10.1016/j.renene.2011.01.024.
- A. M. Adil and Y. Ko. Socio-technical evolution of Decentralized Energy Systems: A critical review and implications for urban planning and policy. *Renewable and Sustainable Energy Reviews*, 57:1025–1037, May 2016. ISSN 1364-0321. doi: 10.1016/j.rser.2015.12.079.
- R. J. Adrian and C. S. Yao. Power spectra of fluid velocities measured by laser Doppler velocimetry. *Experiments in Fluids*, 5(1):17–28, Jan. 1986. ISSN 1432-1114. doi: 10.1007/BF00272419.
- D. O. Akinyele, N. K. C. Nair, R. K. Rayudu, and B. Chakrabarti. Decentralized energy generation for end-use applications: Economic, social and environmental benefits assessment. In *2014 IEEE Innovative Smart Grid Technologies - Asia (ISGT ASIA)*, pages 84–89, May 2014. doi: 10.1109/ISGT-Asia.2014.6873769.
- J. V. Akwa, H. A. Vielmo, and A. P. Petry. A review on the performance of Savonius wind turbines. *Renewable and Sustainable Energy Reviews*, 16

- (5):3054–3064, June 2012. ISSN 1364-0321. doi: 10.1016/j.rser.2012.02.056.
- A. Al-Quraan, T. Stathopoulos, and P. Pillay. Comparison of wind tunnel and on site measurements for urban wind energy estimation of potential yield. *Journal of Wind Engineering and Industrial Aerodynamics*, 158: 1–10, Nov. 2016. ISSN 0167-6105. doi: 10.1016/j.jweia.2016.08.011.
- A. J. Alexander and B. P. Holownia. Wind tunnel tests on a Savonius rotor. *Journal of Wind Engineering and Industrial Aerodynamics*, 3(4):343–351, Jan. 1978. ISSN 0167-6105. doi: 10.1016/0167-6105(78)90037-5.
- A. D. Aliferis, M. S. Jessen, T. Bracchi, and R. J. Hearst. Performance and wake of a Savonius vertical-axis wind turbine under different incoming conditions. *Wind Energy*, 22(9):1260–1273, June 2019. ISSN 1099-1824. doi: <https://doi.org/10.1002/we.2358>.
- M. M. Aslam Bhutta, N. Hayat, A. U. Farooq, Z. Ali, S. R. Jamil, and Z. Hussain. Vertical axis wind turbine – A review of various configurations and design techniques. *Renewable and Sustainable Energy Reviews*, 16(4): 1926–1939, May 2012. ISSN 1364-0321. doi: 10.1016/j.rser.2011.12.004.
- A. Ataei, M. Biglari, M. Nedaei, E. Assareh, J.-K. Choi, C. Yoo, and M. S. Adaramola. Techno-economic feasibility study of autonomous hybrid wind and solar power systems for rural areas in Iran, A case study in Moheydar village. *Environmental Progress & Sustainable Energy*, 34(5): 1521–1527, 2015. ISSN 1944-7450. doi: 10.1002/ep.12121.
- Atkins. Bahrain World Trade Center, 2008. URL <https://www.atkinsglobal.com/en-GB/projects/bahrain-world-trade-center>. Accessed June 2019.
- J. Bartl, F. Pierella, and L. Sætran. Wake measurements behind an array of two model wind turbines. *Energy Procedia*, 24:305–312, Jan. 2012. ISSN 1876-6102. doi: 10.1016/j.egypro.2012.06.113.
- J. Bartl, F. Mühle, J. Schottler, L. Sætran, J. Peinke, M. Adaramola, and M. Holling. Wind tunnel experiments on wind turbine wakes in yaw: effects of inflow turbulence and shear. *329-343*, June 2018. ISSN 2366-7443. doi: 10.5194/wes-3-329-2018.
- M. Bastankhah and F. Porté-Agel. Experimental and theoretical study of wind turbine wakes in yawed conditions. *Journal of Fluid Mechanics*, 806:

- 506–541, Nov. 2016. ISSN 0022-1120, 1469-7645. doi: 10.1017/jfm.2016.595.
- M. Bastankhah and F. Porté-Agel. A New Miniature Wind Turbine for Wind Tunnel Experiments. Part I: Design and Performance. *Energies*, 10(7):908, July 2017. doi: 10.3390/en10070908.
- C. Beller. *Urban Wind Energy*. Danmarks Tekniske Universitet, Risø Nationallaboratoriet for Bæredygtig Energi, Dec. 2011. ISBN 978-87-550-3953-7.
- L. H. Benedict, H. Nobach, and C. Tropea. Estimation of turbulent velocity spectra from laser Doppler data. *Measurement Science and Technology*, 11(8):1089–1104, July 2000. ISSN 0957-0233. doi: 10.1088/0957-0233/11/8/301.
- T. Bertényi, C. Wickins, and S. McIntosh. Enhanced Energy Capture Through Gust-Tracking in the Urban Wind Environment. In *48th AIAA Aerospace Sciences Meeting Including the New Horizons Forum and Aerospace Exposition*. American Institute of Aeronautics and Astronautics, June 2012. doi: 10.2514/6.2010-1376.
- M. F. Blair. Influence of Free-Stream Turbulence on Turbulent Boundary Layer Heat Transfer and Mean Profile Development, Part II—Analysis of Results. *Journal of Heat Transfer*, 105(1):41–47, Feb. 1983a. ISSN 0022-1481. doi: 10.1115/1.3245557.
- M. F. Blair. Influence of Free-Stream Turbulence on Turbulent Boundary Layer Heat Transfer and Mean Profile Development, Part I—Experimental Data. *Journal of Heat Transfer*, 105(1):33–40, Feb. 1983b. ISSN 0022-1481. doi: 10.1115/1.3245555.
- M. Borg, A. Shires, and M. Collu. Offshore floating vertical axis wind turbines, dynamics modelling state of the art. part I: Aerodynamics. *Renewable and Sustainable Energy Reviews*, 39:1214–1225, Nov. 2014. ISSN 1364-0321. doi: 10.1016/j.rser.2014.07.096.
- C. L. Bottasso, F. Campagnolo, and V. Petrović. Wind tunnel testing of scaled wind turbine models: Beyond aerodynamics. *Journal of Wind Engineering and Industrial Aerodynamics*, 127:11–28, Apr. 2014. ISSN 0167-6105. doi: 10.1016/j.jweia.2014.01.009.
- L. Boyer and G. Searby. Random sampling: Distortion and reconstruction of velocity spectra from fast Fourier-transform analysis of the analog signal

- of a laser Doppler processor. *Journal of Applied Physics*, 60(8):2699–2707, Oct. 1986. ISSN 0021-8979. doi: 10.1063/1.337098.
- H. Bredmose, F. Lemmer, M. Borg, A. Pegalajar-Jurado, R. F. Mikkelsen, T. S. Larsen, T. Fjelstrup, W. Yu, A. K. Lomholt, L. Boehm, and J. A. Armendariz. The Triple Spar campaign: Model tests of a 10MW floating wind turbine with waves, wind and pitch control. *Energy Procedia*, 137: 58–76, Oct. 2017. ISSN 1876-6102. doi: 10.1016/j.egypro.2017.10.334.
- R. B. Cal, J. Lebrón, L. Castillo, H. S. Kang, and C. Meneveau. Experimental study of the horizontally averaged flow structure in a model wind-turbine array boundary layer. *Journal of Renewable and Sustainable Energy*, 2(1):013106, Jan. 2010. doi: 10.1063/1.3289735.
- N. Campbell, S. Stankovic, M. Graham, P. Parkin, M. van Duijvendijk, T. de Gruiter, S. Behling, J. Hieber, and M. Blanch. Wind energy for the built environment (Project Web). *A report for Joule III Contract No JOR3-CT98-01270*, 2001.
- I. P. Castro. Effects of Free Stream Turbulence on Low Reynolds Number Boundary Layers. *Journal of Fluids Engineering*, 106(3):298–306, Sept. 1984. ISSN 0098-2202. doi: 10.1115/1.3243119.
- I. P. Castro and A. G. Robins. The flow around a surface-mounted cube in uniform and turbulent streams. *Journal of Fluid Mechanics*, 79(2):307–335, Feb. 1977. ISSN 1469-7645, 0022-1120. doi: 10.1017/S0022112077000172.
- R.-D. Chang, J. Zuo, Z.-Y. Zhao, G. Zillante, X.-L. Gan, and V. Soebarto. Evolving theories of sustainability and firms: History, future directions and implications for renewable energy research. *Renewable and Sustainable Energy Reviews*, 72:48–56, May 2017. ISSN 1364-0321. doi: 10.1016/j.rser.2017.01.029.
- K. A. Chauhan, P. A. Monkewitz, and H. M. Nagib. Criteria for assessing experiments in zero pressure gradient boundary layers. *Fluid Dynamics Research*, 41(2):021404, Mar. 2009. ISSN 1873-7005. doi: 10.1088/0169-5983/41/2/021404.
- A. Choukulkar, Y. Pichugina, C. T. M. Clack, R. Calhoun, R. Banta, A. Brewer, and M. Hardesty. A new formulation for rotor equivalent wind speed for wind resource assessment and wind power forecasting. *Wind Energy*, 19(8):1439–1452, 2016. ISSN 1099-1824. doi: 10.1002/we.1929.

- F. H. Clauser. The Turbulent Boundary Layer. In *Advances in Applied Mechanics*, volume 4, pages 1–51. Elsevier, Jan. 1956. doi: 10.1016/S0065-2156(08)70370-3.
- J. J. Cohen, J. Reichl, and M. Schmidthaler. Re-focussing research efforts on the public acceptance of energy infrastructure: A critical review. *Energy*, 76:4–9, Nov. 2014. ISSN 0360-5442. doi: 10.1016/j.energy.2013.12.056.
- D. Coles. The law of the wake in the turbulent boundary layer. *Journal of Fluid Mechanics*, 1(2):191–226, July 1956. ISSN 1469-7645, 0022-1120. doi: 10.1017/S0022112056000135.
- G. Comte-Bellot and S. Corrsin. The use of a contraction to improve the isotropy of grid-generated turbulence. *Journal of Fluid Mechanics*, 25(4):657–682, Aug. 1966. ISSN 1469-7645, 0022-1120. doi: 10.1017/S0022112066000338.
- J. O. Dabiri. Potential order-of-magnitude enhancement of wind farm power density via counter-rotating vertical-axis wind turbine arrays. *Journal of Renewable and Sustainable Energy*, 3(4):043104, July 2011. doi: 10.1063/1.3608170.
- L. A. Danao, O. Eboibi, and R. Howell. An experimental investigation into the influence of unsteady wind on the performance of a vertical axis wind turbine. *Applied Energy*, 107:403–411, July 2013. ISSN 0306-2619. doi: 10.1016/j.apenergy.2013.02.012.
- A. S. Dar, G. A. Barcos, and F. Porté-Agel. An experimental investigation of a roof-mounted horizontal-axis wind turbine in an idealized urban environment. *Renewable Energy*, May 2022. ISSN 0960-1481. doi: 10.1016/j.renene.2022.05.035.
- P. A. Davidson. *Turbulence: An Introduction for Scientists and Engineers*. Oxford University Press, 2015. ISBN 978-0-19-872258-8.
- E. Dayan. Wind energy in buildings: Power generation from wind in the urban environment - where it is needed most. *Refocus*, 7(2):33–38, Mar. 2006. ISSN 1471-0846. doi: 10.1016/S1471-0846(06)70545-5.
- D. De Tavernier, C. Ferreira, and A. Goude. Vertical-Axis Wind Turbine Aerodynamics. In *Handbook of Wind Energy Aerodynamics*, pages 1–45. Springer International Publishing, Cham, February 2020. ISBN 978-3-030-05455-7. doi: 10.1007/978-3-030-05455-7_64-2.

- E. Dogan, R. E. Hanson, and B. Ganapathisubramani. Interactions of large-scale free-stream turbulence with turbulent boundary layers. *Journal of Fluid Mechanics*, 802:79–107, Sept. 2016. ISSN 0022-1120, 1469-7645. doi: 10.1017/jfm.2016.435.
- E. Dogan, R. J. Hearst, and B. Ganapathisubramani. Modelling high Reynolds number wall–turbulence interactions in laboratory experiments using large-scale free-stream turbulence. *Philosophical Transactions of the Royal Society A: Mathematical, Physical and Engineering Sciences*, 375 (2089):20160091, Mar. 2017. doi: 10.1098/rsta.2016.0091.
- E. Dogan, R. J. Hearst, R. E. Hanson, and B. Ganapathisubramani. Spatial characteristics of a zero-pressure-gradient turbulent boundary layer in the presence of free-stream turbulence. *Physical Review Fluids*, 4(8):084601, Aug. 2019. doi: 10.1103/PhysRevFluids.4.084601.
- K. Duraisamy, G. Iaccarino, and H. Xiao. Turbulence Modeling in the Age of Data. *Annual Review of Fluid Mechanics*, 51(1):357–377, September 2019. doi: 10.1146/annurev-fluid-010518-040547.
- EcoPlanetEnergy. Case study 2 | EcoPlanet Energy, 2011. URL <http://ecoplanetenergy.com/all-about-eco-energy/inspired-leaders/case-study-2/>. Accessed August 2021.
- F. R. Eldridge. *Wind machines: report*, volume 75. 1975. ISBN 0442261349.
- D. L. Elliott and J. B. Cadogan. Effects of wind shear and turbulence on wind turbine power curves. Technical Report PNL-SA-18354; CONF-900989-2, Pacific Northwest Lab., Richland, WA (USA), Sept. 1990.
- Ö. Ertunç, N. Özyilmaz, H. Lienhart, F. Durst, and K. Beronov. Homogeneity of turbulence generated by static-grid structures. *Journal of Fluid Mechanics*, 654:473–500, July 2010. ISSN 1469-7645, 0022-1120. doi: 10.1017/S0022112010000479.
- L. B. Esteban, E. Dogan, E. Rodríguez-López, and B. Ganapathisubramani. Skin-friction measurements in a turbulent boundary layer under the influence of free-stream turbulence. *Experiments in Fluids*, 58(9):115, Aug. 2017. ISSN 1432-1114. doi: 10.1007/s00348-017-2397-8.
- M. A. Ferreira and B. Ganapathisubramani. Scale interactions in velocity and pressure within a turbulent boundary layer developing over a staggered-cube array. *Journal of Fluid Mechanics*, 910, March 2021. ISSN 0022-1120, 1469-7645. doi: 10.1017/jfm.2020.999.

-
- C. Firouzi and A. Firouzi. *Iran: Eclat et splendeur de la Perse*. Georges Naef, Geneva, 2005. ISBN 978-2-8313-0391-8.
- P. D. Fleming and S. D. Probert. The evolution of wind-turbines: An historical review. *Applied Energy*, 18(3):163–177, Jan. 1984. ISSN 0306-2619. doi: 10.1016/0306-2619(84)90007-2.
- S. Gambuzza and B. Ganapathisubramani. The effects of free-stream turbulence on the performance of a model wind turbine. *Journal of Renewable and Sustainable Energy*, 13(2):023304, Mar. 2021. doi: 10.1063/5.0039168.
- M. Ge, D. F. Gayme, and C. Meneveau. Large-eddy simulation of wind turbines immersed in the wake of a cube-shaped building. *Renewable Energy*, 163:1063–1077, January 2021. ISSN 0960-1481. doi: 10.1016/j.renene.2020.08.156.
- M. Haase and E. Löfström. *Building augmented wind turbines - BAWT : Integrated solutions and technologies of small wind turbines*. SINTEF Academic Press, 2015. ISBN 978-82-536-1493-9.
- P. E. Hancock and P. Bradshaw. The effect of free-stream turbulence on turbulent boundary layers. *Journal of Fluids Engineering*, 105(3):284–289, September 1983. doi: 10.1115/1.3240989.
- P. E. Hancock and P. Bradshaw. Turbulence structure of a boundary layer beneath a turbulent free stream. *Journal of Fluid Mechanics*, 205:45–76, Aug. 1989. ISSN 1469-7645, 0022-1120. doi: 10.1017/S0022112089001941.
- B. Hand and A. Cashman. A review on the historical development of the lift-type vertical axis wind turbine: From onshore to offshore floating application. *Sustainable Energy Technologies and Assessments*, 38:100646, Apr. 2020. ISSN 2213-1388. doi: 10.1016/j.seta.2020.100646.
- R. J. Hearst and B. Ganapathisubramani. Tailoring incoming shear and turbulence profiles for lab-scale wind turbines. *Wind Energy*, 20(12): 2021–2035, August 2017. ISSN 1099-1824. doi: 10.1002/we.2138.
- R. J. Hearst and P. Lavoie. The effect of active grid initial conditions on high Reynolds number turbulence. *Experiments in Fluids*, 56(10):185, September 2015. ISSN 1432-1114. doi: 10.1007/s00348-015-2052-1.
- R. J. Hearst, G. Gomit, and B. Ganapathisubramani. Effect of turbulence on the wake of a wall-mounted cube. *Journal of Fluid Mechanics*, 804:513–530, Oct. 2016. ISSN 0022-1120, 1469-7645. doi: 10.1017/jfm.2016.565.

- R. J. Hearst, E. Dogan, and B. Ganapathisubramani. Robust features of a turbulent boundary layer subjected to high-intensity free-stream turbulence. *Journal of Fluid Mechanics*, 851:416–435, Sept. 2018. ISSN 0022-1120, 1469-7645. doi: 10.1017/jfm.2018.511.
- S. d. J. Helvig, M. K. Vinnes, A. Segalini, N. A. Worth, and R. J. Hearst. A comparison of lab-scale free rotating wind turbines and actuator disks. *Journal of Wind Engineering and Industrial Aerodynamics*, 209:104485, Feb. 2021. ISSN 0167-6105. doi: 10.1016/j.jweia.2020.104485.
- D. Hertwig, S. Grimmond, S. Kotthaus, C. Vanderwel, H. Gough, M. Haefelin, and A. Robins. Variability of physical meteorology in urban areas at different scales: implications for air quality. *Faraday Discussions*, 226(0):149–172, Mar. 2021. ISSN 1364-5498. doi: 10.1039/D0FD00098A.
- A. Hughes and B. Drury. *Electric Motors and Drives, Fundamentals, Types and Application (4th Edition)-Austin Hughes, Bill Drury*. Elsevier Ltd., Oxford, 2013. ISBN 978-0-08-098332-5.
- M. Hultmark and A. J. Smits. Temperature corrections for constant temperature and constant current hot-wire anemometers. *Measurement Science and Technology*, 21(10):105404, Aug. 2010. ISSN 0957-0233. doi: 10.1088/0957-0233/21/10/105404.
- N. Hutchins and I. Marusic. Evidence of very long meandering features in the logarithmic region of turbulent boundary layers. *Journal of Fluid Mechanics*, 579:1–28, May 2007. ISSN 1469-7645, 0022-1120. doi: 10.1017/S0022112006003946.
- IEA. World Energy Outlook 2020 – Analysis, Oct. 2020.
- IEC. IEC 61400-2 Wind turbines—Part 2. Design requirements for small wind turbines, 2013.
- IPCC. *Climate Change 2021: The Physical Science Basis. Contribution of Working Group I to the Sixth Assessment Report of the Intergovernmental Panel on Climate Change*. Cambridge University Press, 2021.
- T. F. Ishugah, Y. Li, R. Z. Wang, and J. K. Kiplagat. Advances in wind energy resource exploitation in urban environment: A review. *Renewable and Sustainable Energy Reviews*, 37:613–626, Sept. 2014. ISSN 1364-0321. doi: 10.1016/j.rser.2014.05.053.

-
- H. S. Kang and C. Meneveau. Direct mechanical torque sensor for model wind turbines. *Measurement Science and Technology*, 21(10):105206, September 2010. doi: 10.1088/0957-0233/21/10/105206.
- A. Karabiber, C. Keles, A. Kaygusuz, and B. B. Alagoz. An approach for the integration of renewable distributed generation in hybrid DC/AC microgrids. *Renewable Energy*, 52:251–259, Apr. 2013. ISSN 0960-1481. doi: 10.1016/j.renene.2012.10.041.
- G. Kavari, M. Tahani, and M. Mirhosseini. Wind shear effect on aerodynamic performance and energy production of horizontal axis wind turbines with developing blade element momentum theory. *Journal of Cleaner Production*, 219:368–376, May 2019. ISSN 0959-6526. doi: 10.1016/j.jclepro.2019.02.073.
- A. KC, J. Whale, and T. Urmee. Urban wind conditions and small wind turbines in the built environment: A review. *Renewable Energy*, 131:268–283, Feb. 2019. ISSN 0960-1481. doi: 10.1016/j.renene.2018.07.050.
- L. V. King. XII. On the convection of heat from small cylinders in a stream of fluid: Determination of the convection constants of small platinum wires with applications to hot-wire anemometry. *Philosophical transactions of the royal society of London. series A, containing papers of a mathematical or physical character*, 214(509-522):373–432, 1914.
- P. Knebel, A. Kittel, and J. Peinke. Atmospheric wind field conditions generated by active grids. *Experiments in Fluids*, 51(2):471–481, Aug. 2011. ISSN 1432-1114. doi: 10.1007/s00348-011-1056-8.
- S. Kooiman and S. Tullis. Response of a Vertical Axis Wind Turbine to Time Varying Wind Conditions Found within the Urban Environment. *Wind Engineering*, 34(4):389–401, June 2010. ISSN 0309-524X. doi: 10.1260/0309-524X.34.4.389.
- M. Kozul, R. J. Hearst, J. P. Monty, B. Ganapathisubramani, and D. Chung. Response of the temporal turbulent boundary layer to decaying free-stream turbulence. *Journal of Fluid Mechanics*, 896, Aug. 2020. ISSN 0022-1120, 1469-7645. doi: 10.1017/jfm.2020.320.
- P.-Å. Krogstad and P. A. Davidson. Is grid turbulence Saffman turbulence? *Journal of Fluid Mechanics*, 642:373–394, Jan. 2010. ISSN 1469-7645, 0022-1120. doi: 10.1017/S0022112009991807.

- P.-Å. Krogstad and P. A. Davidson. Freely decaying, homogeneous turbulence generated by multi-scale grids. *Journal of Fluid Mechanics*, 680:417–434, Aug. 2011. ISSN 1469-7645, 0022-1120. doi: 10.1017/jfm.2011.169.
- P.-Å. Krogstad and P. E. Eriksen. “Blind test” calculations of the performance and wake development for a model wind turbine. *Renewable Energy*, 50:325–333, Feb. 2013. ISSN 0960-1481. doi: 10.1016/j.renene.2012.06.044.
- R. Kumar, K. Raahemifar, and A. S. Fung. A critical review of vertical axis wind turbines for urban applications. *Renewable and Sustainable Energy Reviews*, 89:281–291, June 2018. ISSN 1364-0321. doi: 10.1016/j.rser.2018.03.033.
- J. Kumbertuss, J. Chen, H. X. Yang, and L. Lu. Investigation into the relationship of the overlap ratio and shift angle of double stage three bladed vertical axis wind turbine (VAWT). *Journal of Wind Engineering and Industrial Aerodynamics*, 107-108:57–75, Aug. 2012. ISSN 0167-6105. doi: 10.1016/j.jweia.2012.03.021.
- J. V. Larssen and W. J. Devenport. On the generation of large-scale homogeneous turbulence. *Experiments in Fluids*, 50(5):1207–1223, May 2011. ISSN 1432-1114. doi: 10.1007/s00348-010-0974-1.
- R. Lasseter. Smart distribution: Coupled microgrids. *Proceedings of the IEEE*, 99(6):1074–1082, May 2011. ISSN 0018-9219. doi: 10.1109/JPROC.2011.2114630.
- L. Ledo, P. B. Kosasih, and P. Cooper. Roof mounting site analysis for micro-wind turbines. *Renewable Energy*, 36(5):1379–1391, May 2011. ISSN 0960-1481. doi: 10.1016/j.renene.2010.10.030.
- L. Li. *In the wake of turbulence: A study on the effects of freestream turbulence on the flow around simple and complex geometries*. NTNU, 2022. ISBN 978-82-326-6035-3.
- L. Li, R. J. Hearst, M. A. Ferreira, and B. Ganapathisubramani. The near-field of a lab-scale wind turbine in tailored turbulent shear flows. *Renewable Energy*, 149:735–748, Apr. 2020. ISSN 0960-1481. doi: 10.1016/j.renene.2019.12.049.
- Q. S. Li, L. Zhi, and F. Hu. Boundary layer wind structure from observations on a 325m tower. *Journal of Wind Engineering and Indus-*

- trial Aerodynamics*, 98(12):818–832, Dec. 2010. ISSN 0167-6105. doi: 10.1016/j.jweia.2010.08.001.
- B. Loganathan, I. Mustary, H. Chowdhury, and F. Alam. Effect of Turbulence on a Savonius Type Micro Wind Turbine. *Energy Procedia*, 110: 549–554, Mar. 2017. ISSN 1876-6102. doi: 10.1016/j.egypro.2017.03.183.
- H. Makita. Realization of a large-scale turbulence field in a small wind tunnel. *Fluid Dynamics Research*, 8(1-4):53, Oct. 1991. ISSN 1873-7005. doi: 10.1016/0169-5983(91)90030-M.
- J. F. Manwell, J. G. McGowan, and A. L. Rogers. *Wind Energy Explained: Theory, Design and Application*. John Wiley & Sons, Sept. 2010. ISBN 978-0-470-68628-7.
- R. J. Martinuzzi and B. Havel. Turbulent Flow Around Two Interfering Surface-Mounted Cubic Obstacles in Tandem Arrangement. *Journal of Fluids Engineering*, 122(1):24, 2000. ISSN 00982202. doi: 10.1115/1.483222.
- R. J. Martinuzzi and B. Havel. Vortex shedding from two surface-mounted cubes in tandem. *International Journal of Heat and Fluid Flow*, 25(3): 364–372, June 2004. ISSN 0142-727X. doi: 10.1016/j.ijheatfluidflow.2004.02.003.
- I. Marusic, B. J. McKeon, P. A. Monkewitz, H. M. Nagib, A. J. Smits, and K. R. Sreenivasan. Wall-bounded turbulent flows at high Reynolds numbers: Recent advances and key issues. *Physics of Fluids*, 22(6):065103, June 2010. ISSN 1070-6631. doi: 10.1063/1.3453711.
- I. Marusic, K. A. Chauhan, V. Kulandaivelu, and N. Hutchins. Evolution of zero-pressure-gradient boundary layers from different tripping conditions. *Journal of Fluid Mechanics*, 783:379–411, Nov. 2015. ISSN 0022-1120, 1469-7645. doi: 10.1017/jfm.2015.556.
- D. K. McLaughlin and W. G. Tiederman. Biasing correction for individual realization of laser anemometer measurements in turbulent flows. *The Physics of Fluids*, 16(12):2082–2088, Dec. 1973. ISSN 0031-9171. doi: 10.1063/1.1694269.
- D. Medici and P. H. Alfredsson. Measurements on a wind turbine wake: 3D effects and bluff body vortex shedding. *Wind Energy*, 9(3):219–236, May 2006. ISSN 1099-1824. doi: 10.1002/we.156.

- D. Medici, S. Ivanell, J.-A. Dahlberg, and P. H. Alfredsson. The upstream flow of a wind turbine: blockage effect. *Wind Energy*, 14(5):691–697, January 2011. ISSN 1099-1824. doi: <https://doi.org/10.1002/we.451>.
- S. Mertens. The Energy Yield of Roof Mounted Wind Turbines. *Wind Engineering*, 27(6):507–518, Dec. 2003. ISSN 0309-524X. doi: 10.1260/030952403773617472.
- S. Mertens. *Wind Energy in the Built Environment Concentrator Effects of Buildings*. Multi-Science, 2006. ISBN 0906522 35 8.
- A. Mills, R. Wiser, and K. Porter. The cost of transmission for wind energy in the United States: A review of transmission planning studies. *Renewable and Sustainable Energy Reviews*, 16(1):1–19, Jan. 2012. ISSN 1364-0321. doi: 10.1016/j.rser.2011.07.131.
- J. T. Millward-Hopkins, A. S. Tomlin, L. Ma, D. Ingham, and M. Pourkashanian. The predictability of above roof wind resource in the urban roughness sublayer. *Wind Energy*, 15(2):225–243, March 2012. ISSN 1099-1824. doi: <https://doi.org/10.1002/we.463>.
- M. Molina and P. Enrique Mercado. Modelling and Control Design of Pitch-Controlled Variable Speed Wind Turbines. Apr. 2011. ISBN 978-953-307-221-0. doi: 10.5772/15880.
- L. Mydlarski and Z. Warhaft. On the onset of high-Reynolds-number grid-generated wind tunnel turbulence. *Journal of Fluid Mechanics*, 320:331–368, August 1996. ISSN 1469-7645, 0022-1120. doi: 10.1017/S0022112096007562.
- T. Mücke, D. Kleinhans, and J. Peinke. Atmospheric turbulence and its influence on the alternating loads on wind turbines. *Wind Energy*, 14(2): 301–316, August 2011. ISSN 1099-1824. doi: <https://doi.org/10.1002/we.422>.
- M. Nakajima, S. Iio, and T. Ikeda. Performance of Savonius Rotor for Environmentally Friendly Hydraulic Turbine. *Journal of Fluid Science and Technology*, 3(3):420–429, 2008. ISSN 1880-5558. doi: 10.1299/jfst.3.420.
- I. V. Naumov, R. F. Mikkelsen, V. L. Okulov, and J. N. Sørensen. PIV and LDA measurements of the wake behind a wind turbine model. *Journal of Physics: Conference Series*, 524:012168, June 2014. ISSN 1742-6596. doi: 10.1088/1742-6596/524/1/012168. Publisher: IOP Publishing.

- D. R. Neal, A. Sciacchitano, B. L. Smith, and F. Scarano. Collaborative framework for PIV uncertainty quantification: the experimental database. *Measurement Science and Technology*, 26(7):074003, June 2015. ISSN 0957-0233. doi: 10.1088/0957-0233/26/7/074003.
- A. Neuhauser. Cleanvertec vertical windpower. Technical report, 2016. URL <https://docplayer.org/15572275-Cleanvertec-vertical-windpower-andreas-neuhauser-geschaefsfuehrer.html>. Accessed August 2021.
- I. Neunaber, M. Hölling, R. J. A. M. Stevens, G. Schepers, and J. Peinke. Distinct Turbulent Regions in the Wake of a Wind Turbine and Their Inflow-Dependent Locations: The Creation of a Wake Map. *Energies*, 13(20):5392, Jan. 2020. ISSN 1996-1073. doi: 10.3390/en13205392.
- T. R. Oke. The distinction between canopy and boundary-layer urban heat islands. *Atmosphere*, 14(4):268–277, Dec. 1976. ISSN 0004-6973. doi: 10.1080/00046973.1976.9648422.
- T. R. Oke. The urban energy balance. *Progress in Physical Geography: Earth and Environment*, 12(4):471–508, Dec. 1988. ISSN 0309-1333. doi: 10.1177/030913338801200401.
- D. Oppenheim, C. Owen, and G. White. Outside the square: Integrating wind into urban environments. *Refocus*, 5(3):32–35, May 2004. ISSN 1471-0846. doi: 10.1016/S1471-0846(04)00141-6.
- A. Ouahabi, C. Depollier, L. Simon, and D. Koume. Spectrum estimation from randomly sampled velocity data [LDV]. *IEEE Transactions on Instrumentation and Measurement*, 47(4):1005–1012, Aug. 1998. ISSN 1557-9662. doi: 10.1109/19.744659.
- L. C. Pagnini, M. Burlando, and M. P. Repetto. Experimental power curve of small-size wind turbines in turbulent urban environment. *Applied Energy*, 154:112–121, Sept. 2015. ISSN 0306-2619. doi: 10.1016/j.apenergy.2015.04.117.
- B. R. Pearson, P.-Å. Krogstad, and W. van de Water. Measurements of the turbulent energy dissipation rate. *Physics of Fluids*, 14(3):1288–1290, Mar. 2002. ISSN 1070-6631. doi: 10.1063/1.1445422.
- J. Pitteloud and S. Gsänger. Small Wind World Report. Technical report, 2016. URL <https://distributedwind.org/wp-content/uploads/2016/03/2016-Small-Wind-World-Report.pdf>. Accessed June 2019.

- S. B. Pope. *Turbulent Flows*. Cambridge University Press, Aug. 2000. ISBN 978-0-521-59886-6.
- F. Porté-Agel, M. Bastankhah, and S. Shamsoddin. Wind-Turbine and Wind-Farm Flows: A Review. *Boundary-Layer Meteorology*, 174(1):1–59, Jan. 2020. ISSN 1573-1472. doi: 10.1007/s10546-019-00473-0.
- L. Prandtl. Ueber flüssigkeitsbewegung bei sehr kleiner reibung. *Verhandl. III, Internat. Math.-Kong., Heidelberg, Teubner, Leipzig, 1904*, pages 484–491, 1904.
- M. Raffel, C. E. Willert, F. Scarano, C. J. Kähler, S. T. Wereley, and J. Kompenhans. *Particle Image Velocimetry: A Practical Guide*. Springer, 2018. ISBN 978-3-319-68853-4.
- M. Ragheb. Vertical axis wind turbines. *University of Illinois at Urbana-Champaign*, 1:40, 2011.
- M. R. Raupach, R. A. Antonia, and S. Rajagopalan. Rough-Wall Turbulent Boundary Layers. *Applied Mechanics Reviews*, 44(1):1–25, Jan. 1991. ISSN 0003-6900. doi: 10.1115/1.3119492.
- REN21. Renewables Global Futures Report. Technical report, REN21 Secretariat, Paris, 2017. URL <https://www.ren21.net/2022-renewables-global-futures-report/>.
- REN21. Renewables Global Status Report. Technical report, REN21 Secretariat, Paris, 2022. URL <https://www.ren21.net/reports/global-status-report/>.
- O. Reynolds. XXIX. An experimental investigation of the circumstances which determine whether the motion of water shall be direct or sinuous, and of the law of resistance in parallel channels. *Philosophical Transactions of the Royal Society of London*, 174:935–982, Jan. 1883. doi: 10.1098/rstl.1883.0029.
- A. Rezaeiha, H. Montazeri, and B. Blocken. A framework for preliminary large-scale urban wind energy potential assessment: Roof-mounted wind turbines. *Energy Conversion and Management*, 214:112770, June 2020. ISSN 0196-8904. doi: 10.1016/j.enconman.2020.112770.
- H. Riegler. HAWT versus VAWT: Small VAWTs find a clear niche. *Refocus*, 4(4):44–46, July 2003. ISSN 1471-0846. doi: 10.1016/S1471-0846(03)00433-5.

-
- S. K. Robinson. Coherent Motions in the Turbulent Boundary Layer. *Annual Review of Fluid Mechanics*, 23(1):601–639, January 1991. doi: 10.1146/annurev.fl.23.010191.003125.
- M. Roth. Review of atmospheric turbulence over cities. *Quarterly Journal of the Royal Meteorological Society*, 126(564):941–990, April 2000. ISSN 1477-870X. doi: 10.1002/qj.49712656409.
- R. Saidur, N. A. Rahim, M. R. Islam, and K. H. Solangi. Environmental impact of wind energy. *Renewable and Sustainable Energy Reviews*, 15(5): 2423–2430, June 2011. ISSN 1364-0321. doi: 10.1016/j.rser.2011.02.024.
- A. P. Schaffarczyk. *Introduction to Wind Turbine Aerodynamics*. Green Energy and Technology. Springer, Berlin, Heidelberg, 2014. ISBN 978-3-642-36408-2 978-3-642-36409-9. doi: 10.1007/978-3-642-36409-9.
- F. Scheurich and R. E. Brown. Modelling the aerodynamics of vertical-axis wind turbines in unsteady wind conditions. *Wind Energy*, 16(1):91–107, February 2013. ISSN 1099-1824. doi: <https://doi.org/10.1002/we.532>.
- P. Schlatter and R. Örlü. Assessment of direct numerical simulation data of turbulent boundary layers. *Journal of Fluid Mechanics*, 659: 116–126, Sept. 2010. ISSN 1469-7645, 0022-1120. doi: 10.1017/S0022112010003113.
- J. Schottler, A. Hölling, J. Peinke, and M. Hölling. Design and implementation of a controllable model wind turbine for experimental studies. *Journal of Physics: Conference Series*, 753:072030, Sept. 2016. ISSN 1742-6596. doi: 10.1088/1742-6596/753/7/072030.
- A. Sciacchitano and B. Wieneke. PIV uncertainty propagation. *Measurement Science and Technology*, 27(8):084006, June 2016. ISSN 0957-0233. doi: 10.1088/0957-0233/27/8/084006.
- A. Segalini and J.-Å. Dahlberg. Blockage effects in wind farms. *Wind Energy*, 23(2):120–128, December 2020. ISSN 1099-1824. doi: 10.1002/we.2413.
- B. Shahizare, N. Nik-Ghazali, W. T. Chong, S. Tabatabaeikia, N. Izadyar, and A. Esmaeilzadeh. Novel investigation of the different Omni-direction-guide-vane angles effects on the urban vertical axis wind turbine output power via three-dimensional numerical simulation. *Energy Conversion and Management*, 117:206–217, June 2016. ISSN 0196-8904. doi: 10.1016/j.enconman.2016.03.034.

- N. S. Sharp, S. Neuscamman, and Z. Warhaft. Effects of large-scale free stream turbulence on a turbulent boundary layer. *Physics of Fluids*, 21(9):095105, Sept. 2009. ISSN 1070-6631. doi: 10.1063/1.3225146.
- C. J. Simão Ferreira, G. J. W. van Bussel, and G. A. M. van Kuik. Wind Tunnel Hotwire Measurements, Flow Visualization and Thrust Measurement of a VAWT in Skew. *Journal of Solar Energy Engineering*, 128(4):487–497, Aug. 2006. ISSN 0199-6231. doi: 10.1115/1.2349550.
- J. Smith, T. Forsyth, K. Sinclair, and F. Oteri. Built-Environment Wind Turbine Roadmap. Technical Report NREL/TP-5000-50499, National Renewable Energy Lab. (NREL), Golden, CO (United States), Nov. 2012.
- A. J. Smits and I. Marusic. Wall-bounded turbulence. *Physics Today*, 66(9):25, September 2013. doi: 10.1063/PT.3.2114.
- A. J. Smits, B. J. McKeon, and I. Marusic. High-Reynolds Number Wall Turbulence. *Annual Review of Fluid Mechanics*, 43(1):353–375, 2011. doi: 10.1146/annurev-fluid-122109-160753.
- S. Stankovic, N. Campbell, and A. Harries. *Urban Wind Energy*. Routledge, London, July 2009. ISBN 978-1-84977-026-2. doi: 10.4324/9781849770262.
- T. Stathopoulos, H. Alrawashdeh, A. Al-Quraan, B. Blocken, A. Dilimulati, M. Paraschivoiu, and P. Pilay. Urban wind energy: Some views on potential and challenges. *Journal of Wind Engineering and Industrial Aerodynamics*, 179:146–157, Aug. 2018. ISSN 0167-6105. doi: 10.1016/j.jweia.2018.05.018.
- K. A. Thole and D. G. Bogard. High Freestream Turbulence Effects on Turbulent Boundary Layers. *Journal of Fluids Engineering*, 118(2):276–284, June 1996. ISSN 0098-2202. doi: 10.1115/1.2817374.
- F. Toja-Silva, A. Colmenar-Santos, and M. Castro-Gil. Urban wind energy exploitation systems: Behaviour under multidirectional flow conditions—Opportunities and challenges. *Renewable and Sustainable Energy Reviews*, 24:364–378, Aug. 2013. ISSN 1364-0321. doi: 10.1016/j.rser.2013.03.052.
- F. Toja-Silva, C. Peralta, O. Lopez-Garcia, J. Navarro, and I. Cruz. On Roof Geometry for Urban Wind Energy Exploitation in High-Rise Buildings. *Computation*, 3(2):299–325, June 2015. doi: 10.3390/computation3020299.

- F. Toja-Silva, O. Lopez-Garcia, C. Peralta, J. Navarro, and I. Cruz. An empirical–heuristic optimization of the building-roof geometry for urban wind energy exploitation on high-rise buildings. *Applied Energy*, 164:769–794, Feb. 2016. ISSN 0306-2619. doi: 10.1016/j.apenergy.2015.11.095.
- UNFCCC. The Paris Agreement, 2015.
- P. Veers, K. Dykes, E. Lantz, S. Barth, C. L. Bottasso, O. Carlson, A. Clifton, J. Green, P. Green, H. Holttinen, D. Laird, V. Lehtomäki, J. K. Lundquist, J. Manwell, M. Marquis, C. Meneveau, P. Moriarty, X. Munduate, M. Muskulus, J. Naughton, L. Pao, J. Paquette, J. Peinke, A. Robertson, J. S. Rodrigo, A. M. Sempreviva, J. C. Smith, A. Tuohy, and R. Wisser. Grand challenges in the science of wind energy. *Science*, 366:443, Oct. 2019. ISSN 0036-8075, 1095-9203. doi: 10.1126/science.aau2027.
- P. Vincenti, J. Klewicki, C. Morrill-Winter, C. M. White, and M. Wosnik. Streamwise velocity statistics in turbulent boundary layers that spatially develop to high Reynolds number. *Experiments in Fluids*, 54(12):1629, Nov. 2013. ISSN 1432-1114. doi: 10.1007/s00348-013-1629-9.
- G. Vita, A. Šarkić Glumac, H. Hemida, S. Salvadori, and C. Baniotopoulos. On the Wind Energy Resource above High-Rise Buildings. *Energies*, 13(14):3641, July 2020. doi: 10.3390/en13143641.
- R. Wagner, I. Antoniou, S. M. Pedersen, M. S. Courtney, and H. E. Jørgensen. The influence of the wind speed profile on wind turbine performance measurements. *Wind Energy*, 12(4):348–362, September 2009. ISSN 1099-1824. doi: 10.1002/we.297.
- S. Wagner, R. Bareiß, and G. Guidati. Noise Mechanisms of Wind Turbines. In *Wind Turbine Noise*, pages 67–92. Springer, Berlin, Heidelberg, 1996. ISBN 978-3-642-88710-9. doi: 10.1007/978-3-642-88710-9_4.
- L. Wang, D. Li, Z. Gao, T. Sun, X. Guo, and E. Bou-Zeid. Turbulent Transport of Momentum and Scalars Above an Urban Canopy. *Boundary-Layer Meteorology*, 150(3):485–511, Mar. 2014. ISSN 1573-1472. doi: 10.1007/s10546-013-9877-z.
- D. W. Wekesa, C. Wang, Y. Wei, and W. Zhu. Experimental and numerical study of turbulence effect on aerodynamic performance of a small-scale vertical axis wind turbine. *Journal of Wind Engineering and Industrial Aerodynamics*, 157:1–14, Oct. 2016. ISSN 0167-6105. doi: 10.1016/j.jweia.2016.07.018.

- A. J. Wheeler and A. R. Ganji. *Introduction to engineering experimentation*, volume 199. Prentice Hall New Jersey, 1996. ISBN 978-3-7091-1389-9. doi: 10.1007/978-3-7091-1390-5.
- S. Whittlesey, Robert W. caand Liska and J. O. Dabiri. Fish schooling as a basis for vertical axis wind turbine farm design. *Bioinspiration & Biomimetics*, 5(3):035005, Aug. 2010. ISSN 1748-3190. doi: 10.1088/1748-3182/5/3/035005.
- B. Wieneke. PIV uncertainty quantification from correlation statistics. *Measurement Science and Technology*, 26(7):074002, June 2015. ISSN 0957-0233. doi: 10.1088/0957-0233/26/7/074002.
- X. Wu, J. M. Wallace, and J.-P. Hickey. Boundary layer turbulence and freestream turbulence interface, turbulent spot and freestream turbulence interface, laminar boundary layer and freestream turbulence interface. *Physics of Fluids*, 31(4):045104, Apr. 2019. ISSN 1070-6631. doi: 10.1063/1.5093040.
- A. Yakhot, H. Liu, and N. Nikitin. Turbulent flow around a wall-mounted cube: A direct numerical simulation. *International Journal of Heat and Fluid Flow*, 27(6):994–1009, Dec. 2006. ISSN 0142-727X. doi: 10.1016/j.ijheatfluidflow.2006.02.026.
- A.-S. Yang, Y.-M. Su, C.-Y. Wen, Y.-H. Juan, W.-S. Wang, and C.-H. Cheng. Estimation of wind power generation in dense urban area. *Applied Energy*, 171:213–230, June 2016. ISSN 0306-2619. doi: 10.1016/j.apenergy.2016.03.007.
- J. You and T. A. Zaki. Conditional statistics and flow structures in turbulent boundary layers buffeted by free-stream disturbances. *Journal of Fluid Mechanics*, 866:526–566, May 2019. ISSN 0022-1120, 1469-7645. doi: 10.1017/jfm.2019.104.
- S. Zhang, B. Du, M. Ge, and Y. Zuo. Study on the operation of small rooftop wind turbines and its effect on the wind environment in blocks. *Renewable Energy*, 183:708–718, January 2022. ISSN 0960-1481. doi: 10.1016/j.renene.2021.11.059.
- H. Zhou, Y. Lu, X. Liu, R. Chang, and B. Wang. Harvesting wind energy in low-rise residential buildings: Design and optimization of building forms. *Journal of Cleaner Production*, 167:306–316, November 2017. ISSN 0959-6526. doi: 10.1016/j.jclepro.2017.08.166.

Article I

**Spatial development of a turbulent
boundary layer subjected to
freestream turbulence**

Yannick Jooss, Leon Li, Tania Bracchi, R. Jason Hearst

Published in:
Journal of Fluid Mechanics, **911**.

Spatial development of a turbulent boundary layer subjected to freestream turbulence

Yannick Jooss¹, Leon Li¹, Tania Bracchi¹ and R. Jason Hearst^{1,†}

¹Department of Energy and Process Engineering, Norwegian University of Science and Technology, Trondheim NO-7491, Norway

(Received 5 June 2020; revised 18 September 2020; accepted 28 October 2020)

The spatial development of a turbulent boundary layer (TBL) subjected to freestream turbulence (FST) is investigated experimentally in a water channel for friction Reynolds numbers up to $Re_\tau = 5060$. Four different FST intensities are generated with an active grid, ranging from a low-turbulence reference case to $u'_\infty/U_\infty = 12.5\%$. Wall-normal velocity scans are performed with laser doppler velocimetry at three positions downstream of the grid. There are two combating influences as the flow develops: the TBL grows while the FST decays. Whilst previous studies have shown the wake region of the TBL is suppressed by FST, the present measurements demonstrate that the wake recovers sufficiently far downstream. For low levels of FST, the near-wall variance peak grows as one moves downstream, whereas high FST results in an initially high variance peak that decays with streamwise position. These results are mirrored in the evolution of the spectrograms, where low FST results in the emergence of an outer spectral peak as the flow evolves, while high FST sees an initially high outer spectral peak decay in space. This finding is significant as it suggests the FST does not permanently mature the TBL ahead of its natural evolution. Finally, it is explicitly demonstrated that it is not sufficient to characterize the TBL solely by conventional parameters such as Re_τ , but that the level of FST and the evolution of the two flows must also be considered.

Key words: homogeneous turbulence, turbulent boundary layers

1. Introduction

Turbulent boundary layers (TBL) exist in a wide range of natural processes and technical applications. Understanding their nature and evolution has been a subject of great interest since the concept was first introduced (Prandtl 1905). The study of TBLs is also important for developing knowledge on diverse problems ranging from how heat is distributed in the atmosphere to the determination of drag forces on aeroplanes and ships (Smits & Marusic 2013). In many of these flows, the freestream above the boundary layer is also turbulent. The characteristics of the so-called freestream turbulence (FST) can vary significantly; two parameters of leading-order significance are the turbulence intensity u'_∞/U_∞ , where U_∞ is the freestream velocity and u'_∞ is the root-mean-square of the

† Email address for correspondence: jason.hearst@ntnu.no

velocity fluctuations in the freestream, and the size of the largest scales in the flow, both of which vary depending on the turbulence's origin and state of evolution. Over the past three decades the effect of FST on a canonical zero-pressure-gradient turbulent boundary layer has been studied extensively, e.g. Hancock & Bradshaw (1983, 1989), Castro (1984), Thole & Bogard (1996), Sharp, Neuscamman & Warhaft (2009), Dogan, Hanson & Ganapathisubramani (2016), Dogan, Hearst & Ganapathisubramani (2017), Hearst, Dogan & Ganapathisubramani (2018), Dogan *et al.* (2019) and You & Zaki (2019).

Pioneering work in subjecting a turbulent boundary layer to FST was performed by Hancock & Bradshaw (1983, 1989). Freestream turbulence was generated with two different passive grids in a wind tunnel, and the flow was measured over a flat plate. The freestream turbulence intensity and length scales were also varied by measuring at different downstream positions from the grids. This resulted in a range of $2870 \leq Re_\theta \leq 5760$, where $Re_\theta = U_\infty \theta / \nu$ is based on the momentum thickness θ . They covered a range of freestream turbulence length scales $L_{u,\infty}$, representing the characteristic length scale of the energy containing eddies, between 0.67 and 2.23 times the boundary layer thickness δ . They found both u'_∞ / U_∞ and $L_{u,\infty}$ were significant influencing parameters on the structure of the boundary layer. They combined these concepts in an empirical parameter, $\beta = (u'_\infty / U_\infty) / (L_{u,\infty} / \delta + 2)$, which appeared to correlate well with the wall shear stress and boundary layer wake region in their flows. However, their experiment was not without limitations – for example, the relatively low turbulence intensities, up to a maximum of 5.8%, and, more importantly, measurement positions as close as 15 mesh lengths (M) downstream of their grids where the flow is typically still inhomogeneous (Ertuğ *et al.* 2010; Isaza, Salazar & Warhaft 2014). The measurement position relative to the grid bars could bias the results in this region, and more recent measurements offer words of caution and update these results (Hearst *et al.* 2018; Kozul *et al.* 2020). Several other fluids problems, including flow over aerofoils, for example, have shown sensitivity to being in the inhomogeneous region behind a grid, resulting in strongly contrasting results (Devinant, Laverne & Hureau 2002; Wang *et al.* 2014; Maldonado *et al.* 2015). Castro (1984) looked at the effect of freestream turbulence on turbulent boundary layers at relatively low Reynolds numbers, $500 \leq Re_\theta \leq 2500$. Two passive grids were used to create the FST with turbulence intensities up to 7%. It was shown that the skin friction was influenced by both the Reynolds number and the freestream turbulence intensity. Once again measurements were, in part, taken relatively close to the grid, starting from $x/M = 6$.

Similarly, Blair (1983*b*) showed that the skin friction increases with FST in a turbulent boundary layer for $1000 \leq Re_\theta \leq 7000$. In the second part of his work (Blair 1983*a*), the influence of FST on the shape of the turbulent boundary layer profile was analysed. While the logarithmic region was relatively unaffected by the freestream turbulence, the presence of the wake was found to be strongly dependent on the level of FST. The outer region intermittency was progressively suppressed with increasing turbulence intensity, effectively making the wake region of the boundary layer profile imperceptible for $u'_\infty / U_\infty \gtrsim 5.3\%$.

A different way to introduce FST was examined by Thole & Bogard (1996). Crossflow jets were used to generate turbulence intensities up to 20% in the freestream. The conclusions remained the same with the wake being suppressed while the logarithmic region was maintained. This demonstrated that it is not pivotal how the FST is generated.

In a study of canonical turbulent boundary layers without FST, Hutchins & Marusic (2007) introduced the use of spectrograms in boundary layer research. Pre-multiplied spectra at different wall-normal positions throughout the boundary layer are plotted in a contour map illustrating the energy distribution between different wavelengths in the

boundary layer from the wall up to the freestream. They covered a range of friction Reynolds numbers $1010 \leq Re_\tau \leq 7300$, with $Re_\tau = U_\tau \delta / \nu$ based on the friction velocity U_τ . Two peaks were found in the spectrograms: one coinciding with the location of the variance peak close to the wall, which was present through the full range of Re_τ examined, and an outer peak emerging with increasing Re_τ , distinctly visible at $Re_\tau = 7300$. Sharp *et al.* (2009) were the first to use an active grid to study the influence of FST on turbulent boundary layers. The active grid was modeled after the original design of Makita (1991). With the active grid, FST intensities up to 10.5 % were produced. This corresponded to a turbulence Reynolds number of $Re_\lambda = 550$, with $Re_\lambda = u'_\infty \lambda_\infty / \nu$ based on the Taylor microscale λ_∞ . The examined boundary layers ($550 \leq Re_\theta \leq 2840$) showed a decrease of the wake strength with increasing FST, consistent with Blair (1983a). Analysing the pre-multiplied energy spectra showed the emergence of an outer spectral peak similar to the findings of Hutchins & Marusic (2007) at considerably lower Re_τ . This result was confirmed by Dogan *et al.* (2016) who also showed that the magnitude of the outer spectral peak scales with FST. In that work, turbulence intensities up to 13 % were generated with an active grid, and it was shown that the streamwise velocity fluctuations at the near-wall peak in the boundary layer correlate with freestream turbulence intensity. These observations in combination with the presented energy spectra demonstrate that the FST penetrates the boundary layer down to the wall. Despite the permeance of the FST, Dogan *et al.* (2017) used the same setup to demonstrate that the near-wall region is statistically similar to a canonical high- Re_τ turbulent boundary layer without FST.

Using the same setup, Esteban *et al.* (2017) confirmed the increase of skin friction with growing FST (Blair 1983a; Castro 1984). Oil-film interferometry was used to obtain the wall shear stress. It was also found that the relation between Reynolds number and skin friction is similar to canonical turbulent boundary layers without FST. Furthermore, it was demonstrated that oil-film interferometry and the multi-point composite fitting technique of Rodríguez-López, Bruce & Buxton (2015) were in good agreement in their estimates of U_τ for these TBL flows with FST above them.

In a subsequent study by Hearst *et al.* (2018), it was shown that for $8.2\% \leq u'_\infty / U_\infty \leq 12.3\%$, corresponding to $455 \leq Re_\lambda \leq 615$ and up to 65 % changes in the integral scale for a fixed u'_∞ / U_∞ , there was no influence of the length scale on the features of the boundary layer. It was proposed that this result differed from the older Hancock & Bradshaw (1989) result because of the increase in turbulence intensity, a different way of measuring the integral scale and measurements performed at positions more suitably distant from the grid. Through spectral analysis it was found that only the large scales penetrate the boundary layer, resulting in the outer spectral peak which would otherwise not be present in these flows, while the inner spectral peak remained unaffected. This result was included in the formulation of the law of the wall for such flows by Ganapathisubramani (2018). Finally, Hearst *et al.* (2018) developed a model that reproduced the spectrogram of the boundary layer based on the pre-multiplied energy spectrum of the freestream.

The majority of the aforementioned studies focussed on statistics and spectra at singular points in the TBL and did not investigate the streamwise development of the boundary layer. Earlier studies were in fact almost exclusively single plane measurements, and if the streamwise position was varied, this typically involved moving closer to the grid to obtain higher turbulence intensities. The spatial evolution of a canonical turbulent boundary layer without FST was studied experimentally by Vincenti *et al.* (2013) and Marusic *et al.* (2015). They showed that the magnitude of the near wall variance peak increases as the boundary layer evolves spatially. Furthermore, it was demonstrated that the emergence of an outer spectral peak with increasing Re_τ can also be observed in a spatially evolving turbulent boundary layer. There has also been some effort to simulate spatially developing

canonical turbulent boundary layers (Ferrante & Elghobashi 2004; Wu & Moin 2009; Eitel-Amor, Örlü & Schlatter 2014; Wu *et al.* 2017).

None of the aforementioned works investigated how a turbulent boundary layer evolves when subjected to FST which itself is also evolving. Raushan, Singh & Debnath (2018) examined a flow of this type, posing the inverse question: how does the spatial development of a boundary layer influence grid generated freestream turbulence. They used three different passive grids in an open water channel to create different levels of freestream turbulence. The focus in their analysis was on the development of inhomogeneous turbulence in the near-field region of the grids. You & Zaki (2019) compared a turbulent boundary layer subjected to FST (inflow $u'_\infty/U_\infty = 10\%$) to a canonical TBL in a direct numerical simulation (DNS). At $1900 \leq Re_\theta \leq 3000$, an increase of the skin-friction of up to 15% was observed in the presence of FST, as well as the suppression of the wake region, confirming previous experimental results. This study also affirmed an increase in magnitude of the near-wall streamwise variance peak with the logarithmic region remaining robust. At their highest $Re_\theta = 3000$, they also observed the emergence of an outer peak in the pre-multiplied energy spectrogram. Wu, Wallace & Hickey (2019) examined the interfaces between freestream turbulence and laminar and turbulent boundary layers, as well as turbulent spots in a DNS, for $80 \leq Re_\theta \leq 3000$. Recently, Kozul *et al.* (2020) explored the evolution of a temporal turbulent boundary layer subjected to decaying FST. In their DNS study, they analysed the relative timescales of boundary layers and freestream turbulence to determine if and how much the boundary layer is affected. These were insightful works, but the achievable Reynolds numbers in DNS studies are still relatively low compared to what can be realized in a laboratory. So far the development of a turbulent boundary layer subjected to freestream turbulence has only been studied for low Reynolds numbers (Re_τ, Re_θ) and in single cases without comparison to other FST parameters. This study addresses this gap by examining the development of a turbulent boundary layer for $Re_\tau > 5000$ and $Re_\theta > 9000$ at three states of evolution for four levels of freestream turbulence. The influence of the evolving freestream turbulence on the mean velocity and variance profiles is examined, as well as the spectral distribution of energy in the developing boundary layer.

2. Experimental methods and procedure

The measurements were conducted in the water channel at the Norwegian University of Science and Technology. A schematic of the facility is provided in [figure 1](#). The test section measures $11\text{ m} \times 1.8\text{ m} \times 1\text{ m}$ (length \times width \times height) with a maximum water depth of 0.8 m. It is a recirculating, free surface, water channel with a 4 : 1 contraction followed by an active grid upstream of the test section. A 10 mm thick acrylic plate measuring $1.8\text{ m} \times 1.045\text{ m}$ was placed at the start of the test section, immediately downstream of the active grid, on the water surface to dampen surface waves directly caused by the water flowing through the bars of the active grid; the remaining $\sim 10\text{ m}$ of the water channel has a free surface. More details on the facility can be found in [appendix A](#).

The active grid used in this study to generate the freestream turbulence is based on the design of Makita (1991). It is a biplanar grid with 28 rods – 10 horizontal and 18 vertical ([figure 2](#)). The rods are equipped with square-shaped wings that measure 100 mm on the diagonal and include two holes to reduce the motor loading, as well as to prevent 100% blockage from occurring. Each rod can be controlled independently with a stepper motor. The mesh length of the grid, i.e. the spacing between each rod, is $M = 100\text{ mm}$. More information on the active grid design is provided in [appendix B](#).

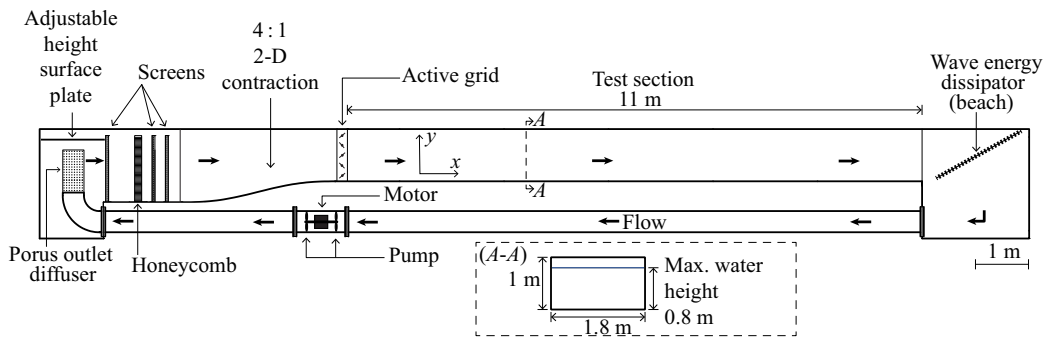


FIGURE 1. Schematic of the water channel facility in Strømmingslaben at the Norwegian University of Science and Technology.

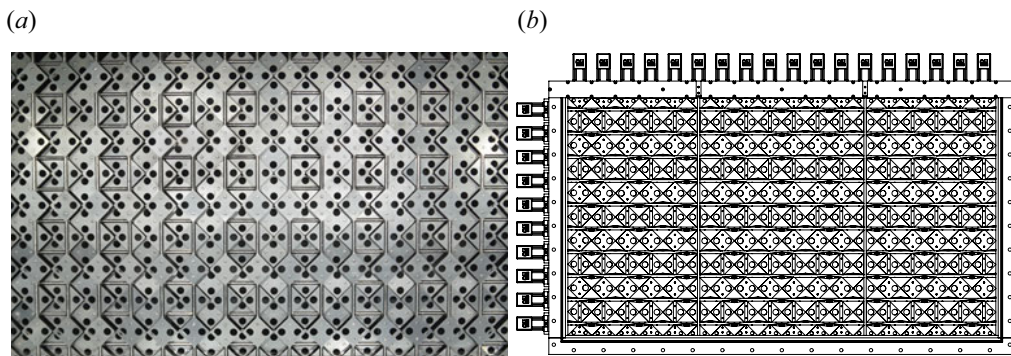


FIGURE 2. Biplanar active grid featuring square wings with holes. Viewed from the test section at full blockage and full schematic of the active grid.

The boundary layer was tripped by the bars of the active grid and then allowed to develop along the glass floor of the water channel. Wall-normal boundary layer scans were performed in the centre of the channel at three streamwise positions, $x/M = 35, 55,$ and 95 . The downstream positions relative to the grid were chosen to be greater than $30M$ to be in keeping with grid turbulence norms for homogeneity and isotropy of the freestream at all measurement positions (Ertunç *et al.* 2010; Isaza *et al.* 2014; Hearst & Lavoie 2015). Velocity measurements were performed with single-component laser doppler velocimetry (LDV). The laser has a wavelength of $514.5 \mu\text{m}$. A 60 mm FiberFlow probe from Dantec Dynamics was used in backscatter mode in combination with a beam expander and a lens with a focal length of 500 mm. This results in an elliptical measuring volume with dimensions $dx \times dy \times dz = 119 \mu\text{m} \times 119 \mu\text{m} \times 1590 \mu\text{m}$, which corresponds to 1.6–1.8 wall units y^+ in the wall-normal direction (depending on the case) and a fringe spacing of $3.33 \mu\text{m}$. Wall unit normalization of the wall-normal position is $y^+ = yU_\tau/\nu$. The wall was found by manually positioning the measurement volume near the wall and then traversing downward in 0.1 mm steps until the data rate suddenly increased, indicating reflections by the glass floor. This gives an accuracy of ~ 0.05 mm. The probe was then traversed upward from this position to the water surface applying a logarithmic spacing with a total of 24 measurement points for each scan. A method to correct for the true wall-normal position from the mean velocity profile, introduced by Rodríguez-López *et al.* (2015), was applied *a posteriori*.

The sampling rate of LDV is non-constant and varies with mean velocity – thus, in this study effectively with wall-normal distance. The mean sampling rate varied between 7 Hz directly at the wall and 155 Hz in the freestream. To guarantee convergence throughout the scans, every position was sampled for 10 min. This is between 630 and 1440 boundary layer turn-overs for a single measurement, depending on the test case. This might be low compared to some hot-wire studies, but it is still a substantial amount of data and sampling time with a single scan, pushing the realistic limits for what could be accomplished as a continuous run. Moreover, a 20 min convergence study in the freestream for the most turbulent case showed only a 0.4 % change in the variance compared to 10 min samples, which is smaller than the other measurement uncertainties. Time-series acquired with LDV also have a non-uniform time step distribution. To perform spectral analysis it is therefore required to resample the data. This is done with sample and hold reconstruction as proposed by Boyer & Searby (1986) and Adrian & Yao (1986). This method returns a uniformly spaced data series, which can then be used to compute spectra using a fast Fourier transform in the same manner as hot-wire data. The spectra are filtered with a bandwidth moving filter of 25 % to facilitate the identification of the underlying trends (Baars, Hutchins & Marusic 2016).

The friction velocity, U_τ , was estimated from the measured velocity profiles using the method introduced by Rodríguez-López *et al.* (2015), which was demonstrated to be effective in these flows by comparison to oil-film interferometry (Esteban *et al.* 2017). This method is essentially a multi-variable optimization applied to the composite boundary layer profile,

$$U^+ = \frac{1}{\kappa} \ln(y^+) + C^+ + \frac{2\Pi}{\kappa} \mathcal{W} \left(\frac{y^+}{Re_\tau} \right), \quad (2.1)$$

where κ is the von Kármán constant, Π is Coles' wake parameter (Coles 1956) and \mathcal{W} is the wake function defined as per Chauhan, Monkewitz & Nagib (2009). Due to a limited number of points acquired in the log-region, a simple comparison of κ to $\kappa = 0.39 \pm 0.02$ as found by Marusic *et al.* (2013) across several facilities was made and found to be in good agreement; this is illustrated explicitly in the subsequent figures. The von Kármán constant is not a specific focus of the present investigation, but the interested reader can find more details on κ in the work by Hearst *et al.* (2018), who measured several points within the log-region for a TBL subjected to FST.

3. Freestream conditions

Four different inflow conditions were investigated in this work. They are presented in table 1 with their freestream statistics at the three measurement positions. The mean velocity in the freestream was kept constant at $U_\infty = 0.345 \pm 0.015 \text{ m s}^{-1}$ for all test cases. A slight increase in velocity was recorded for the downstream positions. This is expected due to the head loss and growing boundary layer in an open channel flow. Overall the differences in mean velocity are considered negligible here. The parameter of interest that was deliberately varied between cases is the turbulence intensity in the freestream u'_∞/U_∞ . The reference case (REF) was created by orienting all the wings of the active grid in line with the flow, resulting in $2.5 \% \leq u'_\infty/U_\infty \leq 3.2 \%$ at the three measurement positions. It is worth noting that the background turbulence in water channel flows is typically on the order of 2 or 3 %, and thus this particular case quickly sees the flow return to the background state of the water channel. For comparison, the canonical turbulent boundary layer results presented by Laskari *et al.* (2018) were measured in a water channel with $\sim 3 \%$ turbulence intensity in the freestream; thus our REF case is

Case	$\Omega \pm \omega$ (Hz)	x/M	U_∞ (m s ⁻¹)	u'_∞/U_∞ (%)	$Re_{\lambda,\infty}$	$L_{u,\infty}$ (m)	u'_∞/v'_∞	Symbol
REF	—	35	0.33	3.2	59	0.20	1.1	●
		55	0.34	2.9	52	0.24	1.2	●
		95	0.35	2.5	45	0.32	1.2	●
A	1 ± 0.5 (2D)	35	0.34	5.5	176	0.30	1.2	■
		55	0.34	4.7	142	0.37	1.2	■
		95	0.35	3.8	103	0.50	1.2	■
B	1 ± 0.5	35	0.34	7.4	303	0.39	1.2	▲
		55	0.34	6.0	219	0.49	1.2	▲
		95	0.35	5.0	176	0.64	1.2	▲
C	0.1 ± 0.05	35	0.35	12.5	725	0.50	1.2	▶
		55	0.35	9.6	495	0.69	1.1	▶
		95	0.36	7.7	392	0.94	1.2	▶

TABLE 1. Freestream parameters of the examined cases at the different streamwise positions. Note that the colours fade with increasing downstream distance from the grid. These symbols are used in all figures and tables.

equivalent to their canonical case. For case A, the wings on the vertical rods remained static, while the horizontal rods were actuated. For the last two cases, B and C, all rods were actuated. The actuation mode for the cases A–C was always fully random. This means rotational velocity, acceleration and period were varied randomly over a set range (Hearst & Lavoie 2015). The parameter that was varied between cases was the mean rotational velocity Ω , i.e. $\Omega_A, = \Omega_B = 1$ Hz and $\Omega_C = 0.1$ Hz. All three cases were varied with a top-hat distribution $\Omega \pm \omega$ with the limits $\omega = 0.5\Omega$. The exact distributions used for each case are listed in table 1. The period and acceleration were always varied in the same range of 0.5–10 s and 10–100 s⁻², respectively. The parameters were chosen based on the findings of previous active grid studies (Kang, Chester & Meneveau 2003; Larssen & Devenport 2011; Hearst & Lavoie 2015; Hearst *et al.* 2018) and slightly adapted to reflect the requirements of this study. The result is a wide range of turbulence intensities at the first measurement position $x/M = 35$, from 3.2 % for REF up to 12.5 % for case C. The turbulence intensity at the first position will be referred to as the initial turbulence intensity, $u'_0/U_0 = (u'_\infty/U_\infty)_{x/M=35}$.

The decay of the turbulence in the freestream was measured with a finer streamwise discretization. Measurements were taken at 15 positions between $x/M = 15$ and $x/M = 107$ at $y = 500$ mm. This wall-normal position was chosen as it was always outside the boundary layer while also being far away from the free surface. As the turbulence decays with increasing distance from the grid, the spread of turbulence intensity between the cases becomes smaller from $\Delta u'_\infty/U_\infty = 9.3$ % at $x/M = 35$ down to $\Delta u'_\infty/U_\infty = 5.2$ % at the last measurement position, $x/M = 95$. The decay of the turbulence with increasing distance from the grid can be described by a power law (Comte-Bellot & Corrsin 1966; Mohamed & Larue 1990; Lavoie, Djenidi & Antonia 2007; Isaza *et al.* 2014),

$$\frac{u'^2_\infty}{U^2_\infty} = A \left(\frac{x}{M} - \frac{x_0}{M} \right)^{-n}, \tag{3.1}$$

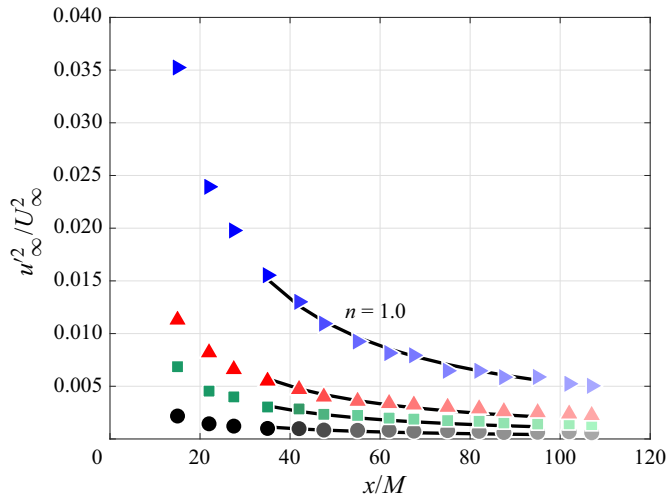


FIGURE 3. Decay of turbulence for case REF ● ; A ■, green; B ▲, red; C ▶, blue with fading colours indicating increasing streamwise distance from the grid.

where x_0 is a virtual origin, and A and n are the decay coefficient and exponent, respectively. Figure 3 shows the best fits to (3.1), resulting in $n \approx 1$ for all cases. Here, all three variables, A , x_0 and n were allowed to vary.

The Taylor microscale in the freestream λ_∞ was calculated as

$$\lambda_\infty^2 = \frac{u'^2}{\langle (\partial u / \partial x)^2 \rangle}, \tag{3.2}$$

assuming local isotropy and Taylor’s frozen flow hypothesis to calculate $(\partial u / \partial x)^2$ from the time series data acquired at a singular streamwise position. A sixth-order central differencing scheme was used to determine the gradients as suggested by Hearst *et al.* (2012). This leads to turbulence Reynolds numbers Re_λ between 45 and 725. A decrease of Re_λ can be observed both for decreasing u'_0 / U_0 and with streamwise evolution of the flow, as expected.

The integral length scale $L_{u,\infty}$ was calculated as proposed by Hancock & Bradshaw (1989) assuming isotropic turbulence,

$$U_\infty \frac{du'_\infty^2}{dx} = \frac{-(u'_\infty^2)^{3/2}}{L_{u,\infty}}, \tag{3.3}$$

where x is the downstream distance from the grid, and the gradient du'_∞^2 / dx is calculated in physical space by taking the analytical derivative of (3.1). An increase in $L_{u,\infty}$ exists as the distance from the grid grows (table 1), which is expected. The integral scale was also computed by other means, e.g. integrating the auto-correlation to the first zero-crossing, but this approach was found to be less robust. Kozul *et al.* (2020, figure 7) demonstrated that while the finite value of the integral scale in flows like the present one is dependent on the method chosen for estimating it, the trends with evolution time (distance) and turbulence intensity are preserved.

The global anisotropy is also reported in table 1 as u'_∞ / v'_∞ . A separate two-component measurement campaign was performed to obtain these estimates. In general, the anisotropy

is between 1.1 and 1.2 and thus similar to what is typically reported in grid turbulence (Lavoie *et al.* 2007) and lower than the anisotropy in some other studies of a similar nature (Sharp *et al.* 2009; Dogan *et al.* 2019). In most cases, the anisotropy grows slightly with downstream distance, which is a result of the slight flow acceleration. Nonetheless, the positional variation in anisotropy is always within $\pm 5\%$, which is approximately the uncertainty of this quantity. The isotropy itself was not a controlled parameter, and generally increasing the turbulence intensity with active grids comes with a loss of isotropy (Hearst & Lavoie 2015). One should thus consider the present results in light of the anisotropy of the flow, which may also have an influence but was not rigorously controlled.

4. Evolution of the mean and variance profiles

Freestream turbulence has previously been shown to influence turbulent boundary layers all the way down to the wall (Castro 1984; Dogan *et al.* 2016; Hearst *et al.* 2018). While the majority of earlier studies focused on the influence of FST at a single point, in the present study we demonstrate that the evolution of the FST also plays a significant role. We begin with the mean statistics. In figure 4 the velocity and variance profiles for the four inflow conditions are displayed together for every measurement position, showing the differences between the cases at distinct downstream positions. It can be observed that the velocity profiles all collapse in the viscous sublayer, the buffer layer and the logarithmic region. In the viscous sublayer they follow the relation $U^+ = y^+$, with U^+ being a function of the streamwise velocity and the friction velocity $U^+ = U/U_\tau$. In the logarithmic region, all profiles agree with the law of the wall. This corresponds to the first three terms in (2.1); the plotted logarithmic region reference line has $\kappa = 0.39$ and $C^+ = 4.35$. The only significant deviation between cases and locations is in the region between the logarithmic layer and the freestream. In a canonical TBL this is the wake region, where large-scale mixing leads to a velocity defect (Coles 1956). When subjected to high enough freestream turbulence intensity, the wake region is known to be suppressed (Blair 1983a; Thole & Bogard 1996; Dogan *et al.* 2016). The freestream, being turbulent itself, leads to a suppression of the intermittent region that typically separates a canonical TBL from an approximately laminar freestream and replaces it with the inherent uniform intermittency of the FST, resulting in a suppressed wake in the boundary layer velocity profile (Dogan *et al.* 2016). The same can be observed here as presented in figure 4. Case REF with the lowest turbulence intensity of $u'_0/U_0 = 3.2\%$ shows traces of a wake region at $x/M = 35$ which grows with the development of the boundary layer; the wake is visible at $x/M = 55$ and 95. This evolution becomes even more apparent when looking at the velocity profiles of a single case at the three streamwise positions plotted together as presented in figure 5; we note that figure 5 does not contain different information from figure 4, but that plotting it in this way is also informative for comparison. DNS data of a fully developed canonical TBL without FST (Sillero, Jiménez & Moser 2013) at a Re_τ comparable to REF is included in figure 5 for reference. The mean velocity profile of REF and the DNS are in good agreement at our last measurement station. The variance profiles are roughly in good agreement, but the background turbulence in the freestream elevates the fluctuations in outer regions of the boundary layer for the experiment. At $x/M = 95$, the intermediate cases, A and B, also exhibit a wake region in the velocity profile (figures 4c, 5b) with turbulence intensities of 3.8% and 5.0%, respectively, but this is still weaker than the REF case and the DNS. For case B, this trend starts to become visible at $x/M = 55$ and $u'_\infty/U_\infty = 4.7\%$. This is remarkably consistent with the limit of $u'_\infty/U_\infty = 5.3\%$ found by Blair (1983a). The present results demonstrate for the first time that even if the wake region is initially suppressed by the FST, it redevelops as the

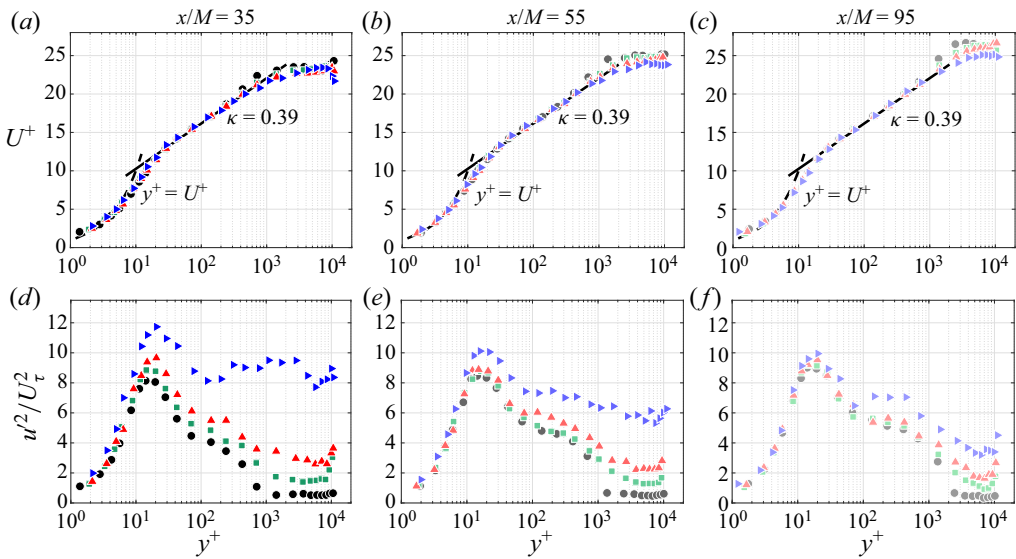


FIGURE 4. Mean velocity and variance profiles for cases REF \bullet ; A \blacksquare , green; B \blacktriangle , red; C \blacktriangleright , blue.

FST decays below a certain threshold. This is also supported by looking at Coles' wake parameter Π (Coles 1956). He predicted it to be 0.55 for a canonical turbulent boundary layer with no FST. Marusic *et al.* (2010) confirmed a similar value in their analysis using the model of Perry, Marusic & Jones (1998). Dogan *et al.* (2016) found $\Pi = 0.55$ in their no-FST case as well and showed that for FST with $7.4\% \leq u'_\infty/U_\infty \leq 12.7\%$ at $x/M = 43$, Coles' wake parameter drops to between -0.52 and -0.26 . At $x/M = 35$, the present study shows values between -0.57 and -0.08 (table 2). For all cases, Π grows with the development of the TBL. The reference case reaches $\Pi = 0.37$, which approaches Coles' prediction. Both cases A and B eventually reach positive values for the wake parameter as the wake starts to become visible as one moves downstream. Case C does not show a visible recovery of the wake, as illustrated in figure 5(c). A visible difference remains compared to the canonical DNS of Sillero *et al.* (2013). The wake parameter for case C grows but remains negative and within the range of values for FST found by Dogan *et al.* (2016) throughout the three positions. u'_∞/U_∞ does not drop below 7.7% within the studied distance from the grid for case C, suggesting it does not drop below the required threshold for wake recovery.

In the present study, we define the boundary layer thickness δ as the point where the velocity reaches 99% of the freestream velocity, $\delta = \delta_{99}$. For all cases an increase of the boundary layer thickness is observed with the streamwise evolution of the TBL as documented in table 2. δ at $x/M = 35$ also scales with u'_∞/U_∞ , likely due to enhanced mixing. It is also worth highlighting that $L_{u,\infty}$ grows with u'_∞/U_∞ at $x/M = 35$. From the first measurement station, the boundary layers with elevated FST (i.e. cases A, B and C) all grow more rapidly than the REF case.

Freestream turbulence is found to increase the friction velocity U_τ at a given point, in agreement with earlier works (Hancock & Bradshaw 1989; Blair 1983a; Castro 1984; Stefes & Fernholz 2004; Dogan *et al.* 2016; Esteban *et al.* 2017). This stems from the FST penetrating the boundary layer, increasing mixing and thus the momentum flux towards the wall. This increases the steepness of the velocity profile close to the wall (Dogan *et al.* 2016) and as a result also the skin friction (Stefes & Fernholz 2004).

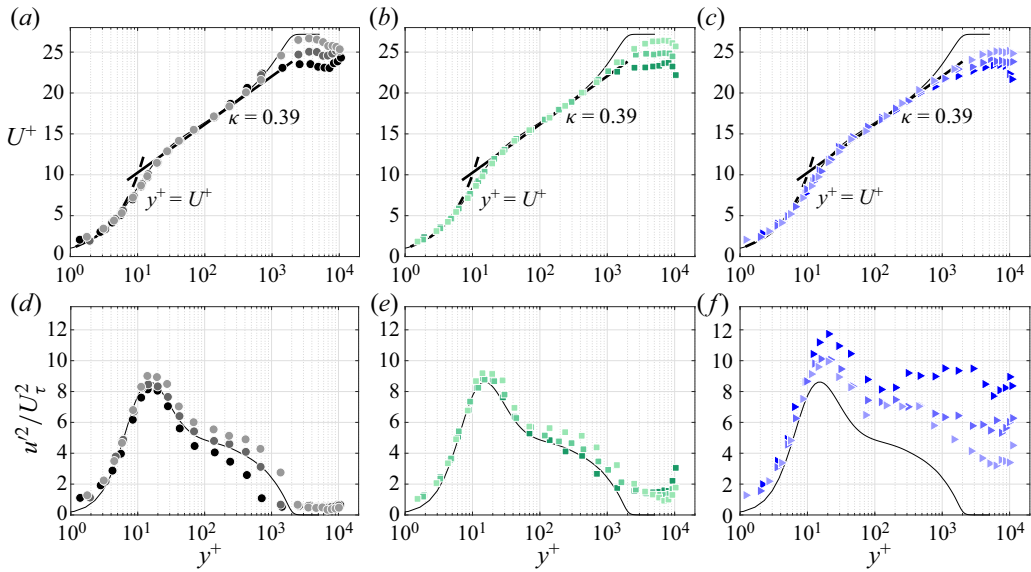


FIGURE 5. Development of mean velocity and variance profiles for cases REF \bullet , A \blacksquare , green and C \blacktriangleright , blue with fading colours indicating increasing streamwise distance from the grid. DNS data of a fully developed canonical TBL at $Re_\tau \approx 1990$ by Sillero *et al.* (2013) plotted as a reference solid black line.

Case	u'_∞/U_∞ (%)	x/M	δ (mm)	δ^* (mm)	θ (mm)	H	U_τ (mm s $^{-1}$)	Re_τ	Re_θ	Π	β	Symbol
REF	3.2	35	85	12	9	1.31	14.0	1210	3080	-0.08	0.73	\bullet
	2.9	55	95	17	12	1.34	13.5	1310	4280	0.04	0.64	\bullet
	2.5	95	138	25	19	1.34	13.1	1870	6860	0.37	0.58	\bullet
A	5.5	35	142	16	13	1.24	14.4	1990	4170	-0.19	1.34	\blacksquare
	4.7	55	170	20	16	1.26	13.8	2490	5860	0.04	1.13	\blacksquare
	3.8	95	265	31	24	1.28	13.3	3700	8990	0.17	0.97	\blacksquare
B	7.4	35	152	15	12	1.23	14.8	2150	3840	-0.35	1.63	\blacktriangle
	6.0	55	220	21	17	1.23	14.0	3260	6230	-0.18	1.41	\blacktriangle
	5.0	95	308	31	25	1.26	13.4	4340	9050	0.01	1.23	\blacktriangle
C	12.5	35	246	22	18	1.18	14.9	3610	6340	-0.57	3.09	\blacktriangleright
	9.6	55	298	23	19	1.21	14.6	4590	7000	-0.35	2.22	\blacktriangleright
	7.7	95	343	29	24	1.22	14.2	5060	8820	-0.26	1.62	\blacktriangleright

TABLE 2. Boundary layer parameters of the test cases at the different streamwise positions.

A decrease in U_τ is observed as the boundary layer develops for each case. This agrees with the behaviour known for spatially evolving canonical turbulent boundary layers without FST (Anderson 2010; Vincenti *et al.* 2013; Marusic *et al.* 2015). Values for the friction Reynolds number Re_τ range from 1210 to 5060 and increase both with freestream turbulence intensity and streamwise development. The same is true for Re_θ , with values between 3080 and 9050. The empirical parameter β defined by Hancock & Bradshaw

(1989) is included in [table 2](#). It follows the same trends as u'_∞/U_∞ , showing that the influence of the FST is dominant in this flow. Greater discussion of this parameter can be found in [appendix C](#).

The variance profiles at the first measurement positions in [figure 4\(d\)](#) resemble results from Dogan *et al.* (2016), Hearst *et al.* (2018) and You & Zaki (2019). They showed that the magnitude of the near-wall peak in the variance profiles correlates with the freestream turbulence intensity. The same can be observed in this study. The higher u'_∞/U_∞ , the stronger the near-wall variance peak. FST penetrates the boundary layer and amplifies the fluctuations close to the wall. Moving downstream we can see that the magnitude of the near-wall peaks approach each other until they approximately collapse at $x/M = 95$ ([figure 4f](#)). Note that the four flows all still have distinct u'_∞/U_∞ , $L_{u,\infty}$ and δ at $x/M = 95$. Thus, the present results demonstrate that if the boundary layer is allowed to evolve for a sufficient time, the correlation between the FST magnitude and the near-wall variance peak magnitude diminishes. This differs from earlier measurements performed at a single downstream position that could not observe this phenomenon. Taking a closer look at the development of the near-wall peak for the cases REF, A and C in [figure 5](#), it becomes apparent that the approach to a common near-wall variance peak magnitude is due to different underlying trends in the four cases. For REF, the near-wall variance peak steadily increases with downstream position. This is in agreement with the results from Marusic *et al.* (2015) for spatially evolving canonical TBLs without FST. This trend is diminished but still present for case A; case B is similar to case A and is not plotted to reduce clutter. For case C, with the highest initial turbulence intensity, the trend reverses: instead of an increase, the near-wall variance peak decreases significantly with the development of the boundary layer. It can be concluded that the spatial development of the near-wall variance peak is strongly dependent on the initial level of turbulence intensity but approaches a common value downstream independently of the initial freestream state, at least for a given Re_τ . Hutchins & Marusic (2007) predicted this to be between 8.4 and 9.2 for the Re_τ examined here. The present measurements find a similar value of $u'^2/U_\tau^2 \approx 9.5$. This is slightly higher than what was found by Hutchins & Marusic (2007), which could be a result of the remaining freestream turbulence still present at the last measurement position, or differences in the noise floors of the measurement techniques used.

The displacement thickness $\delta^* = \int_0^\infty (1 - U(y)/U_\infty) dy$ and momentum thickness $\theta = \int_0^\infty U(y)/U_\infty (1 - U(y)/U_\infty) dy$ grow with streamwise evolution for all cases. The ratio between the two is the shape factor $H = \delta^*/\theta$, which is an indicator of the fullness of the boundary layer profile. Small deviations for the dimensional quantities δ^* and θ can be explained by differences in the mean velocity and uncertainty in the measurements. The trend is still captured accurately. Consequently, in the nondimensional H , the small deviations vanish. This study shows that freestream turbulence reduces the shape factor as the boundary layer profile becomes fuller – i.e. the velocity rises more steeply close to the wall, while farther away from the wall the velocity profile becomes flatter. This is in good agreement with previous studies (Hancock & Bradshaw 1983; Castro 1984; Stefes & Fernholz 2004; Dogan *et al.* 2016; Hearst *et al.* 2018). As presented in [figure 6](#) and [table 2](#), the higher the initial turbulence intensity, the lower the shape factor. For a canonical turbulent boundary layer, Monkewitz, Chauhan & Nagib (2008) found that the shape factor decreases with increasing Re_θ . This is confirmed for each downstream position in this study as depicted in [figure 6](#); the data from Dogan *et al.* (2016) have also been plotted showing the same trend.

The aforementioned trend pertains to a single position. However, the question of how the evolution of H is impacted by the FST is still open. The data of Hancock & Bradshaw (1983) suggest a decrease of the shape factor as one moves downstream; this data is also

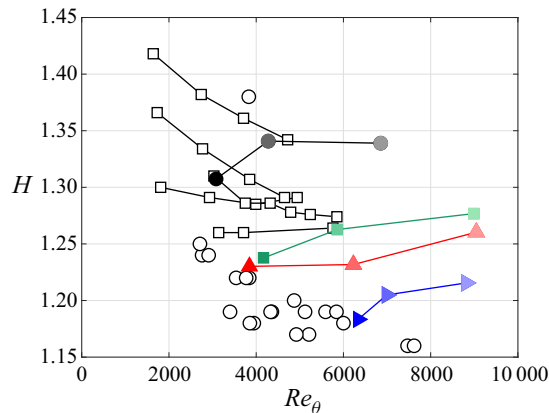


FIGURE 6. Development of the shape factor H for cases REF ●; A ■, green; B ▲, red; C ►, blue with fading colours indicating increasing streamwise distance from the grid. The data of Hancock & Bradshaw (1983) □ and Dogan *et al.* (2016) ○ are also included for reference. Lines connecting points indicate that they were acquired from the same set-up but at different streamwise positions. All Dogan *et al.* (2016) measurements were conducted at the same location but with different freestream conditions.

included in figure 6. It has to be kept in mind that their measurements were for relatively low turbulence intensities, and some of them were very close to the grid. We show that when the turbulence intensity in the freestream is increased further and the measurements are taken past $x/M = 30$, this trend reverses. The shape factor is reduced significantly at the first measurement position, and as the freestream turbulence decreases it recovers towards its natural value. This value can be obtained by looking at the shape factor of canonical zero pressure gradient turbulent boundary layers for a wide range of $Re_{\delta^*} = U_{\infty} \delta^* / \nu$ as presented by Chauhan *et al.* (2009). For Re_{δ^*} between 4000 and 10 000, as found in the present study, a shape factor between 1.35 and 1.41 would be expected without the presence of freestream turbulence (Chauhan *et al.* 2009). While the shape factors of Hancock & Bradshaw (1983) drop away from the canonical values with increasing distance from the grid (Chauhan *et al.* 2009), the data presented herein trend toward the predicted values. The boundary layer appears to forget it started with different conditions as the influence of these conditions diminishes farther downstream.

The continuous streamwise development of the boundary layer results in an increase of Re_{τ} for all cases. At the same time Re_{τ} scales with the level of freestream turbulence which decays with streamwise evolution of the flow. It is therefore interesting to compare boundary layers with similar Re_{τ} but different paths to get there. This is done in figure 7 with the reference case at $x/M = 95$ with $u'_{\infty}/U_{\infty} = 2.5\%$ and $Re_{\tau} = 1870$ and case A at $x/M = 35$ with $u'_{\infty}/U_{\infty} = 5.5\%$ and $Re_{\tau} = 1990$ (figure 7a,c), as well as with case A at $x/M = 95$ with $u'_{\infty}/U_{\infty} = 3.8\%$ and $Re_{\tau} = 3700$ and case C at $x/M = 35$ with $u'_{\infty}/U_{\infty} = 12.5\%$ and $Re_{\tau} = 3610$ (figure 7b,d). For the first comparison (figure 7a,c) with a moderate difference in freestream turbulence intensity, the deviations in the variance profiles are small. Nevertheless, a distinction in the outer region is visible in the velocity profile. Whereas for case A at $x/M = 35$ the wake is still suppressed, for the most part, the reference case at $x/M = 95$ displays a pronounced wake region. This is particularly interesting given these two cases have essentially the same freestream integral scale, $L_{u,\infty} \approx 310$ mm and $2.1 \leq L_{u,\infty}/\delta \leq 2.3$, suggesting that this parameter is not what is driving the difference in the outer region. When comparing cases with a bigger difference

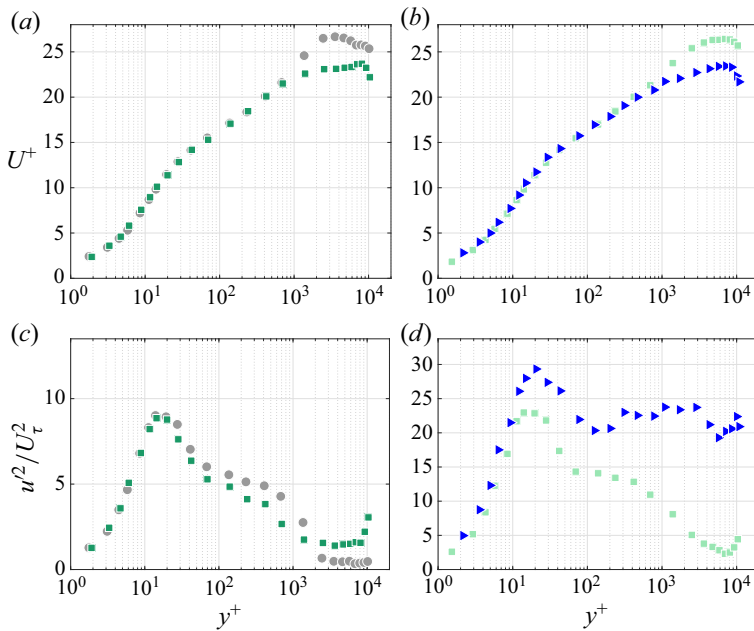


FIGURE 7. Comparison of TBL profiles with similar Re_τ : (a,c) case REF at $x/M = 95$ ●, grey and case A at $x/M = 35$ ■, green; (b,d) case A at $x/M = 95$ ■, light green and case C at $x/M = 35$ ►, blue.

in freestream turbulence (figure 7b,d), the differences become even more distinct. Once again the velocity profiles are collapsed in the viscous sublayer, the buffer layer and the logarithmic region. Farther away from the wall the profiles diverge. For case C the wake region is fully suppressed at this point, whereas case A at $x/M = 95$ shows the reemergence of a wake. In the variance profiles the considerable difference in u'_∞/U_∞ is visible. Moving closer to the wall it becomes evident that the turbulence intensity in the freestream also influences the boundary layer close to the wall. The near-wall variance peak is significantly more pronounced for the case with the higher freestream turbulence intensity. These particular cases have the same $L_{u,\infty}$ and $1.9 \leq L_{u,\infty}/\delta \leq 2.0$, again suggesting the above differences are not a result of a difference in the size of the large scales in the freestream. The same general trends were also observed at $Re_\tau \approx 4500$. One can thus conclude that Re_τ alone is not sufficient to describe the profile of a turbulent boundary layer subjected to FST, but rather u'_∞/U_∞ and the evolution distance must also be considered at a minimum.

5. Evolution of the spectral distribution of energy

Further insight into the processes governing the evolution of a TBL subjected to FST can be gained by looking at the spectral distribution of energy at different streamwise positions. For this, the pre-multiplied spectra, $\phi^+ = k_x \phi_u / U_\tau^2$, at every wall-normal position are plotted together in a contour map illustrating regions and wavelengths, $\zeta^+ = 2\pi U_\tau / k_x \nu$, with high and low energy. This is based on the streamwise energy spectra ϕ_u in normalized wavenumber space k_x . Computing spectra from the LDV measurements is not as straightforward as it is from hot-wires, which is the more common measurement technique in TBLs. As stated in § 2, we have used the sample

and hold technique to compute the spectra and applied a bandwidth moving filter. The spectra are also computed over less boundary layer turn-overs than is typical in hot-wire measurements, despite the long sample times used herein. As such, we provide the present spectra as qualitative relative comparisons in which we have confidence, rather than exact quantitative comparisons to the hot-wire-acquired spectra in the literature.

Hutchins & Marusic (2007) showed that in a canonical turbulent boundary layer there is a fixed peak close to the wall at $y^+ \approx 15$ and $\zeta^+ \approx 1000$. They further showed that for high $Re_\tau = 7300$, an outer spectral peak emerges. The evolution of the spectrograms in a spatially developing TBL for different initial freestream turbulence intensities is presented in figure 8. The first observation is that in agreement with Dogan *et al.* (2016), Hearst *et al.* (2018) and Ganapathisubramani (2018), the location of the near-wall spectral peak is independent of the level of freestream turbulence and coincides with the location found by Hutchins & Marusic (2007). It seems that the small scales close to the wall are not affected by the freestream turbulence. This is displayed explicitly in figure 9, where the larger scales deviate visibly for the higher FST cases above $u'_\infty/U_\infty \approx 6\%$, in agreement with Hearst *et al.* (2018).

Looking at the first measurement position, $x/M = 35$, in figure 8 confirms the findings of Sharp *et al.* (2009), Dogan *et al.* (2016) and Hearst *et al.* (2018) that when subjected to strong enough FST an outer spectral peak forms at considerably lower Reynolds numbers than in canonical TBLs – here at $Re_\tau = 3610$ for case C. For the lowest Re_τ of 1210, corresponding to the reference case at $x/M = 35$, no outer peak exists, and the spectrogram resembles the shape found by Hutchins & Marusic (2007) for $Re_\tau = 1010$. Cases B and C at $x/M = 35$ demonstrate a timid emergence of an outer spectral peak. The novel element of the present study is the streamwise development of these features. For cases REF, A and B, with initial turbulence intensities between 3.2% and 7.4%, the outer spectral peak grows in magnitude and moves away from the wall as the boundary layer develops. Of these three cases, case B with the highest initial turbulence intensity u'_0/U_0 , shows the strongest outer spectral peak. This agrees with the trend for increasing Re_τ detected by Hutchins & Marusic (2007) in a canonical TBL.

Up until the present study there has been no reason not to expect a growth of the outer spectral peak with increasing Re_τ for higher freestream turbulence intensities as well. Instead, case C with the highest initial turbulence intensity of $u'_0/U_0 = 12.5\%$, presents different behaviour. The outer spectral peak is pronounced at $x/M = 35$. In contrast to the expected continuous growth of the outer spectral peak in canonical TBLs, here it gradually decreases as the boundary layer develops and the freestream turbulence decays. Thus, if one did not know the measured values of Re_τ , the spectrogram from earlier in the spatial evolution of case C gives the impression it is at a higher Re_τ than those from farther downstream. In contrast to the lower FST cases, the decay of the freestream turbulence more significantly influences the spectrogram than the growth of the TBL. This fading of the outer spectral peak is visible throughout the three measurement positions for case C. This behavior becomes more evident when looking at the net change $\Delta^+ = (\phi^+ - \phi_0^+)/\phi_{0,max}^+$ in spectrograms, where ϕ_0^+ is the spectrogram at $x/M = 35$. This is displayed in figure 10 for the reference case compared to case C with the highest freestream turbulence intensity. The reference case (figure 10a,b) shows the slow emergence of an outer peak with a positive net change Δ^+ for $\zeta^+ \approx 10^4$ most distinctly in the outer regions of the boundary layer at $y^+ \approx 10^3$. The opposite is observed for case C in figure 10(c,d), with a negative net change where the outer spectral peak was initially most pronounced at $10^3 \lesssim y^+ \lesssim 10^4$ and $10^4 \lesssim \zeta^+ \lesssim 10^5$. The location of the outer spectral peak in outer scaling, i.e. y/δ and ζ/δ , does not coincide with the location for canonical TBLs identified by Hutchins & Marusic (2007). This is to be expected for a TBL subjected to FST (Dogan

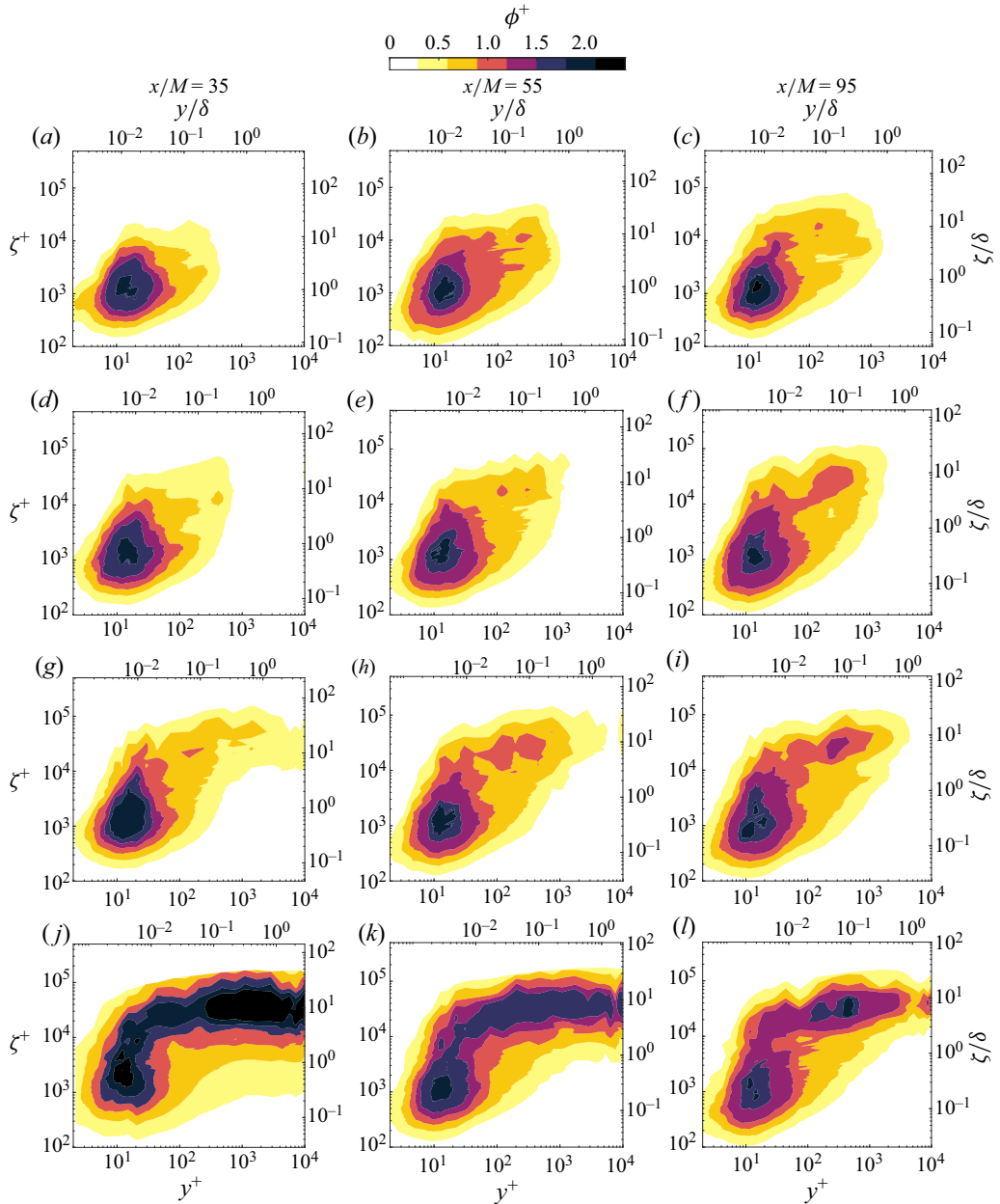


FIGURE 8. Spectrograms for cases REF (*a–c*), A (*d–f*), B (*g–i*) and C (*j–l*) at the three streamwise positions with increasing level of freestream turbulence from top to bottom.

et al. 2016; Hearst *et al.* 2018). The reason for this is that the peak is superimposed onto the outer boundary layer by the freestream turbulence. In fact, the peak is situated much higher for the FST cases and moves only once the boundary layer starts to redistribute the energy. This is documented in great detail for numerous cases in Hearst *et al.* (2018). As the outer peak evolves in this study, it approaches $\zeta_x/\delta \approx 10$ and $y/\delta \approx 0.4$ as found by Hearst *et al.* (2018).

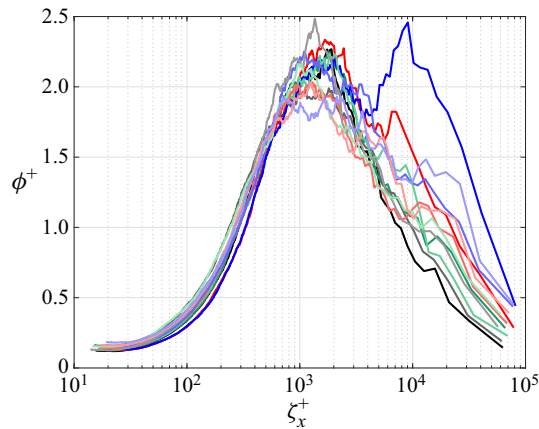


FIGURE 9. Normalized pre-multiplied velocity spectra at the near-wall spectral peak for cases REF solid black line, A solid green line, B solid red line, C solid blue with fading colours indicating increasing streamwise distance from the grid.

It is also interesting to compare case B at $x/M = 35$ (figure 8g) and case C at $x/M = 95$ (figure 8l), which have approximately the same freestream turbulence intensity $7.4\% \leq u'_\infty/U_\infty \leq 7.7\%$ and integral scale relative to the boundary layer thickness $2.6 \leq L_{u,\infty}/\delta \leq 2.7$. Their spectrograms look very different, demonstrating the importance of the evolution on the energy distribution within the boundary layer. Furthermore, when comparing cases with similar Re_τ , e.g. case A at $x/M = 95$ (figure 8f) and case C at $x/M = 35$ (figure 8j), the difference is even more apparent. Figure 8(f) shows a hint of an outer spectral peak, while figure 8(j) represents the most prominent occurrence of an outer peak of all the measurements. This underlines the fact that Re_τ must be considered alongside u'_∞/U_∞ and the evolution distance when studying TBLs subjected to FST.

6. Global trends

The way this experiment was constituted, there were two main factors modulating the boundary layer contrarily to each other. On the one hand, the TBL was evolving spatially, growing and becoming more developed. On the other hand, the FST, which artificially matured the state of evolution of the boundary layer, decayed with increasing distance x from its origin, the active grid. The streamwise evolution of a boundary layer may be expressed through $Re_x = U_\infty x/\nu$. Figure 11 summarizes how the natural growth of the boundary layer and the decay of the freestream turbulence interact, and which prevails under what conditions. The implications for different characteristics of a TBL are examined as the boundary layers evolve spatially.

The boundary layer at a single position thickens with increasing freestream turbulence intensity. As the flow evolves, the turbulence in the freestream decays and the integral scale grows. At the same time the boundary layer develops. Overall this leads to a growth of the boundary layer thickness for all levels of freestream turbulence. Figure 11(b) shows a relatively uniform stacking of the boundary layer thickness with u'_∞/U_∞ for low Re_x . As the flow develops, the higher FST intensity cases A, B and C have similar values of δ , while δ for REF is demonstrably smaller. The influence of u'_∞/U_∞ on δ decreases as the flow evolves, but a distinct difference remains between low and moderate to high FST intensity.

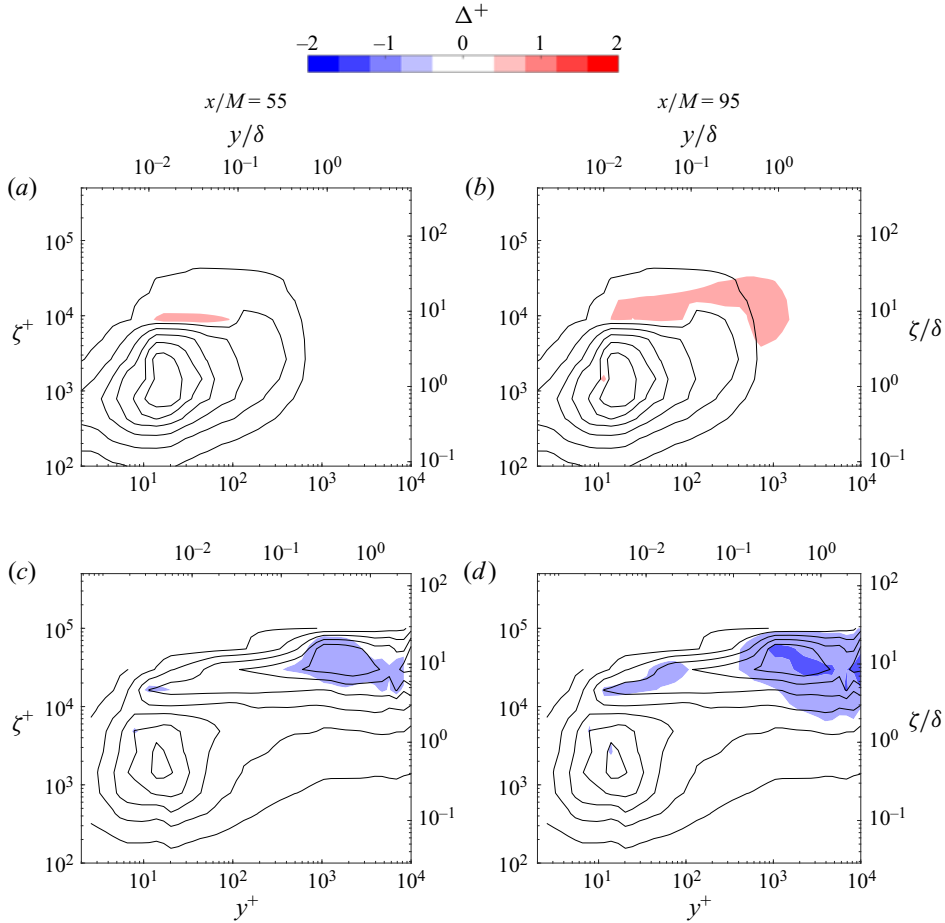


FIGURE 10. Net change $\Delta^+ = (\phi^+ - \phi_0^+)/\phi_{0,max}^+$ in spectrograms at $x/M = 55$ and $x/M = 95$ for cases REF (a,b) and C (c,d) with respect to initial spectrogram at $x/M = 35$. The contour lines of the initial spectrogram are imprinted as a reference.

For a sufficiently developed canonical turbulent boundary layer, the shape factor H decreases with increasing Re_x (Vincenti *et al.* 2013; Marusic *et al.* 2015). This decrease can also be achieved by introducing FST in the flow. The result is, contrarily to a canonical TBL, H grows with increasing Re_x as the boundary layer develops beneath decaying FST. Presumably there is a turning point when H will start decreasing again. Throughout the examined range, the shape factor remains distinguished by u'_∞/U_∞ (figure 11c). The influence of the initial difference in freestream turbulence is transported through the examined range of Re_x . Similar behaviour can be observed for the wake region of the TBL. This is quantified through Coles' wake parameter Π , which is known to trend towards a fixed value for canonical conditions with high Reynolds numbers and sufficient development length (Marusic *et al.* 2010). Freestream turbulence suppresses the intermittency in the wake region, thus leading to the suppression of the typical flow profile seen in the wake region and a significantly depleted wake parameter (Dogan *et al.* 2016). The stronger the freestream turbulence intensity, the lower Π becomes. The wake is predominantly influenced by the FST, and as it decays, the wake

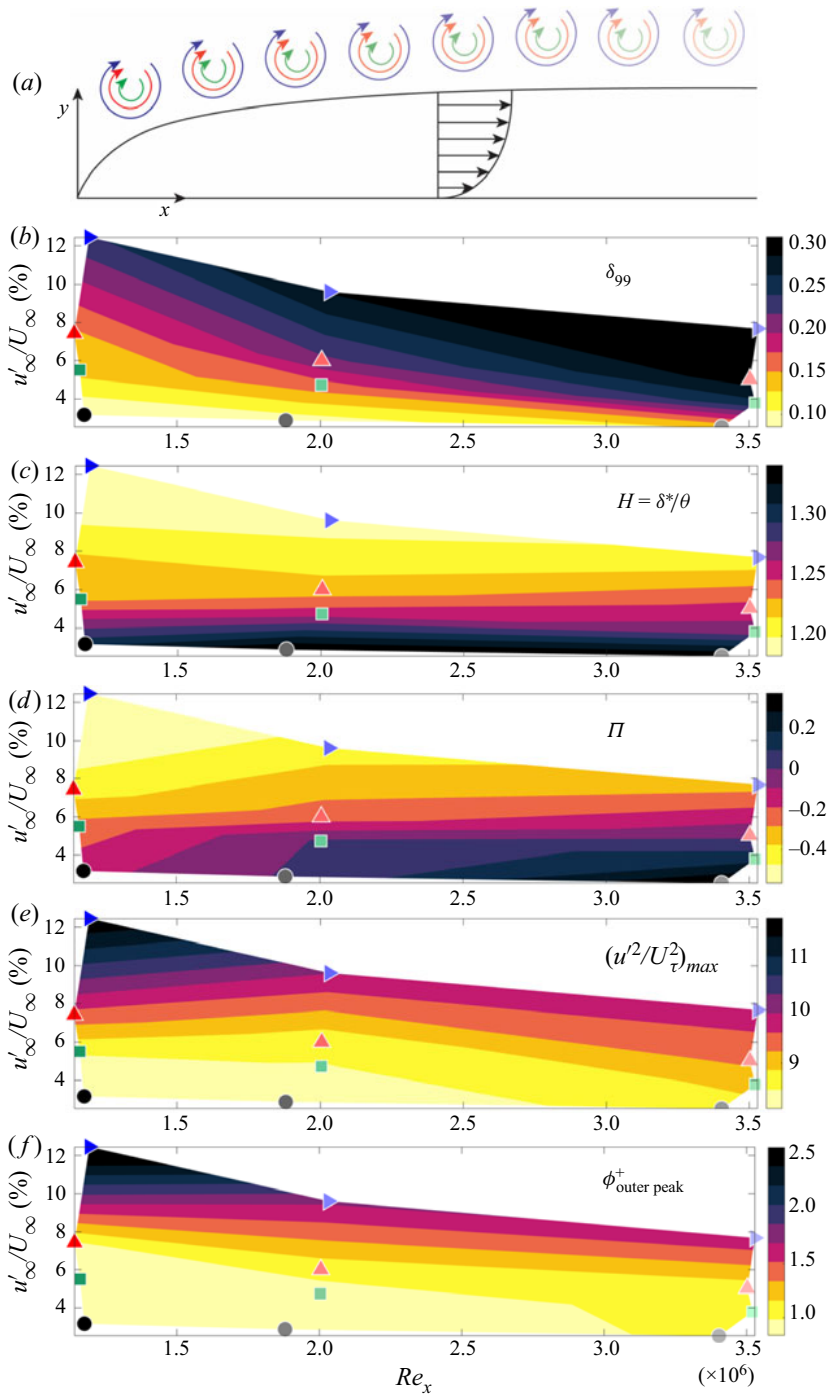


FIGURE 11. Trends for an evolving turbulent boundary layer subjected to different levels of freestream turbulence. Case REF \bullet ; A \blacksquare , green; B \blacktriangle , red; C \blacktriangleright , blue with fading colours indicating increasing streamwise distance from the grid.

becomes more pronounced. The overall change of Π with spatial evolution is more substantial than the change to H . For the lower turbulence intensities, Π approaches the analytical value of 0.55 (Coles 1956), and a visible wake region re-emerges within the investigated spatial development range (figure 5). The change in shape of the boundary layer indicates that the FST penetrates the boundary layer and has an influence on its evolution.

How deep and how significant that influence is becomes evident when looking at the modulation of the near-wall variance peak at $y^+ \approx 15$. The magnitude is strongly dependent on the level of turbulence in the freestream, with a higher turbulence intensity correlating with a higher peak in the variance. For canonical TBLs, the near-wall peak increases with the evolution of the boundary layer until the profiles become self-similar. This behaviour can be observed for lower initial freestream turbulence up to $u'_0/U_0 = 5.5\%$. For the highest freestream turbulence intensity, the decay of the turbulence proves to be dominant, as the near-wall variance peak decreases in magnitude as the flow evolves.

For high enough Re_τ , TBLs develop an outer peak in the spectral energy distribution (Hutchins & Marusic 2007). This state can also be reached by subjecting the boundary layer to high-intensity freestream turbulence (Dogan *et al.* 2016; Hearst *et al.* 2018). For canonical TBLs, this peak develops as the boundary layer grows spatially and Re_τ increases. This is observed for the lower freestream turbulence cases $3.2\% \leq u'_0/U_0 \leq 7.4\%$ here. Initially there is no outer peak visible in the spectrograms, but as the boundary layer develops, the magnitude of the outer peak gradually increases. This evolution looks very different for the highest level of freestream turbulence. A strong peak exists at the first measurement position, then proceeds to decrease with streamwise evolution of the flow. For this case, the decay of the FST appears to drive the phenomenology. The drop in outer peak magnitude is significantly higher than the observed increase for the lower FST cases (figure 11*f*). We thus again arrive at the conclusion that these flows must be parameterized by Re_τ , u'_∞/U_∞ and the streamwise development of the flow.

7. Conclusions

The evolution of a turbulent boundary layer subjected to different freestream turbulent flows was studied experimentally for $1210 \leq Re_\tau \leq 5060$. The freestream turbulence was generated with an active grid in a water channel. Boundary layer profiles were taken at three streamwise positions for four inflow turbulence intensities $3.2\% \leq u'_0/U_0 \leq 12.5\%$. It is important to appreciate that the conclusions presented herein are derived from the results of the present measurement campaign and the investigated turbulence intensities, integral scales and anisotropy. This is the first in-depth analysis of how freestream turbulence influences the characteristics of a spatially evolving turbulent boundary layer at Reynolds numbers of this magnitude. In particular, the interaction of decaying freestream turbulence with a developing turbulent boundary layer was examined. The main findings of this study are:

- (i) The development of the boundary layer mean velocity profile changes in the presence of freestream turbulence. Instead of a decrease in shape factor, as observed in canonical turbulent boundary layers (Monkewitz *et al.* 2008), H increases as the freestream turbulence decays. The suppression of the wake region for high freestream turbulence intensities observed in accordance with Blair (1983*a*), Thole & Bogard (1996) and Dogan *et al.* (2016) can be reversed as the flow

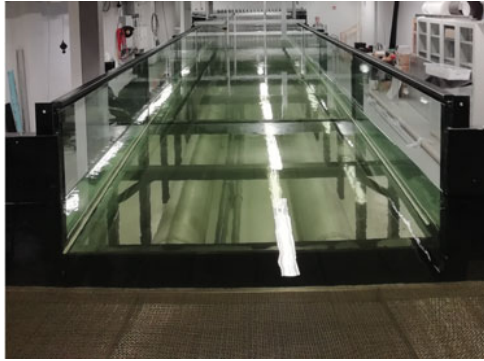


FIGURE 12. Water channel facility viewed from the end tank.

evolves downstream. It was shown that as the freestream turbulence decays below $u'_{\infty} \approx 5\%$, the wake region is recovered.

- (ii) The influence of the freestream turbulence on the magnitude of the near-wall variance peak decreases as the freestream turbulence decays in the spatially developing flow. For high-intensity FST cases, a decrease in near-wall variance peak magnitude was observed contrarily to lower freestream turbulence levels where an increase was noted with the development of the boundary layer. The latter is similar to canonical turbulent boundary layers without freestream turbulence.
- (iii) Spectral analysis showed that an outer peak in the spectrograms can be formed in two ways, and that this is pivotal for the evolution of the spectrograms. For $u'_0/U_0 = 3.2\text{-}7.4\%$, it emerges gradually as the boundary layer evolves as observed for canonical boundary layers by Hutchins & Marusic (2007) and Marusic *et al.* (2015). The mechanisms at the wall that naturally generate this peak are dominant here. However, an outer spectral peak can also be imprinted by high intensity freestream turbulence (Sharp *et al.* 2009; Dogan *et al.* 2016; Hearst *et al.* 2018). For the latter, it was demonstrated that as the flow develops spatially and the freestream turbulence decays, the outer spectral peak becomes weaker, and hence the flow does not remember that it had an outer peak earlier in its evolution. The information available in the literature does not suggest that the boundary layer would effectively regress to a less mature state once the freestream turbulence decayed, and evidence of this is presented herein for the first time.

Generally, it was found that for turbulent boundary layers subjected to freestream turbulence, the previous perspective that one could parameterize the flow with just a few parameters, i.e. Re_{τ} or Re_{θ} , u'_{∞}/U_{∞} and $L_{u,\infty}$, is incorrect. For example, flows with similar Re_{τ} , u'_{∞}/U_{∞} or $L_{u,\infty}/\delta$ can have significantly different boundary layer characteristics depending on the evolution of the freestream turbulence and boundary layer. Thus, the relative evolution of the freestream turbulence and the boundary layer must also be considered.

Funding

This work was funded by the Research Council of Norway project no. 288046 (WallMix).

Declaration of interests

The authors report no conflict of interest.

Appendix A. Water channel facility

The water channel is a recirculating facility with a capacity of 65 tons of water. A picture of the facility as viewed from the end tank is shown in [figure 12](#) and a schematic was provided in [figure 1](#). It is driven by two Siemens 1AV2186B 3-phase squirrel-cage motors each connected to two counter-rotating propellers. Each motor-pump assembly forms a part of the return pipe system that runs the length of the water channel underneath the test section. The motors are controlled via two ABB ACS550 variable frequency drives. The two return pipes supply water to the channel through a 90° bend each into a polyethylene settling chamber. The end section of the outlet is constructed from porous sheet metal to provide a diffuse source of water. A flat circular plate is also secured within the porous section to minimize the size of the water jet from the outlet. A large acrylic surface plate with adjustable height is placed above the outlet to dampen the surface waves caused by the water flowing out of the exits. After the outlet, the water flows through a porous plate, followed by a honeycomb and then a pair of stainless steel screens with progressively smaller mesh size for flow conditioning. A 4 : 1 fibreglass contraction connects the settling chamber and the test section. Between the contraction and the test section, there is a slot measuring 200 mm wide intended for the installation of turbulence generating grids. This section consists of permanently mounted acrylic frames with interchangeable inner skins, allowing for an active grid, passive grid or clean flow. The test section measures 11 m × 1.8 m × 1 m internally and is constructed from float glass panes supported by stainless steel frames. The maximum water level is 0.8 m. The clear glass construction provides optical access for laser diagnostic measurements and other optically-based measurement techniques. The water exits the test section into a stainless steel end tank, where it recirculates back to the return pipes. A stainless steel frame with wire meshes on both sides is installed in the end tank at an angle. This device acts as a wave energy dissipator to prevent large reflected waves from the end tank. The height and angle of the dissipator are adjustable. The water is kept free from debris and algae through a filter system consisting of a pump, a cyclone filter, a particle filter and a UV-lamp. There is no active temperature control for the water channel; however, once the water reaches an equilibrium with the room temperature, the daily variation in water temperature is less than 0.5 °C, which is monitored with a thermocouple.

The freestream flow velocity is measured through a Höntzsch ZS25 vane wheel flow sensor with an accuracy of 0.01 m s⁻¹. The flow sensor has an analogue current output, which is converted to an analogue voltage output and connected to a NI-9125 C series voltage input module. A T-type thermocouple is placed in the test section to measure the water temperature. It is connected to a NI-9210 C series temperature input module. Both modules are plugged into a NI cDAQ-8178 CompactDAQ chassis, which is in turn connected to a data acquisition computer.

Appendix B. Active grid

An active grid is an instrument for controlling freestream turbulence that is gaining popularity. While active grids are becoming more common, comprehensive documentation of them is still sparse. As such, this section offers a detailed description that can be potentially useful for others in the future.

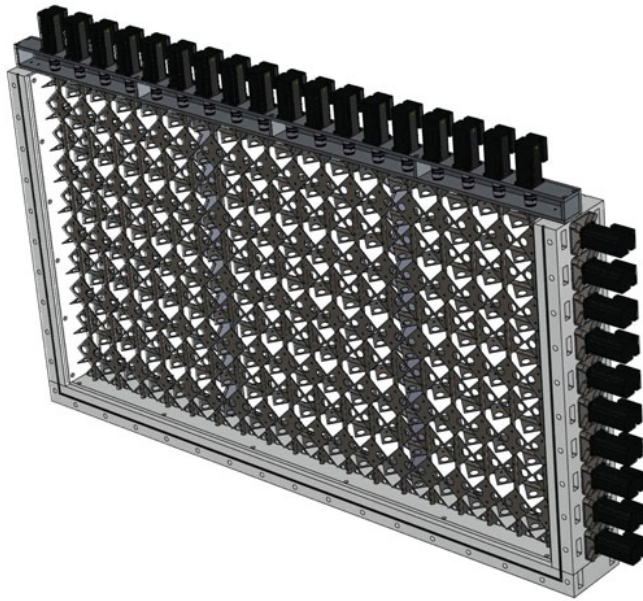


FIGURE 13. Three-dimensional view of the active grid at the water channel facility at the Norwegian University of Science and Technology.

The active grid used in the present study was designed in-house, and a three-dimensional drawing of the design is shown in [figure 13](#). It consists of 28 independently controlled stainless steel rods arranged in a biplanar square mesh, with 10 horizontal rods and 18 vertical rods. The mesh length M defined by the centre to centre distance between the rods is 100 mm, and the rods measure 12 mm in diameter. The grid stretches across the entire cross-sectional area of the test section. Stainless steel 1 mm thick square-shaped wings are attached to the rods in a space-filling manner. The sides of the wings measure 70.71 mm, such that the diagonal measures 100 mm, which matches the mesh length of the grid. Each wing has two 24 mm-diameter holes cut out of it in order to reduce the loading on the motors during actuation sequences, as well as to make sure a 100 % blockage scenario is impossible. The maximum blockage ratio achievable by the active grid is 81.9 %, and the minimum blockage ratio is 22.6 %. The rods are CNC-machined to have a 1 mm deep flat for wing mounting, such that the wings sit flush with the rod. As the maximum water level is 0.8 m, only the bottom eight horizontal rods are submerged at the maximum capacity; the top two rods are always in the air and are meant for possible future expansion of the facility. [Figure 2](#) shows the middle section of the active grid at maximum blockage. The horizontal rods are supported at four locations by low-friction plastic bushings, two at the ends and two within the grid body, located at the $\frac{1}{3}$ grid width positions from the ends. The vertical rods are secured in place at the ends through the same low-friction plastic bushings at the bottom and through stainless steel bearings at the top. The plastic bushings that support the horizontal rods are inlaid inside CNC-machined acrylic plates that attach to the permanent frame between the contraction and the test section. The plates measure 164 mm in width and span the entire inner portion of the permanent frame. They are designed to sit flush with the walls of the test section so that the flow downstream is not affected. The plates are also designed to be removable. The vertical rods are secured at the top through bearings mounted inside a custom-designed aluminium frame. The rods are then attached to the motors through a stainless steel flexible coupling

and a custom-made stainless steel coupling. This coupling is designed to interface between the flexible coupling and the motor, which have different diameter shafts. The coupling is secured onto the motor via set screws. The motors for the vertical rods are secured onto the aluminium frame, which is in turn fastened onto the permanent frame for the active grid. The horizontal rods are connected to the motors through the same mechanism, except for a custom-made water-tight mounting box for the motor. The water-tight box features a custom-designed double lip seal from Trelleborg AB sandwiched between a plastic bushing and a stainless steel bearing. The bushing is on the wet side of the seal while the bearing is on the dry side. The same custom-made coupling mentioned previously goes through the seal assembly to connect to the motor, and the motor is mounted to the dry side of the water-tight box. Large drainage openings are milled into the water-tight box so that in the event of a leakage, the water would drain away before reaching the motor, thus protecting the motors from water damage. The entire vertical rod assembly, which includes the rods with wings, aluminium frame and motors, is designed to be removable as one unit, while the horizontal rods are designed to be removable from the flexible couplings. The motors for the horizontal rods along with the water-tight boxes are permanently mounted to the side of the frame.

The motors used are STM23S-3RE stepper motors from Moons Ltd. (also marketed as Applied Motion Products in other countries). The motors are equipped with internal encoders and motion controllers. Power is supplied by two TDK-Lambda 48 V 52 A DC power supplies. Each motor can draw up to 2.5 A at 48 V. The motors are daisy-chained together and connected to a PCI serial adapter card in a computer. Unique ASCII names are given to each motor for identification by the controlling scripts. Control commands are generated and transmitted through MATLAB scripts, which can independently control each motor's rotation speed, acceleration, direction and duration. To the authors' best knowledge, this is the largest active grid installation for a water channel facility in the world at the time of writing.

Appendix C. A note on the empirical parameter of Hancock & Bradshaw (1983)

Seminal experimental works on the influence of FST on a TBL from the 1980s placed emphasis on both the turbulence intensity and the integral scale (Hancock & Bradshaw 1983, 1989; Castro 1984). In fact, Hancock & Bradshaw (1983) developed an empirical parameter, $\beta = (u'_{\infty}/U_{\infty})/(L_{u,\infty}/\delta + 2)$, which appeared to correlate well with the wall shear stress and wake in their flows. More recent studies have placed more emphasis on the turbulence intensity – e.g. Dogan *et al.* (2016); Hearst *et al.* (2018) – with the latter even proposing that for higher turbulence intensities, the integral scale does not necessarily play a significant role. The primary difference between the earlier studies and contemporary ones is that the recent use of active grids has allowed for high turbulence intensity ($> 10\%$) to be achieved much farther downstream from the turbulence generating grid ($x/M > 30$). Hearst *et al.* (2018) noticed that one of the reasons for this result appeared to be that δ adjusts itself such that the peak in the premultiplied energy spectrum is at approximately $\sim 10\delta$. This appeared to be true for all 17 of their cases with $7\% \lesssim u'_{\infty}/U_{\infty} \lesssim 13\%$, see their figure 1(b). This was in fact first noticed by Dogan *et al.* (2016) in their figure 8, although they did not emphasize it as strongly. This is also approximately true in the present investigation, particularly for the more turbulent cases, as depicted in figure 14. This relationship suggests that given sufficient coevolution distance, the energy containing scales and the boundary layer height adjust to keep a constant proportionality between them (Hearst *et al.* 2018). Thus, $L_{u,\infty}$ and δ are co-dependent, and the ratio $L_{u,\infty}/\delta$ is relatively constant, whilst the turbulence intensity decays, resulting in the appearance

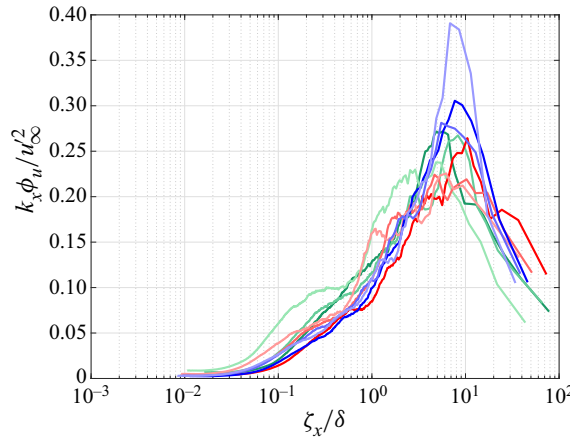


FIGURE 14. Normalized pre-multiplied velocity spectra in the freestream for cases A solid green line, B solid red line, C solid blue line with fading colours indicating increasing streamwise distance from the grid.

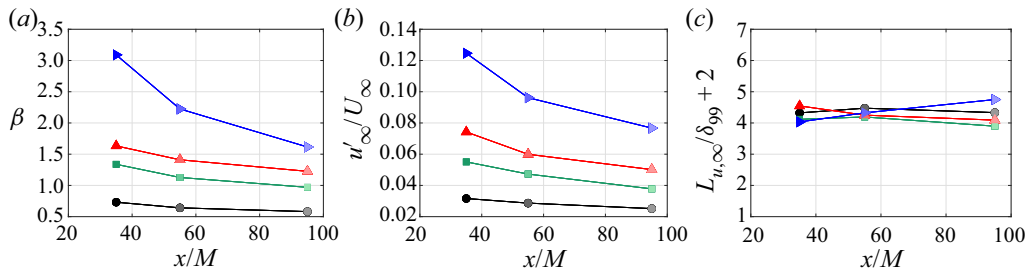


FIGURE 15. Analysis of the empirical parameter β introduced by Hancock & Bradshaw (1983) for cases REF \bullet ; A \blacksquare , green; B \blacktriangle , red; C \blacktriangleright , blue. Note that the scaling on these figures was chosen to represent equal changes in β and the two contributing parameters included in it.

of primary dependence on the turbulence intensity. It is important to acknowledge that although this result has been observed in two different facilities, it is possible that it is a consequence of the integral scales produced in those studies, and that if significantly larger or smaller integral scales were investigated, a different result or trend may emerge.

For completeness, we present β along with u'_∞ / U_∞ and $L_{u,\infty} / \delta + 2$ in figure 15, with the y-axis scaled to show the same percentage change on all figures. It is evident that when scaled in this way, β predominantly follows u'_∞ / U_∞ , and $L_{u,\infty} / \delta + 2$ is approximately constant. In §§ 4 and 5 it was also shown that for cases with similar $L_{u,\infty} / \delta$, the mean profiles and spectrograms could look very different. Thus, while the integral scale likely does play some role, this role is small compared to the turbulence intensity and evolution history, at least for the test cases investigated herein.

REFERENCES

- ADRIAN, R. J. & YAO, C. S. 1986 Power spectra of fluid velocities measured by laser Doppler velocimetry. *Exp. Fluids* **5** (1), 17–28.
- ANDERSON, J. D. 2010 *Fundamentals of Aerodynamics*. McGraw-Hill Education.

- BAARS, W. J., HUTCHINS, N. & MARUSIC, I. 2016 Spectral stochastic estimation of high-Reynolds-number wall-bounded turbulence for a refined inner-outer interaction model. *Phys. Rev. Fluids* **1** (5), 054406.
- BLAIR, M. F. 1983*a* Influence of free-stream turbulence on turbulent boundary layer heat transfer and mean profile development, part ii—analysis of results. *Trans. ASME: J. Heat Transfer* **105** (1), 41–47.
- BLAIR, M. F. 1983*b* Influence of free-stream turbulence on turbulent boundary layer heat transfer and mean profile development, part i—experimental data. *Trans. ASME: J. Heat Transfer* **105** (1), 33–40.
- BOYER, L. & SEARBY, G. 1986 Random sampling: distortion and reconstruction of velocity spectra from fast Fourier-transform analysis of the analog signal of a laser Doppler processor. *J. Appl. Phys.* **60** (8), 2699–2707.
- CASTRO, I. P. 1984 Effects of free stream turbulence on low Reynolds number boundary layers. *Trans. ASME: J. Fluids Engng* **106** (3), 298–306.
- CHAUHAN, K. A., MONKEWITZ, P. A. & NAGIB, H. M. 2009 Criteria for assessing experiments in zero pressure gradient boundary layers. *Fluid Dyn. Res.* **41** (2), 021404.
- COLES, D. 1956 The law of the wake in the turbulent boundary layer. *J. Fluid Mech.* **1** (2), 191–226.
- COMTE-BELLOT, G. & CORRISIN, S. 1966 The use of a contraction to improve the isotropy of grid-generated turbulence. *J. Fluid Mech.* **25** (4), 657–682.
- DEVINANT, P., LAVERNE, T. & HUREAU, J. 2002 Experimental study of wind-turbine airfoil aerodynamics in high turbulence. *J. Wind Engng Ind. Aerodyn.* **90** (6), 689–707.
- DOGAN, E., HANSON, R. E. & GANAPATHISUBRAMANI, B. 2016 Interactions of large-scale free-stream turbulence with turbulent boundary layers. *J. Fluid Mech.* **802**, 79–107.
- DOGAN, E., HEARST, R. J. & GANAPATHISUBRAMANI, B. 2017 Modelling high Reynolds number wall–turbulence interactions in laboratory experiments using large-scale free-stream turbulence. *Phil. Trans. R. Soc. A* **375** (2089), 20160091.
- DOGAN, E., HEARST, R. J., HANSON, R. E. & GANAPATHISUBRAMANI, B. 2019 Spatial characteristics of a zero-pressure-gradient turbulent boundary layer in the presence of free-stream turbulence. *Phys. Rev. Fluids* **4** (8), 084601.
- EITEL-AMOR, G., ÖRLÜ, R. & SCHLATTER, P. 2014 Simulation and validation of a spatially evolving turbulent boundary layer up to $Re_\theta = 8300$. *Intl J. Heat Fluid Flow* **47**, 57–69.
- ERTUNÇ, Ö., ÖZYILMAZ, N., LIENHART, H., DURST, F. & BERONOV, K. 2010 Homogeneity of turbulence generated by static-grid structures. *J. Fluid Mech.* **654**, 473–500.
- ESTEBAN, L. B., DOGAN, E., RODRÍGUEZ-LÓPEZ, E. & GANAPATHISUBRAMANI, B. 2017 Skin-friction measurements in a turbulent boundary layer under the influence of free-stream turbulence. *Exp. Fluids* **58** (9), 115.
- FERRANTE, A. & ELGHOBASHI, S. 2004 On the physical mechanisms of drag reduction in a spatially developing turbulent boundary layer laden with microbubbles. *J. Fluid Mech.* **503**, 345–355.
- GANAPATHISUBRAMANI, B. 2018 Law of the wall for small-scale streamwise turbulence intensity in high-Reynolds-number turbulent boundary layers. *Phys. Rev. Fluids* **3** (10), 104607.
- HANCOCK, P. E. & BRADSHAW, P. 1983 The effect of free-stream turbulence on turbulent boundary layers. *Trans. ASME: J. Fluids Engng* **105** (3), 284–289.
- HANCOCK, P. E. & BRADSHAW, P. 1989 Turbulence structure of a boundary layer beneath a turbulent free stream. *J. Fluid Mech.* **205**, 45–76.
- HEARST, R. J., BUXTON, O. R. H., GANAPATHISUBRAMANI, B. & LAVOIE, P. 2012 Experimental estimation of fluctuating velocity and scalar gradients in turbulence. *Exp. Fluids* **53** (4), 925–942.
- HEARST, R. J., DOGAN, E. & GANAPATHISUBRAMANI, B. 2018 Robust features of a turbulent boundary layer subjected to high-intensity free-stream turbulence. *J. Fluid Mech.* **851**, 416–435.
- HEARST, R. J. & LAVOIE, P. 2015 The effect of active grid initial conditions on high Reynolds number turbulence. *Exp. Fluids* **56** (10), 185.
- HUTCHINS, N. & MARUSIC, I. 2007 Evidence of very long meandering features in the logarithmic region of turbulent boundary layers. *J. Fluid Mech.* **579**, 1–28.
- ISAZA, J. C., SALAZAR, R. & WARHAFT, Z. 2014 On grid-generated turbulence in the near- and far field regions. *J. Fluid Mech.* **753**, 402–426.

- KANG, H. S., CHESTER, S. & MENEVEAU, C. 2003 Decaying turbulence in an active-grid-generated flow and comparisons with large-eddy simulation. *J. Fluid Mech.* **480**, 129–160.
- KOZUL, M., HEARST, R. J., MONTY, J. P., GANAPATHISUBRAMANI, B. & CHUNG, D. 2020 Response of the temporal turbulent boundary layer to decaying free-stream turbulence. *J. Fluid Mech.* **896**, A11.
- LARSEN, J. V. & DEVENPORT, W. J. 2011 On the generation of large-scale homogeneous turbulence. *Exp. Fluids* **50** (5), 1207–1223.
- LASKARI, A., DE KAT, R., HEARST, R. J. & GANAPATHISUBRAMANI, B. 2018 Time evolution of uniform momentum zones in a turbulent boundary layer. *J. Fluid Mech.* **842**, 554–590.
- LAVOIE, P., DJENIDI, L. & ANTONIA, R. A. 2007 Effects of initial conditions in decaying turbulence generated by passive grids. *J. Fluid Mech.* **585**, 395–420.
- MAKITA, H. 1991 Realization of a large-scale turbulence field in a small wind tunnel. *Fluid Dyn. Res.* **8**, 53.
- MALDONADO, V., CASTILLO, L., THORMANN, A. & MENEVEAU, C. 2015 The role of free stream turbulence with large integral scale on the aerodynamic performance of an experimental low Reynolds number S809 wind turbine blade. *J. Wind Engng Ind. Aerodyn.* **142**, 246–257.
- MARUSIC, I., CHAUHAN, K. A., KULANDAIVELU, V. & HUTCHINS, N. 2015 Evolution of zero-pressure-gradient boundary layers from different tripping conditions. *J. Fluid Mech.* **783**, 379–411.
- MARUSIC, I., MCKEON, B. J., MONKEWITZ, P. A., NAGIB, H. M., SMITS, A. J. & SREENIVASAN, K. R. 2010 Wall-bounded turbulent flows at high Reynolds numbers: recent advances and key issues. *Phys. Fluids* **22** (6), 065103.
- MARUSIC, I., MONTY, J. P., HULTMARK, M. & SMITS, A. J. 2013 On the logarithmic region in wall turbulence. *J. Fluid Mech.* **716**, R3.
- MOHAMED, M. S. & LARUE, J. C. 1990 The decay power law in grid-generated turbulence. *J. Fluid Mech.* **219**, 195–214.
- MONKEWITZ, P. A., CHAUHAN, K. A. & NAGIB, H. M. 2008 Comparison of mean flow similarity laws in zero pressure gradient turbulent boundary layers. *Phys. Fluids* **20** (10), 105102.
- PERRY, A. E., MARUSIC, I. & JONES, M. B. 1998 New evolution equations for turbulent boundary layers in arbitrary pressure gradients. *Sadhana* **23** (5), 443–457.
- PRANDTL, L. 1905 über Flüssigkeitsbewegung bei sehr kleiner Reibung. In *Proceedings of the 3rd International Congress of Mathematicians, Heidelberg, 1904, Leipzig*, pp. 485–491. B. G. Teubner.
- RAUSHAN, P. K., SINGH, S. K. & DEBNATH, K. 2018 Grid generated turbulence under the rigid boundary influence. *J. Wind Engng Ind. Aerodyn.* **182**, 252–261.
- RODRÍGUEZ-LÓPEZ, E., BRUCE, P. J. K. & BUXTON, O. R. H. 2015 A robust post-processing method to determine skin friction in turbulent boundary layers from the velocity profile. *Exp. Fluids* **56** (4), 68.
- SHARP, N. S., NEUSCAMMAN, S. & WARHAFT, Z. 2009 Effects of large-scale free stream turbulence on a turbulent boundary layer. *Phys. Fluids* **21** (9), 095105.
- SILLERO, J. A., JIMÉNEZ, J. & MOSER, R. D. 2013 One-point statistics for turbulent wall-bounded flows at Reynolds numbers up to $\delta^+ \approx 2000$. *Phys. Fluids* **25** (10), 105102.
- SMITS, A. J. & MARUSIC, I. 2013 Wall-bounded turbulence. *Phys. Today* **66** (9), 25.
- STEFES, B. & FERNHOLZ, H. H. 2004 Skin friction and turbulence measurements in a boundary layer with zero-pressure-gradient under the influence of high intensity free-stream turbulence. *Eur. J. Mech. B/Fluids* **23** (2), 303–318.
- THOLE, K. A. & BOGARD, D. G. 1996 High freestream turbulence effects on turbulent boundary layers. *Trans. ASME: J. Fluids Engng* **118** (2), 276–284.
- VINCENTI, P., KLEWICKI, J., MORRILL-WINTER, C., WHITE, C. M. & WOSNIK, M. 2013 Streamwise velocity statistics in turbulent boundary layers that spatially develop to high Reynolds number. *Exp. Fluids* **54** (12), 1629.
- WANG, S., ZHOU, Y., ALAM, M. M. & YANG, H. 2014 Turbulent intensity and Reynolds number effects on an airfoil at low Reynolds numbers. *Phys. Fluids* **26** (11), 115107.
- WU, X. & MOIN, P. 2009 Direct numerical simulation of turbulence in a nominally zero-pressure-gradient flat-plate boundary layer. *J. Fluid Mech.* **630**, 5–41.

- WU, X., MOIN, P., WALLACE, J. M., SKARDA, J., LOZANO-DURÁN, A. & HICKEY, J.-P. 2017 Transitional–turbulent spots and turbulent–turbulent spots in boundary layers. *Proc. Natl Acad. Sci.* **114** (27), E5292–E5299.
- WU, X., WALLACE, J. M. & HICKEY, J.-P. 2019 Boundary layer turbulence and freestream turbulence interface, turbulent spot and freestream turbulence interface, laminar boundary layer and freestream turbulence interface. *Phys. Fluids* **31** (4), 045104.
- YOU, J. & ZAKI, T. A. 2019 Conditional statistics and flow structures in turbulent boundary layers buffeted by free-stream disturbances. *J. Fluid Mech.* **866**, 526–566.

Article II





**Flow field and performance of a
vertical axis wind turbine on model
buildings**

Yannick Jooss, Roberto Bolis, Tania Bracchi, R. Jason Hearst

Published in:
Flow, 2.

RESEARCH ARTICLE

Flow field and performance of a vertical-axis wind turbine on model buildings

Yannick Jooss¹ , Roberto Bolis² , Tania Bracchi¹  and R. Jason Hearst^{1,*} 

¹Department of Energy and Process Engineering, Norwegian University of Science and Technology, Trondheim, Norway

²School of Industrial and Information Engineering, Politecnico di Milano, Milan, Italy

*Corresponding author. E-mail: jason.hearst@ntnu.no

Received: 12 June 2021; **Revised:** 26 January 2022; **Accepted:** 16 March 2022

Keywords: Urban fluid dynamics; Wind turbines; Complex terrain; Turbulent flows

Abstract

The placement of a scaled-down Savonius (drag) vertical-axis wind turbine on model buildings is analysed experimentally by the use of turbine performance and flow field measurements in a wind tunnel. The set-up consists of two surface mounted cubes aligned in the flow direction. The turbine is tested at six different streamwise positions – three on each cube. Velocity field measurements are performed with particle image velocimetry along the centreline of the cubes with and without the turbine. The performance at each position is evaluated based on measurements of the produced torque and the rotational speed of the turbine. It is demonstrated that the common practice of estimating wind resources based on the urban flow field without the turbine present is insufficient. The turbine has a substantial influence on the flow field and thus also on the available power. The performance is found to be optimal in the front and centre of the first building with a significant drop-off to the back. This trend is reversed for the downstream building. Holistically, for more generic geometries and varying wind directions, the results suggest the central position on a building is a good compromise.

Impact Statement

Urban wind energy presents untapped potential for decentralized energy generation from renewable sources. One aspect impeding its wider use is the complicated flow field that exists within the complex terrain of urban areas. The flow is highly dependent on the local topology, which makes the positioning of a wind turbine a key parameter. We investigate this problem with particle image velocimetry, allowing for high fidelity analysis of the flow field and its statistics around two model buildings. Power measurements of a vertical-axis wind turbine on the model buildings demonstrate how the positioning of the turbine can influence the produced power by 84 %. In addition, it is shown that the turbine itself has a significant impact on the flow field and thus on the available power, which is considerably different from estimates made from the flow field without a turbine.

1. Introduction

The world energy demand is projected to rise, with renewable energies playing an increasing role in meeting this demand (IEA, 2020). Wind energy is expected to be one of the key contributors in this process. An important challenge in advancing this technology is to improve performance predictions of wind turbines and wind farms (Porté-Agel, Bastankhah, & Shamsoddin, 2020). A large share of

this contribution will come from large-scale turbines and farms. However, there are also barriers to this path (Musial & Ram, 2010), such as available sites, impact of grid power quality, losses during transmission and distribution of the electricity to the consumer, as well as public acceptance (Kc, Whale, & Urmee, 2019). Some of these can be mitigated with more decentralized electricity generation (Chicco & Mancarella, 2009) involving renewable energy sources, such as small wind turbines in the built environment or in complex terrain. (Kc et al. 2019) identified a proper assessment of the urban wind resources as a key aspect requiring further investigation in this field. The wind field in an urban environment can be divided into two layers conceptually (Oke, 1976). From the bottom there is the urban canopy layer, extending up to the roof height (h) of the buildings. Here the flow is complex and dominated by microscale effects (Oke, 1976, 1988; Wang et al., 2014). Above that lies the urban boundary layer which again can be divided into multiple layers (Oke, 1988). This includes the roughness sublayer extending from the roof height up to $2h$ – $5h$ (Raupach, Antonia, & Rajagopalan, 1991). Here, the flow is still strongly affected by the geometry, size and layout of individual buildings (Millward-Hopkins, Tomlin, Ma, Ingham, & Pourkashanian, 2012; Wang et al., 2014). Above that are the surface and mixed layers, where the flow becomes homogeneous in the horizontal plane (Cheng & Castro, 2002). Roof-mounted wind turbines are typically placed in the roughness sublayer (Millward-Hopkins et al., 2012). The flow here is complex and manifold, dependent on the local topology. This makes a general assessment of the wind resources for roof-mounted wind turbines challenging.

The predominant method of analysis thus far has been numerical studies, often solving the Reynolds-averaged Navier–Stokes (RANS) equations. Amongst other things, the influence of the roof shape (Abohela, Hamza, & Dudek, 2013; Ledo, Kosasih, & Cooper, 2011; Toja-Silva, Peralta, Lopez-Garcia, Navarro, & Cruz, 2015; Yang et al., 2016) and neighbouring buildings (Lu & Ip, 2009; Mertens, 2003) have been examined. However, RANS simulations are sensitive to the choice of turbulence model, which is often case specific (Kc et al., 2019). Moreover, they are modelling the complex turbulence interactions which dominate this process. Experimental data is thus required, to both improve numerical models as well as to advance the understanding of the wind resources for roof mounted wind turbines (Stathopoulos et al., 2018). On-site measurements remain the benchmark methodology to evaluate wind resources. However, these field measurements may be performed in locations that are not easily accessible and they are usually expensive, especially if good spatial and temporal resolution is desired. While the relative costs of on-site measurements are typically small for large wind turbine projects, they can become significant for small installations (Kalmikov, Dupont, Dykes, & Chan, 2010). Al-Quraan, Stathopoulos, and Pillay (2016) showed that wind tunnel measurements can help to bridge this gap. For a site with homogeneous terrain, a high correlation between wind tunnel and on-site measurements was achieved, and even for a site with non-homogeneous terrain an initial evaluation of the wind resource was found to be feasible in a wind tunnel. Glumac, Hemida, and Höffer (2018), Vita, Glumac, Hemida, Salvadori, and Baniotopoulos (2020) and Hemida, Glumac, Vita, Kostadinović Vranešević, and Höffer (2020) conducted wind tunnel studies on wind resources above a high-rise building. The influence of four surrounding buildings with a distance of two building widths and varying roof shapes was examined for different wind directions. Velocity measurements above the central building showed a reduction of the wind velocity and an increase in turbulence intensity when the analysed building was positioned in the wake of an upstream building. This was concluded to be unfavourable for the extraction of power.

None of the aforementioned studies measured the power extraction of a wind turbine directly. Conclusions were typically only drawn from velocity fields. The streamwise wind velocity U at the potential turbine position, or deduced from that, the available wind power $P_a = \frac{1}{2}A\rho U^3$ was analysed, where ρ is the fluid density and A is the presumed rotor area. Other flow parameters reported were the skew angle of the velocity $\gamma = \tan^{-1}(W/U)$, the turbulence intensity u'/U , or the turbulent kinetic energy $k = \frac{1}{2}(\overline{u'^2} + \overline{v'^2} + \overline{w'^2})$, where W is the wall-normal velocity and u' , v' and w' represent the fluctuations in the three flow directions.

While this approach, based on P_a , gives a lot of insight and is heavily employed in wind resource assessment, it can be problematic when applying it to the roughness sublayer, and especially to roof-mounted wind turbines. The flow dynamics here are non-uniform and strongly dependent on the

local topology, e.g. building shape and surroundings. Wind turbines are large rotating objects with the potential to alter the flow field themselves. Blockage effects are acknowledged to be relevant for wind turbines and farms (Medici, Ivanell, Dahlberg, & Alfredsson, 2011; Porté-Agel et al., 2020; Simley et al., 2016). These also remain relevant in complex terrain, as shown by (Yan et al. 2018). While roof-mounted wind turbines are usually smaller, so are the length scales of local flow phenomena caused by the non-uniform topology. Furthermore, the flow a turbine experiences in an urban environment is typically not only highly turbulent but also intermittent in U , γ and k (Kc et al., 2019) and often heavily sheared in at least one direction. The interaction of this flow with an energy extracting machine, such as a wind turbine, is complex and thus not easily predictable. Some of these effects can be modelled (Bazilevs et al., 2014) but in complex flow fields the power typically is still estimated based on local velocities and not measured directly (Ge, Gayme, & Meneveau, 2021).

Studies subjecting wind turbines to flows approximating urban conditions have been conducted to evaluate the suitability of different turbine types (e.g. Aliferis, Jessen, Bracchi, & Hearst, 2019; Danao, Eboibi, & Howell, 2013; Loganathan, Mustary, Chowdhury, & Alam, 2017; Scheurich & Brown, 2013; Wekesa, Wang, Wei, & Zhu, 2016). Typically the influence of one or some of the features of the urban wind resources were examined. The influence of an urban flow field with all its characteristics on the performance of a wind turbine is difficult to emulate. (Kooiman and Tullis 2010) placed a Darrieus (lift) type vertical-axis wind turbine (VAWT) in a real urban environment and compared its performance there with measurements of the same turbine in a wind tunnel. The performance was found to be reduced for turbulence intensities higher than 15 %. (Pagnini, Burlando, and Repetto 2015) measured the performance of a horizontal-axis wind turbine (HAWT) and a VAWT at the same location in a real urban environment. While the HAWT gave a higher power output overall, the VAWT proved to be more robust to gusts and high wind velocities. Recently (Pellegrini, Guzzini, and Saccani 2021) installed a small HAWT in an urban environment and monitored the turbine performance for 12 months. Due to low average wind velocities the installation proved to be not sustainable economically. Studies like these are rare and mostly limited to single locations. The influence of the roof-mounting position of a turbine on its actual power output thus remains an open question. To parameterize this, in the present study a model VAWT was placed on idealized scaled-down buildings in a wind tunnel. The flow field was acquired with and without the turbine present. In addition, the power the turbine extracted at different positions was measured.

Vertical-axis wind turbines have received increasing attention both for their use in wind farms (Brownstein, Kinzel, & Dabiri, 2016; Dabiri, 2011; Kinzel, Mulligan, & Dabiri, 2012) as well as in the built environment (Hui, Cain, & Dabiri, 2018; Kc et al., 2019; Li, Wang, & Yuan, 2010; Mertens, 2003). They are considered to be well suited for the urban environment due to their insensitivity to flow direction and also due to their low noise levels (Kooiman & Tullis, 2010). For example Aeolos, CleanVerTec, Quietrevolution, Greener Energy, Semtive and the Solar Impulse Foundation offer VAWTs designed for the built environment with turbine heights (h_T) of 1 m to 6.2 m. Turbines in the same size range are also obtainable by the generic consumer directly from Amazon. These turbines yield size ratios of $0.23 \lesssim h_T/h \lesssim 1.44$ when mounted on average one-storey buildings, $0.13 \lesssim h_T/h \lesssim 1.03$ on average on two-storey buildings and $0.08 \lesssim h_T/h \lesssim 0.62$ on average on three-storey buildings. A prominent example of such an installation is the Greenpeace facility in Hamburg. Three CleanVerTec CVT-V100 VAWTs with a turbine height of $h_T = 6.2$ m and a rated output of 12.5 kW were installed on a 24 m high building in 2013. This resulted in a size ratio of h_T/h of 0.26.

In the present study, the modelled urban environment was chosen to be as generic as possible while still being representative. Two surface-mounted cubes were positioned in line with each other, in a so-called tandem arrangement. The upstream cube represents a building relatively unaffected by its surroundings. The downstream cube enabled the evaluation of the influence of an upstream building with comparable height on both wind resources and wind turbine performance. The use of surface-mounted cubes as idealized buildings is a common approach in the assessment of urban wind resources (Ge et al., 2021; Millward-Hopkins et al., 2012). A more detailed description of the experimental set-up is given in § 2.

The flow around a surface-mounted cube has been studied extensively (e.g. [Castro & Robins, 1977](#); [Hearst, Gomit, & Ganapathisubramani, 2016](#); [Yakhot, Liu, & Nikitin, 2006](#)). The scalability of this configuration yields a wide range of applications, from small-scale roughness elements to complex terrain such as buildings of various sizes, as in the present study. Also the flow around a matrix of cubical bodies has been the subject of numerous studies (e.g. [Cheng, Lien, Yee, & Sinclair, 2003](#); [Ferreira & Ganapathisubramani, 2021](#); [Fuka et al., 2018](#); [Meinders & Hanjalić, 1999](#); [Xie & Castro, 2006](#); [Xie, Coceal, & Castro, 2008](#)), often with the motivation of learning more about the flow in urban environments. A little less explored is the flow around cubes in a tandem arrangement. ([Martinuzzi and Havel 2000](#)) studied this problem, varying the spacing (s) between the cubes from one cube height (h) to $4h$. The cubes were placed on an artificial floor to obtain uniform inflow with a thin boundary layer. The flow field was measured with laser Doppler velocimetry (LDV). Their main findings are elaborated here to give some background on the underlying flow physics. They showed that for Reynolds numbers $Re_h = U_\infty h / \nu = 12\,000$ to $40\,000$, where U_∞ is the incoming velocity and ν is the viscosity of the fluid, the flow field was independent of Re_h . As for single cubes, the flow separates on the upstream edge of the first cube, independent of s . They found three different regimes dependent on the spacing s/h . For $s/h < 1.4$ the flow reattaches on the roof of the second cube and a large low turbulence recirculation zone forms between the cubes. Spacings larger than $s/h = 3.5$ let the flow reattach in-between the cubes, and with increasing s/h the flow around the second cube approaches the flow around the first cube. In-between exists a regime where the separated flow from the first cube impinges on the windward top edge of the second cube. Also, fluid from the side is entrained, leading to increased levels of turbulence in-between the cubes. Periodic vortex shedding was found both in-between the cubes and downstream of the whole arrangement. The flow field was further examined for a spacing of $s/h = 2$ in a second study ([Martinuzzi & Havel, 2004](#)).

This study thus uses a cube spacing of $s/h = 2$, utilizing ([Martinuzzi and Havel 2004](#)) as a reference for the flow field. On these cubes, turbines of $h_T/h = 0.3$ are mounted, which is representative of the aforementioned examples. The turbines are placed at six sample positions and their power output and resulting flow fields are measured. The latter provides insight on how the power changes based on turbine location in this arrangement. We are thus able to identify both how the power output of the turbine changes and why it changes, providing a full picture of the problem.

2. Experimental set-up

All measurements were conducted in the large-scale wind tunnel at the Norwegian University of Science and Technology. This is a closed-loop tunnel with a $2.71\text{ m} \times 1.80\text{ m} \times 11.15\text{ m}$ (width \times height \times length) test section. The set-up was positioned on a $1.8\text{ m} \times 3\text{ m} \times 0.01\text{ m}$ (width \times length \times thickness) flat plate, acting as an artificial floor. A schematic of this is shown in [figure 1\(a\)](#). The plate was mounted on legs attached to the tunnel floor. The leading edge of the plate was sharpened to a 15° angle to avoid detachment of the flow there. A roughness strip downstream of the leading edge was used to trip the boundary layer on the artificial floor. Two $h = 100\text{ mm}$ cubes are placed on the flat plate. The front of the first cube was positioned $5h$ downstream of the leading edge of the plate. The distance between the two cubes was $s = 2h$. A coordinate system with $x = 0$ at the centre of the first cube and $z = 0$ at the artificial floor, as shown in [figure 1\(a\)](#), was used. Including the support structure, the blockage of the whole system was below 3.8%, so blockage effects can be considered negligible ([West & Apelt, 1982](#)).

A VAWT of the Savonius (drag) type was positioned on top of the cubes. The two-bladed turbine has a diameter d_T of $0.4h$ and a blade height h_T of $0.3h$. The relative size of the turbine to the cube might appear ‘large’, but is in fact representative of VAWT installations on smaller buildings and in residential areas. The investigated h_T/h corresponds to size ratios found for average one- to three-storey buildings (see § 1). In addition, experimental considerations played into the selection of this h_T/h . First, the size of the turbine places it within the shear flow region so that we can study its effects. Second, the size of the turbine was required so that it is both autostarting and that it produced sufficient power such that it is readily measured. Note that a wide range of operating conditions needed to be covered as

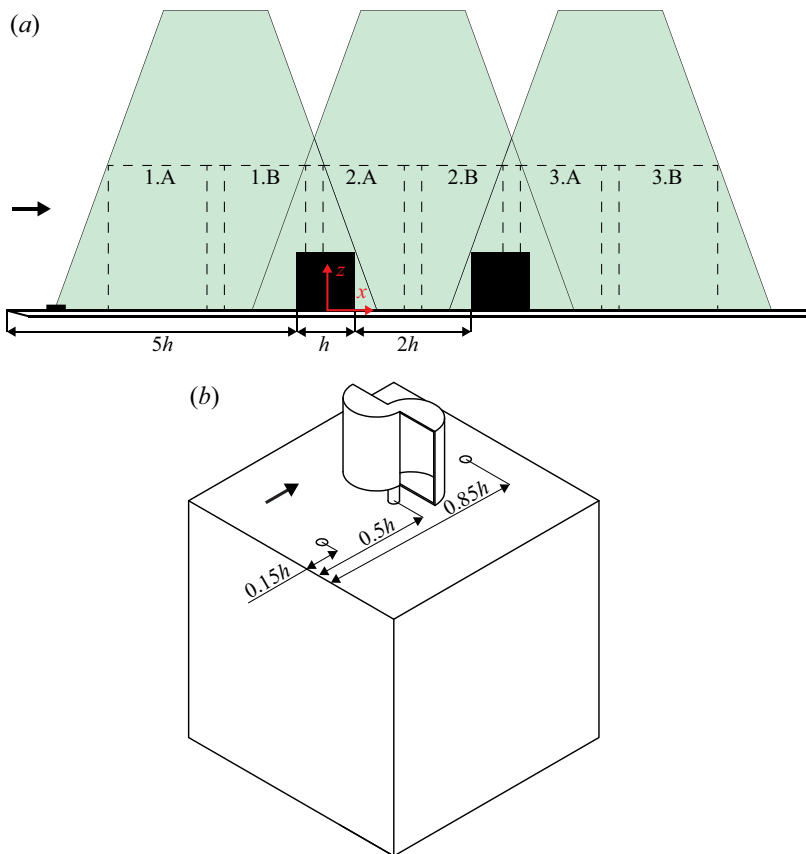


Figure 1. (a) Schematic of the experimental set-up. The flow fields were acquired in three separate acquisitions with two cameras (A and B). (b) The wind turbine was placed at three different positions along the centreline on each cube.

the available power varied significantly between the examined cases. Finally, the cube size was limited by our ability to create a large measurement area. Consider that the total field of view (FOV) in the present study is $1040 \text{ mm} \times 250 \text{ mm}$, which is quite large for laboratory scale PIV and cannot easily be stretched further. The interaction between the flow field and the turbine is a crucial element of this study. Scaling the cubes up in this FOV would have led to a loss of information on the flow field the turbines are placed in. While the results presented herein are insightful, certainly it would be interesting for future studies to investigate changes to the relative size of the turbine and building. The turbine was 3-D printed out of polylactide (PLA) with a fineness of 0.6 mm . Inspiration for the design of the VAWT was taken from (Akwa, Vielmo, and Petry 2012). Figure 2 shows the cross-section of the turbine. It consists of two semicircles overlapping by $0.125d_T$ in the centre, which are held in place by end plates on top and bottom. The overlap was added to decrease the starting torque (Kumbernuss, Chen, Yang, & Lu, 2012). The turbine shaft has a diameter of $0.04h (= 0.1d_T)$. The design was deliberately chosen to be generic and reproducible. The goal of the study is to compare different turbine positions, not to optimize the turbine itself. Its position was varied in the streamwise direction along the centreline of the cubes, with three positions on top of each cube at $0.15h$ (front), $0.50h$ (central) and $0.85h$ (back), as illustrated in figure 1(b). An alphanumeric system is used to identify the position of the turbine on the cubes, where 1 and 2 are used to denote the front and back cube, and F, C and B are used to denote a turbine in the front, central and back positions on the identified cube. The distance from the roof to the lowest point of the turbine blades was kept constant at $0.08h (= 0.2d_T)$. For each of these cases flow and

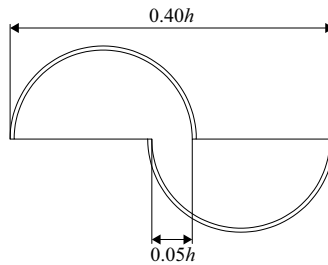


Figure 2. Cross-section of the Savonius turbine used for the experiments. The blade height corresponds to $0.3h$.

performance measurements were carried out. In addition the flow was also measured around the cubes without a turbine and on the plate without the cubes. The mean incoming velocity was kept constant at $12.05 \text{ m s}^{-1} \pm 0.03 \text{ m s}^{-1}$ which lead to Reynolds numbers of $Re_h \approx 80\,000$ and $Re_{d_T} = U_\infty d_T / \nu \approx 32\,000$ for all cases. The reference velocity U_∞ was taken upstream and above the cubes at $x = -3.5h$, averaged over $2 \leq z/h \leq 2.5$.

Flow measurements were carried out using planar particle image velocimetry (PIV). A dual-pulse Litron Nd-YAG laser (Nano L200-15 PIV) with a wavelength of 532 nm and maximum power of 200 mJ was used. The flow was seeded with $\sim 1 \mu\text{m}$ smoke droplets, generated by a Martin Magnum 2500 Hz haze generator with Martin Rush & Thrill Haze Fluid. Particle images were captured by two Imager LX 16 mega-pixel cameras with Sigma DG 180 mm lenses, resulting in a FOV of $200 \text{ mm} \times 250 \text{ mm}$ (width \times height) for each camera. The overlap between the two cameras was set to be $\approx 30 \text{ mm}$ which corresponds to 15 % of the FOV. Since the total field of interest was wider, the flow field was measured in three acquisitions with 1000 image pairs each, resulting in a total FOV of $1040 \text{ mm} \times 250 \text{ mm}$ (width \times height). This corresponds to $3.7h$ upstream and downstream of the cubes and $2.5h$ from the floor, which covers the urban canopy layer and a good part of the roughness sublayer. Vector fields were computed with Davis 8.4.0 using multiple passes starting from 96×96 down to 48×48 circular-shaped windows on the final pass with an overlap of 75 %. The nominal vector spacing was 0.75 mm.

The focus in this study is on the aerodynamics of wind turbine performance, thus it is not of interest to calculate the electrical power. This would include electrical losses and depend heavily on the efficiency of the generator (Bastankhah & Porté-Agel, 2017). The quantity of interest is $P_m = Q_s \Omega$, where Q_s is the shaft torque and Ω is the rotational velocity. Furthermore P_m is the sum of the converted power P_c and the friction losses P_f . The performance of a wind turbine can thus be evaluated through measurements of the converted power $P_c = Q_e \Omega$. The electromagnetic torque $Q_e = K_T I$ is directly proportional to the current I through the torque constant K_T , which is a motor property. The friction losses, P_f , can be estimated based on the motor parameters. Thus, it is possible to obtain the mechanical power by measuring the rotational velocity Ω and the current I (Bastankhah & Porté-Agel, 2017; Gambuzza & Ganapathisubramani, 2021). For this, the wind turbine was connected to a brushed DC motor (10NS61 Athlonix) acting as a generator. The current was measured over a 0.1Ω shunt resistor with an INA219 High Side DC Current Sensor. To measure the rotational velocity, a reflective object sensor (OPB705WZ) based on an infrared emitter and a phototransistor was used. This was pointed at the spinning turbine shaft, which was partly made reflective. This way the rotational velocity was identified from the signal of the phototransistor. A high-frequency variable switch (IRF540NPbF) was used to control the current in the circuit, and with that the rotational speed of the turbine. The wind turbine was controlled to run at a tip speed ratio of $\lambda = \Omega R / U = 0.7 \pm 0.08$. This is slightly higher than for $C_{P_{max}}$ but was chosen as it allowed for robust control of the turbine with the present set-up. The literature suggests that a $\lambda = 0.7$ is relatively close to optimal (Akwa et al., 2012; Aliferis et al., 2019).

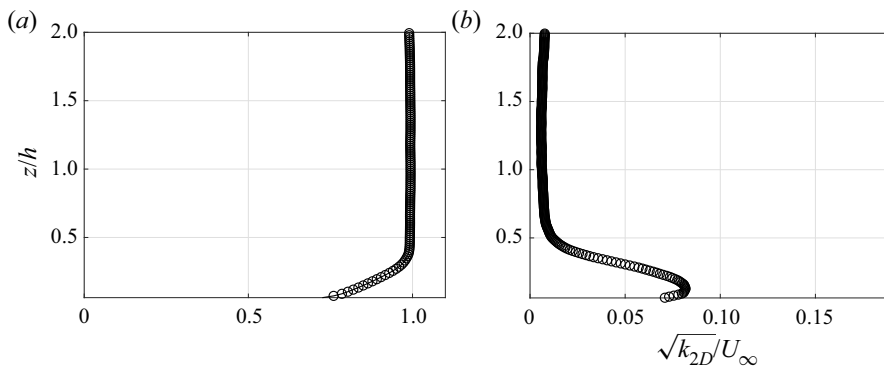


Figure 3. Background profiles of (a) the streamwise velocity and (b) turbulent kinetic energy (two-dimensional) both normalized by U_∞ . Note, these profiles are averaged over $0.2h$ in the streamwise direction $2h$ upstream of the leading edge of the first cube.

3. Flow fields

3.1. Background flow

To generate generic and reproducible results, a flat plate was placed in the homogeneous region of the wind tunnel flow. The background flow was measured on the artificial floor without the cubes at a position that would have been $2h$ upstream of the leading edge of the first cube. The resulting streamwise velocity and two-dimensional turbulent kinetic energy ($k_{2D} = \frac{1}{2}(\overline{u'^2} + \overline{w'^2})$) profiles are shown in figure 3. The boundary layer thickness δ , defined as the point where the velocity reaches 99% of the free stream velocity, is $0.38h$. Both quantities are normalized by the reference velocity U_∞ . In the free stream $\sqrt{k_{2D}}/U_\infty$ is low, with values of 0.7%, and only increases close to the wall. Both U and k_{2D} are uniform outside of the boundary layer.

3.2. Flow fields of cubes without the turbine

An analysis of the flow around the two cubes in tandem formation with a spacing of $2h$ was carried out. This was used to understand the dynamics of the flow in which the turbine was placed. To distinguish the flow fields with and without the turbine, the measured quantities for the cubes without the turbine are denoted with the subscript \cdot_c . Of utmost importance for the evaluation of VAWTs are the wind velocities perpendicular to the axis of rotation, due to their relevance for the available power P_a . The streamwise velocity U_c is shown in figure 4(a). It is normalized with the free stream velocity U_∞ . Velocity vectors of uniform length are overlaid to show the direction of flow. The flow field upstream of the cubes ($x \leq -2h$) is homogeneous with a small turbulent boundary layer on the artificial floor upstream of the cubes. As the flow approaches the first cube it decelerates due to the presence of the cube. A small zone of recirculation forms where the artificial floor and the first cube meet. It is located at $-1 \leq x/h \leq -0.5$ and $0 \leq z/h \leq 0.15$. This was also observed in LDV measurements along the centreline by (Martinuzzi and Havel 2004). Their measurements in the horizontal plane showed that this is part of a horseshoe vortex forming immediately upstream of the first cube. At the top windward edge of the first cube the flow detaches. This leads to a growing recirculation bubble with reverse flow on top of the cube. Above this there is a region where the flow accelerates relative to U_∞ . The flow reattaches on the roof of the second cube with the shear layer impinging on the top windward edge of the second cube. This is in good agreement with results by (Martinuzzi and Havel 2004). In-between the two cubes there is a large area of recirculating flow. The flow rotates clockwise around $x/h \approx 1.27$ and $z/h \approx 1.14$. There is downward flow along the windward side of the second cube, and reverse motion between the cubes and upward flow on the leeward side of the first cube. The upward flow feeds into the recirculation bubble on top

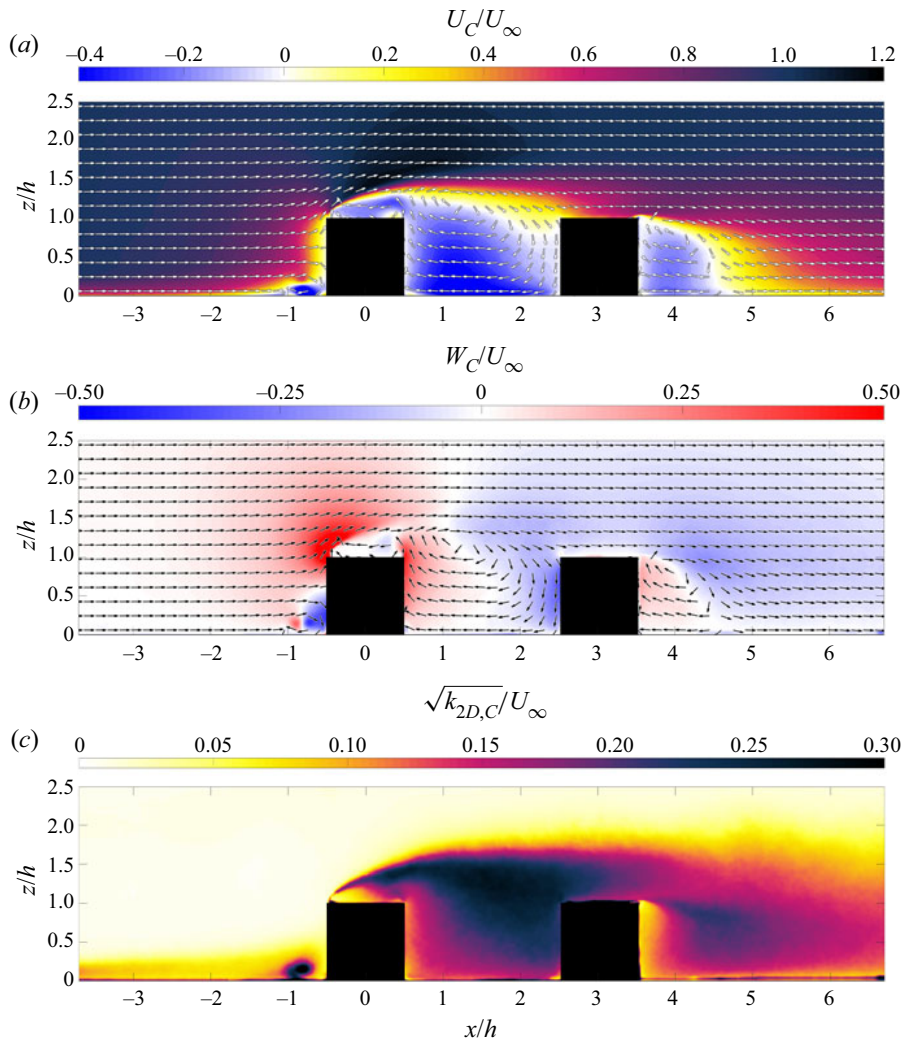


Figure 4. (a) Streamwise velocity, (b) wall-normal velocity and (c) turbulent kinetic energy fields normalized by U_∞ around the cubes without the turbine. Note that only every 20th vector is displayed to avoid clutter and all velocity vectors are scaled to be of uniform length, only representing the direction of flow.

of the first cube. The flow remains attached along the roof of the second cube and detaches only at the trailing edge. Another recirculation zone forms behind the second cube centred around $x/h \approx 4.00$ and $z/h \approx 0.90$.

Figure 4(b) shows the wall-normal velocity field around the cubes. Also, W_C is normalized with the free stream velocity U_∞ . Besides the recirculation zones, there is significant upward motion above the recirculation bubble on top of the first cube, which is dominant around the first cube. This is compensated downstream with predominantly downward motion around the second cube.

There are three regions of increased turbulent kinetic energy. This is illustrated in figure 4(c), showing the k_{2D} -field around the cubes. There is a small region of increased k_{2D} on the artificial floor upstream of the first cube and one associated with flow separation on the leeward edge of the second cube. More importantly for urban wind energy considerations is the large region resulting from flow separation on the windward edge of the first cube. As the recirculation bubble and the high-momentum flow on top

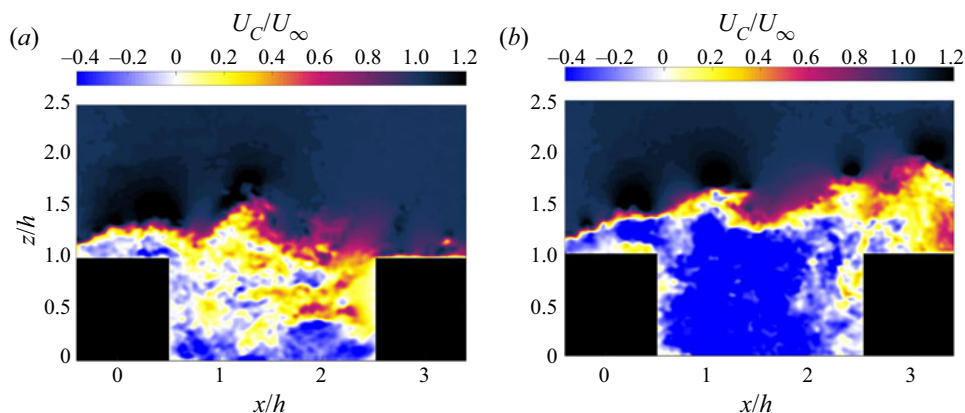


Figure 5. Two examples of the instantaneous streamwise velocity field between the cubes without a turbine in place.

start to mix, $k_{2D,C}$ grows. This leads to a small region of increased turbulence on top of the back of the first cube spanning $1.2 \lesssim z/h \lesssim 1.4$. This grows as more fluid from the top and, as shown by (Martinuzzi and Havel 2004), also from the sides, gets entrained into the recirculation zone between the cubes. As the flow reattaches along the roof of the second cube the turbulence starts to decay again.

To show the level of variability, two exemplary instantaneous streamwise velocity fields focussed on the region between the cubes are plotted in figure 5. It is apparent that the flow field can look significantly different at different instances in time. While the separation on the first cube is relatively constant, farther downstream severe differences in velocity exist. This is illustrated here with velocities locally exceeding U_∞ on the roof of the second cube in one instance in figure 5(a) and very slow, partly recirculating, flow in another instance at the same location in figure 5(b).

3.3. Flow fields with the turbine mounted on cubes

To understand the reciprocal effects between the flow and the wind turbine in this modelled building environment, the turbine was placed at six different positions along the centreline of the cubes (see table 1). At each position the flow field was acquired while measuring the performance of the turbine. The quantities acquired in the presence of the turbine are denoted with the subscript \cdot_T . The flow parameters upstream of the turbine positions are listed in table 1 for the measurements with and without a turbine. They are taken in the wind turbine induction region. That is the region upstream of the turbine, where the flow is affected by the presence of the turbine (Porté-Agel et al., 2020). The flow is examined $0.05d_T$ upstream of the turbine averaged over h_T . An evaluation at different upstream distances from the turbine showed the same trends, making the results qualitatively independent of the upstream distance within a reasonable range. The quantities averaged over h_T are denoted with $\bar{\cdot}$.

Figure 6 shows the streamwise velocity fields U_T/U_∞ for the six turbine positions. A wake behind the turbine can be observed in the flow fields, more prominently on the second cube. Studying this would be interesting for the potential placement of further turbines downstream. However, the focus in this study is on the upstream flow, as this is what influences the turbine performance.

Looking at the velocity vectors, it is apparent that at position 1F, the turbine entrains fluid from below as a result of the upstream blockage of the cube. This effect is increased by the presence of the turbine, which can be seen in table 1 by comparing the average skew angle $\tilde{\gamma}$ upstream of the turbine for the flow field with and without the turbine. Note that $\tilde{\gamma} = 0$ indicates no motion in the wall-normal direction, while positive $\tilde{\gamma}$ -values indicate upward motion. At 1C the turbine is partly submerged in the recirculation bubble caused by the flow separation at the windward edge of the cube. The upper part of the turbine also experiences accelerated flow from above. This effect is increased by the presence of

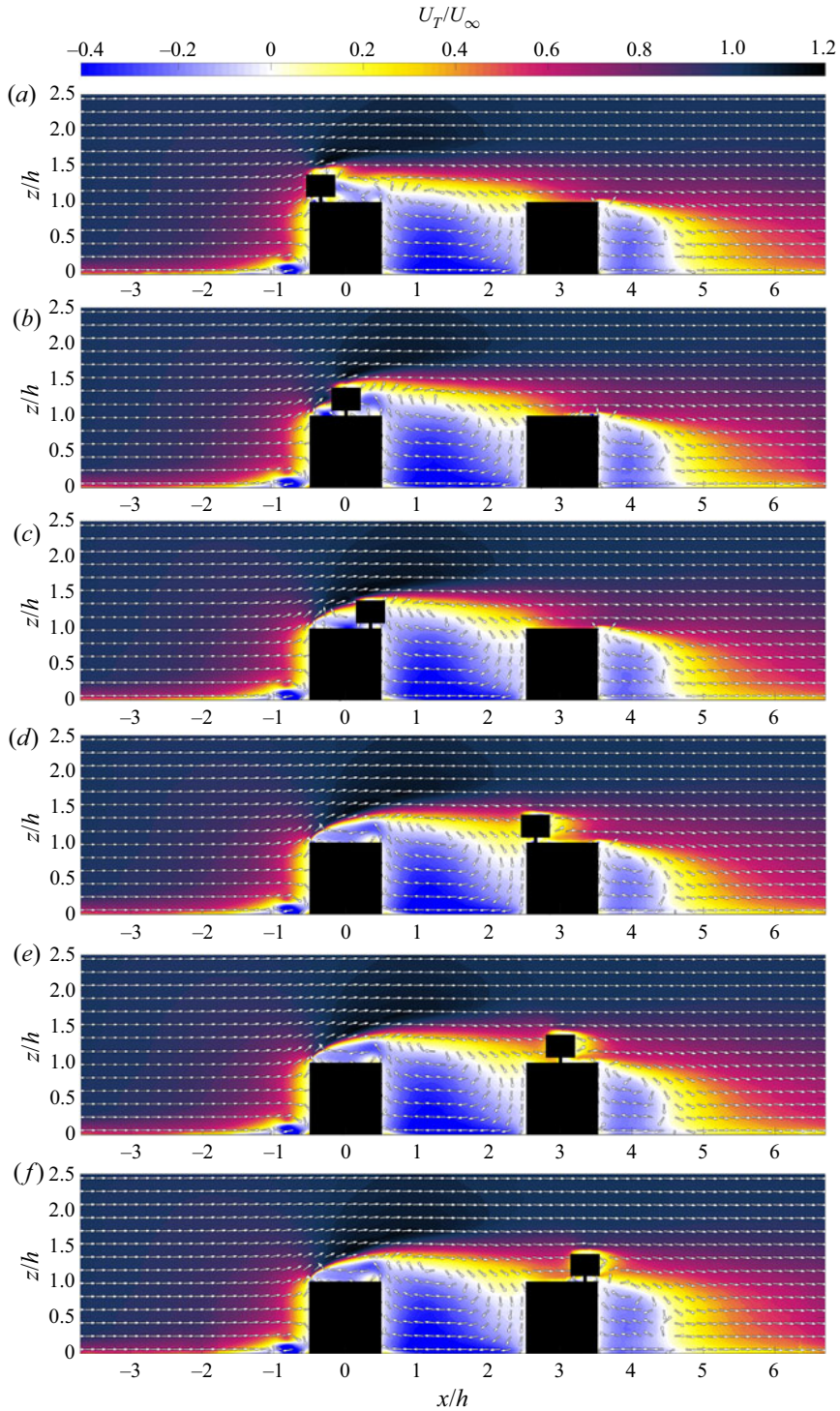


Figure 6. Streamwise velocity fields with the wind turbine mounted at different streamwise positions along the centreline. Note that only every 20th vector is displayed to avoid clutter and all velocity vectors are scaled to be of uniform length, only representing the direction of flow.

Table 1. Flow parameters $0.05d_T$ upstream of the turbine position, averaged over h_T .

Case	Position	x/h	\tilde{U}_C/U_∞ (m s^{-1})	\tilde{U}_T/U_∞ (m s^{-1})	$\tilde{\gamma}_C$ (°)	$\tilde{\gamma}_T$ (°)	$\sqrt{\tilde{k}_{2D,C}}/U_\infty$ (%)	$\sqrt{\tilde{k}_{2D,T}}/U_\infty$ (%)
Cube 1	1F	-0.35	0.78	0.57	32.0	37.6	1.1	7.5
	1C	0.00	0.50	0.57	26.3	11.0	9.0	17.3
	1B	0.35	0.07	0.17	24.1	-23.9	17.8	18.4
Cube 2	2F	2.65	0.43	0.28	-14.2	-30.9	25.9	24.5
	2C	3.00	0.57	0.40	-8.5	-13.3	22.4	20.8
	2B	3.35	0.66	0.43	-5.2	-9.1	19.7	19.0

the turbine, which leads to a decreased $\tilde{\gamma}$. The turbulence intensity $\sqrt{\tilde{k}_{2D,T}}/U_\infty$ is increased by 6.4% and 8.3% for 1F and 1C, respectively. At 1B, the turbine is almost fully submerged in the recirculation zone. It encounters highly turbulent and chaotic flow, illustrated by an average incoming turbulence intensity $\sqrt{\tilde{k}_{2D,T}}/U_\infty$ of 18.9% and strong variations in the skew angle. Only at the very top of the turbine is accelerated fluid entrained. The presence of the turbine only increases the turbulence intensity by $\Delta\sqrt{\tilde{k}_{2D}}/U_\infty = 0.6\%$.

On the second cube the turbine entrains high-speed fluid from the reattaching flow from above. This effect is most prominent at 2F. It is amplified by the presence of the turbine, indicated by increasingly negative $\tilde{\gamma}$ for 2F, 2C and 2B. The flow from above the recirculation bubble is mixed with the wake of the first cube, leading to a significantly reduced magnitude of \tilde{U} compared with U_∞ . Moving downstream on the second cube the flow recovers successively. This results in higher velocities and a reduced $\tilde{\gamma}$ towards the back of the second cube. The presence of the turbine reduces the difference in \tilde{U}/U_∞ and $\sqrt{\tilde{k}_{2D}}/U_\infty$ between 2C and 2B, with the bigger change occurring from 2F to 2C. In general, the presence of the turbine slightly decreases the high turbulence intensities experienced on cube 2 by $0.7\% \leq \Delta\sqrt{\tilde{k}_{2D}}/U_\infty \leq 1.6\%$.

To illustrate further how the wind turbine changes the flow field at the different positions a differential velocity field $\Delta U/U_\infty$ generated by subtracting the velocity field of the empty cubes is plotted in figure 7; $\Delta U = U_T - U_C$, where U_T is the streamwise velocity field including the turbine and U_C is the streamwise velocity field of the empty cubes. Here, U_∞ is taken from the velocity field without the turbine. At positions 1F and 1C the turbine is placed in flow with a significant upward velocity component, as illustrated by figure 4(b), the velocity vectors in figure 6(a,b) and the skew angles in table 1. This creates an upwards deflected wake behind the turbine, visible in figure 7(a,b). At 1F the turbine also accelerates the flow below its wake, due to the disturbance of the recirculation bubble on top of the first cube. The turbine at 1B does not have a significant wake downstream of the turbine, due to the low velocities upstream of it. The turbine wake grows in magnitude and size with increasing downstream position on the second cube, as the flow upstream recovers. Detailed descriptions of VAWT wake characteristics can be found in Shamsoddin and Porté-Agel (2014), Rolin and Porté-Agel (2018) and Shamsoddin and Porté-Agel (2020).

More important for the turbine performance is the flow upstream of the turbine and this study reveals contrasting effects depending on the turbine position. At 1F the turbine shows a classical upstream blockage effect, where the streamwise velocity is slowed down by the presence of the turbine. It experiences a 27.5% lower velocity than the flow field on the empty cubes would suggest. While the turbine at position 1B generates a similar upstream blockage at the top of the blade, overall the turbines at positions 1B and 1C have the opposite effect on the flow immediately upstream. Both turbines are partly placed in the recirculation bubble on top of the first cube. By virtue of obstructing the dominant reverse flow in this region, their presence causes more high-momentum fluid to enter the turbine area.

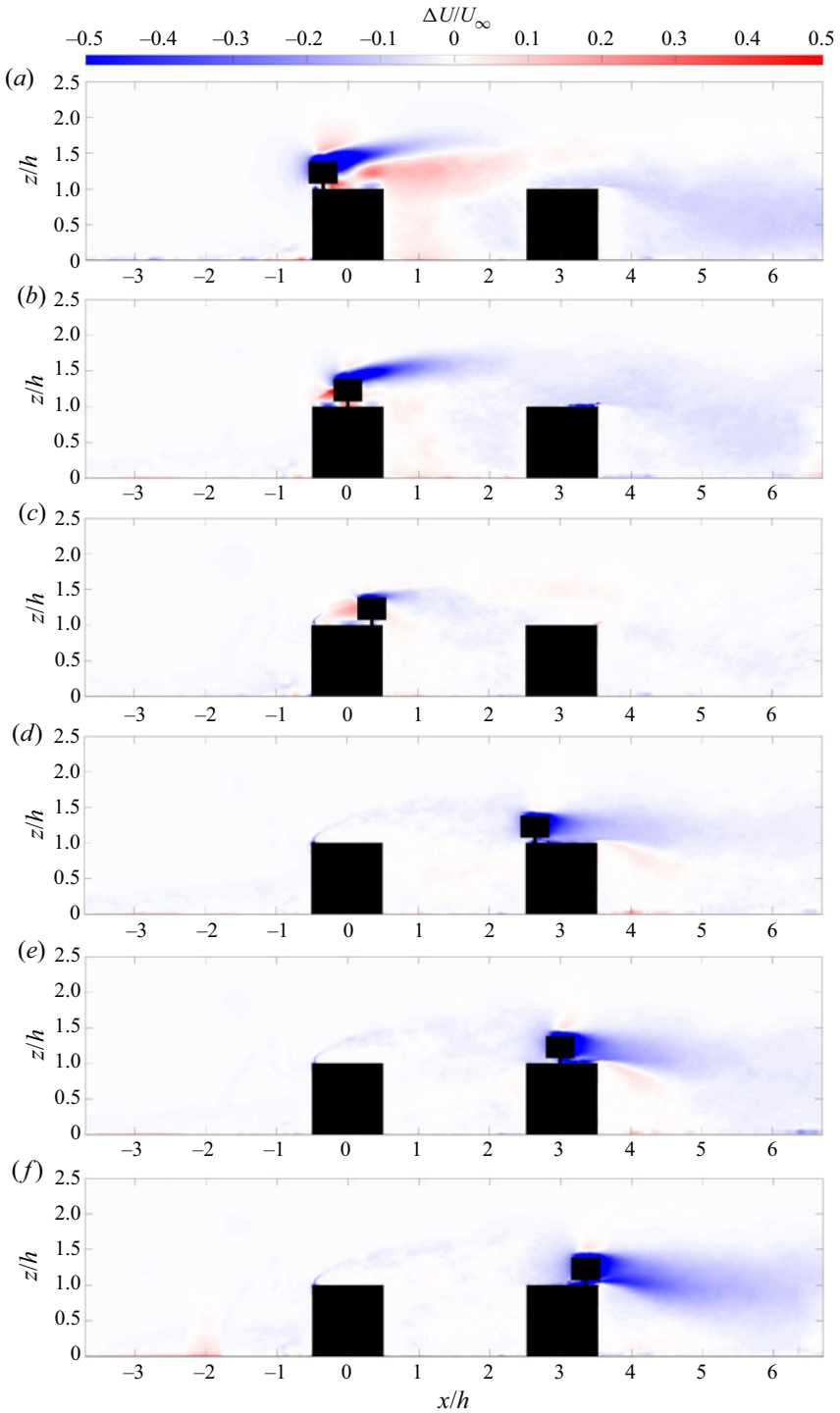


Figure 7. Velocity difference caused by the presence of the wind turbine at different streamwise positions along the centreline.

This leads to a relative velocity surplus upstream of the turbines of 14.6 % and 132 % for 1C and 1B, respectively (table 1). This is a result that shows an impact of the turbine on the flow field that goes beyond established wind turbine blockage effects. Note the extreme relative increase on the back position is due to a very low \tilde{U}_C here. The trend is clear for both positions.

The turbines on the second cube again show more classical behaviour, causing an upstream blockage that slows down the flow by 30 % to 35 %. The flow is less skewed but more turbulent than on cube 1, which leads to enhanced deceleration of the flow upstream of the turbine. To determine the influence of those two factors rigorously would require a separate examination in a different set-up, which is outside the present scope and left for future investigations.

A more detailed analysis of the inflow at the turbine positions is shown in figure 8, where the histograms of the streamwise velocity along the blade height of the turbine h_T , $0.05d_T$ upstream of the turbine are plotted. This is compared for the flow field U_C without a turbine and for the flow fields U_T including the turbine at various positions. It is apparent that the wind turbine encounters a wide range of inflow at the different turbine positions. The velocity profile is sheared at all positions, with strong gradients at positions 1C and 1B (figure 8*b,c,e,f*). The turbulent fluctuations increase on the first cube when moving the turbine downstream, indicated by wider histograms throughout h_T , while they decrease on cube 2, where the fluctuations are higher overall. The impact of the turbine on the incoming flow is visible at all positions, but is more prominent on the first cube. This is likely due to the fact that it is placed partly in a region of separating flow with high velocity gradients, whereas on cube 2 a recovering wake dominates, which is already a highly turbulent flow. At position 1F (figure 8*a,d*), the inflow without the turbine present is characterized by a low turbulence intensity $\sqrt{k_{2D,C}}/U_\infty = 1.1\%$, indicated by a narrow histogram. The presence of the turbine reduces the streamwise velocity, most significantly in the centre, with the histograms showing large tails towards low velocities. This is also partly observed at the top of the turbine for 1C (figure 8*b,e*). Below that, the region of high shear is stretched and pushed down towards the lower part of the turbine. Here it replaces a low speed region, leading to an overall surplus of velocity compared with the case without the turbine. At 1B (figure 8*c,f*) the shear region is stretched similarly, diminishing the region of predominantly negative velocities. On the second cube the shape of the velocity profiles and width of the histograms do not change much in the presence of the turbine. The inflow is already highly turbulent with only a small gradient from top to bottom. A slight deficit around $z/h_T = 0$ caused by the turbine can be observed, most prominent for position 2B (figure 8*i,l*). Overall the velocity is decreased on cube 2 for all positions, visible in the superimposed mean velocity profiles in figure 8. It is evident that the presence of the turbine has a significant impact on the flow phenomena across the system beyond blockage effects, which would result in significantly different power output from the real arrangement compared with predictions based off the system without the turbine alone. This is explicitly demonstrated in the next section.

4. Wind turbine performance

The converted power was measured as described in § 2. Based on this the mechanical power the wind turbine produced was calculated, considering the friction losses. In such a manner, P_m was evaluated for the six different locations. The goal of this study was not to evaluate how well the wind turbine performs but rather to compare different wind turbine positions on a modelled building environment. To do this the power coefficient $C_P = P_m / (\frac{1}{2}\rho U_\infty^3 A)$ was calculated based on the incoming velocity U_∞ upstream of the cubes; C_P is listed in table 2 along with the other performance parameters such as λ , P_m , P_c and P_f . The control of the tip speed ratio was fixed between different measurement positions leading to slight variations between 0.62 and 0.78. The values are in line with expected values for Savonius-type turbines (Akwa et al., 2012; Aliferis et al., 2019).

The available power at the turbine positions is expressed through a power coefficient of the available power $C_{P_a} = (1/2)\rho\tilde{U}^3 A / (1/2)\rho U_\infty^3 A = \tilde{U}^3 / U_\infty^3$, in order to represent it in non-dimensional form. Figure 9 shows C_P at the different turbine positions in comparison with C_{P_a} , based on the measured

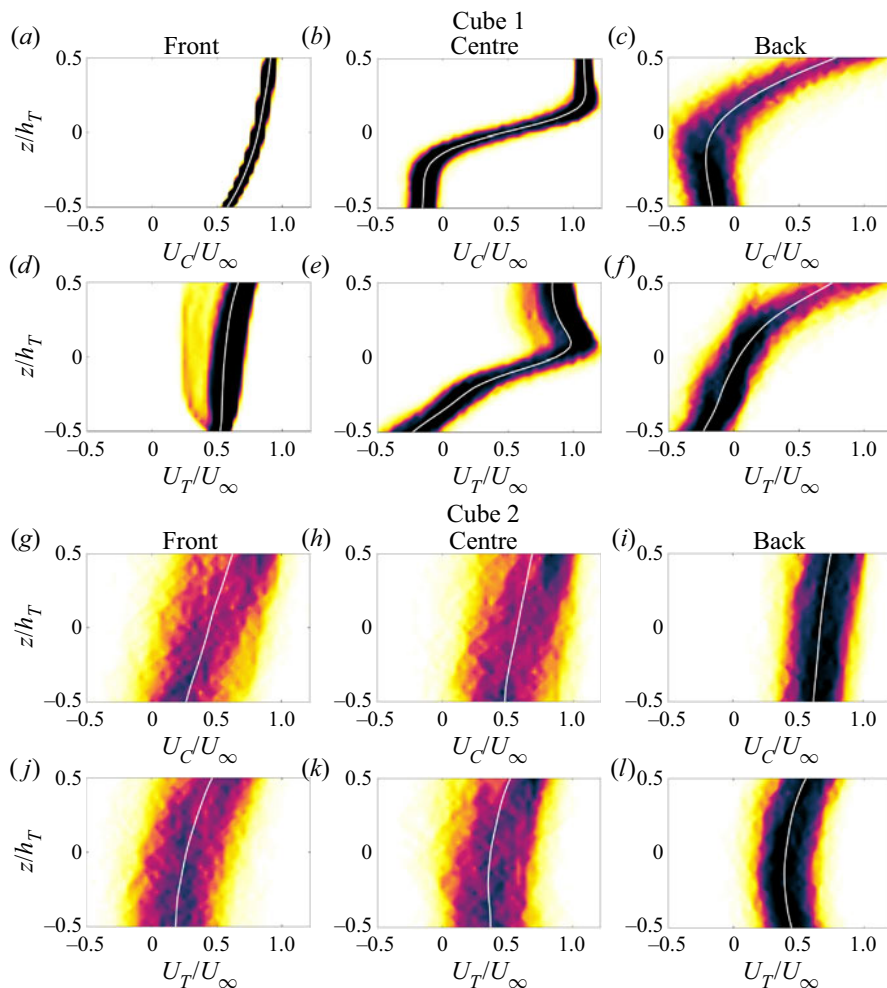


Figure 8. Histograms of streamwise velocity U along the turbine blade immediately ($0.05d_T$) upstream of the turbine from the flow fields without ((a–c) and (g–i)) and with the turbine ((d–f) and (j–l)). Mean velocity profiles superimposed as white lines.

velocities \tilde{U} at these locations for the set-up with and without the turbine. Maximum uncertainties for C_P and C_{P_a} of 8.8 % and 3.5 %, respectively, are plotted for all cases. As shown by (Akwa et al. 2012) C_P values for Savonius turbines are generally low compared with HAWT and very dependent on Reynolds number. From $Re_{d_T} = 280\,000$ to $Re_{d_T} = 140\,000$ they report a reduction of C_P from 0.17 to 0.13. In the present study Re_{d_T} is almost an order of magnitude smaller at $Re_{d_T} = 32\,000$, thus explaining the low C_P values observed here. Of the positions tested, C_P is at a maximum for the positions 1F and 1C, with a significant reduction in power as one moves towards the back of the cube (1B). On the second cube the extracted power increases with streamwise position. The turbine performance on cube 2 is higher at all positions compared with 1B but always remains below 1F and 1C. This suggests the outside positions, farthest away from the other building to be ideal in this configuration with one of the buildings directly downstream of the other and no other substantial obstructions in close proximity. However, the performance difference between this location and the centre of the cubes is small. Considering varying wind directions in reality and potentially multiple neighbouring buildings, the centre position offers a good balance of robustness and performance.

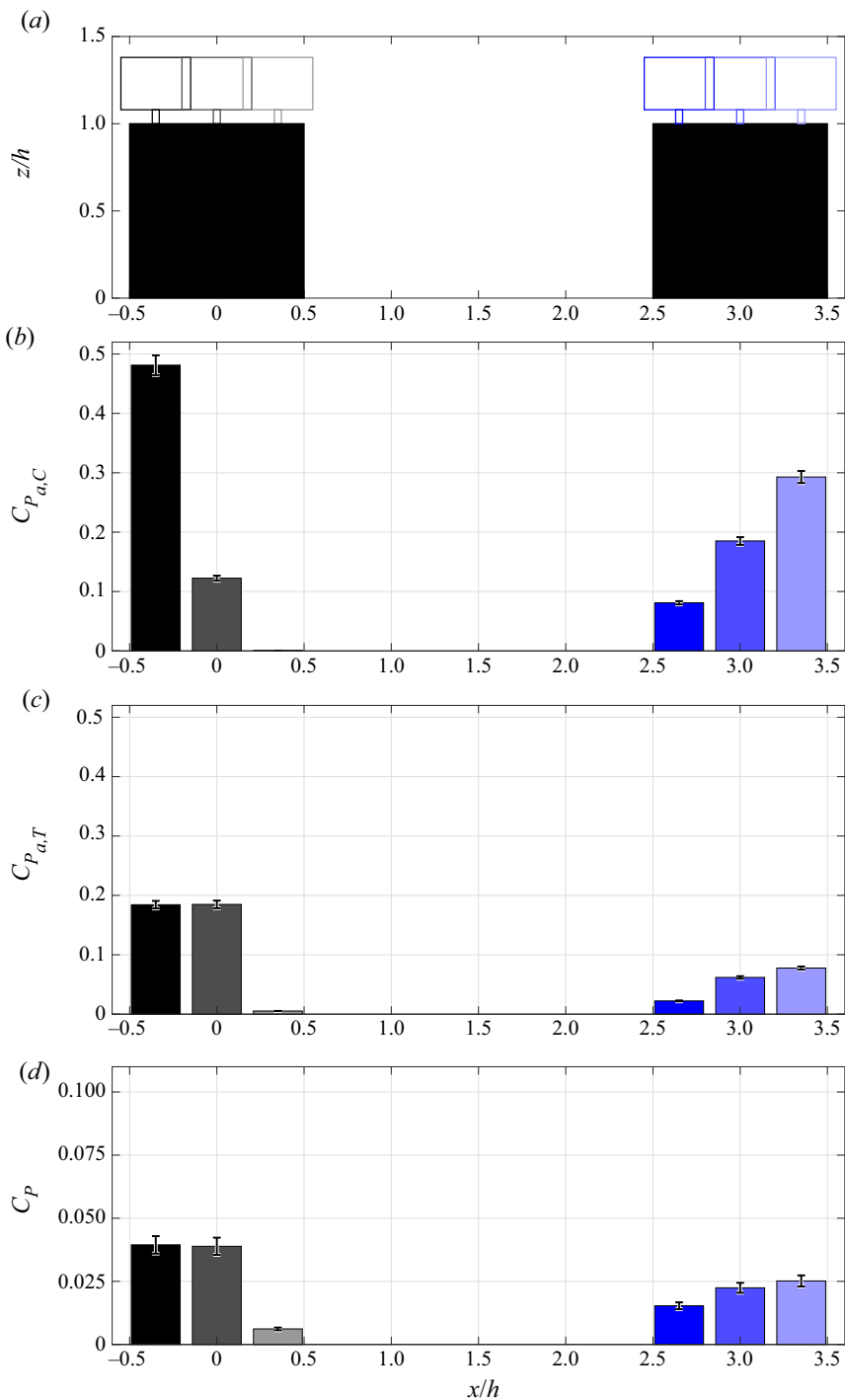


Figure 9. Analysis of the wind turbine performance at different positions based on the available power with and without the turbine ($C_{P_{a,T}}$ and $C_{P_{a,C}}$) and the measured mechanical power (C_P). Uncertainty bars based on propagation of uncertainty of all contributing variables.

Table 2. Wind turbine performance parameters. C_P is calculated based on P_m .

	Position	x/h	λ	P_m (mW)	P_c (mW)	P_f (mW)	C_P	Color
Cube 1	1F	0.15	0.62	24.0	19.8	4.2	0.040	■
	1C	0.50	0.62	23.7	19.5	4.3	0.039	■
	1B	0.85	0.67	3.7	2.3	1.4	0.006	■
Cube 2	2F	0.15	0.78	9.4	6.7	2.7	0.015	■
	2C	0.50	0.68	13.7	10.4	3.2	0.022	■
	2B	0.85	0.66	15.3	11.9	3.4	0.025	■

It is apparent that the available power measured in the presence of the turbine $C_{P_{a,T}}$ shows a much better correlation with the measured performance compared with that predicted from the flow field alone. The correlation coefficient $r(C_P, C_{P_{a,T}}) = \text{cov}(C_P, C_{P_{a,T}}) / \sigma_{C_P} \sigma_{C_{P_{a,T}}}$ is 97.7%. Considering only the flow field around the empty cubes leads to deviations in the estimated available power $C_{P_{a,C}}$. The gap between the estimated available power at positions 1F and 1C is significantly overestimated. $C_{P_{a,C}}$ at 2C and 2B exceed $C_{P_{a,C}}$ at 1C, which contrasts with the measured power output (see P_m and C_P in table 2). The correlation coefficient $r(C_P, C_{P_{a,C}})$ is only 70.7%. The reason for this discrepancy between $C_{P_{a,C}}$ and $C_{P_{a,T}}$, and the resulting C_P is the influence the wind turbine has on the flow field (see § 3.3). At position 1F and for all turbine positions on cube 2 C_{P_a} is negatively affected by the presence of the turbine, whereas at positions 1C and 1B C_{P_a} is increased by adding the turbine. These diverging trends lead to significantly different power estimates when considering only the flow field around the empty cubes.

5. Conclusions

The wind resources for two model buildings in tandem formation were evaluated using a combination of flow field and performance measurements. A VAWT of the Savonius (drag) type was placed at six different streamwise locations along the centreline of the roofs of the two buildings. It was shown that the presence of the turbine substantially influences the flow field and the power production. This extends beyond established wind turbine blockage effects previously reported in the literature. An analysis of the available power based only on the flow field around the cubes at the supposed turbine location, but without the turbine, would change the conclusions significantly. The available power calculated from the flow field in the presence of the turbine was found to correlate well with the power produced by the turbine at the various positions. The trends from front to back position differed between the first and second cube. The highest power was measured at the front and centre position of the first cube with a large reduction towards the back of cube 1. On the second cube the power production was found to increase gradually from front to back, with values in-between the extremes measured on the first cube. On the first cube the separation of the flow at the windward edge was the dominant flow pattern. The presence of the turbine diminished the recirculation zone on top of the cube and thus increased the available power at the centre and back position. At the front position the turbine affected the available power negatively due to upstream blockage effects and increased turbulent fluctuations. The second cube experienced a recovering wake from cube 1, which led to increasing power production with increasing distance from the upstream cube. Similarly to the front position on cube 1, the power production was diminished by the presence of the turbine, due to its upstream blockage effect.

It has to be noted that these conclusions are specifically for the present set-up and size ratios. However, the observed effects are expected to remain relevant in different configurations with similar size ratios. Future studies should investigate the influence of the size ratios of turbine to building d_T/h and h_T/h , the distance between the buildings s/h as well as the influence of a staggered arrangement, the wind

direction and the influence of incoming turbulence. Nonetheless, the results provided here suggest that in this specific configuration the ideal position of the turbine is on the outer edge of the buildings, farthest from the other building. More generally, the central positions on both buildings offer a good compromise between performance and robustness to the possibility of adjacent buildings and variations in incoming flow angle.

Supplementary Material. Supplementary material are available at <https://doi.org/10.1017/flo.2022.3>.

Declaration of Interest. The authors report no conflict of interest.

Funding Statement. This research received no specific grant from any funding agency, commercial or not-for-profit sectors.

Author Contributions. Y.J., T.B. and R.J.H. created the research plan. Y.J. and R.B. designed and built the set-up and conducted all experiments. Y.J. performed the analysis and wrote the manuscript. All authors contributed to the editing of the manuscript.

Data Availability Statement. See supplementary material.

Ethical Standards. The research meets all ethical guidelines, including adherence to the legal requirements of the study country.

References

- Abohela, I., Hamza, N., & Dudek, S. (2013). Effect of roof shape, wind direction, building height and urban configuration on the energy yield and positioning of roof mounted wind turbines. *Renewable Energy*, *50*, 1106–1118.
- Akwa, J. V., Vielmo, H. A., & Petry, A. P. (2012). A review on the performance of Savonius wind turbines. *Renewable and Sustainable Energy Reviews*, *16*(5), 3054–3064.
- Al-Quraan, A., Stathopoulos, T., & Pillay, P. (2016). Comparison of wind tunnel and on site measurements for urban wind energy estimation of potential yield. *Journal of Wind Engineering and Industrial Aerodynamics*, *158*, 1–10.
- Aliferis, A. D., Jessen, M. S., Bracchi, T., & Hearst, R. J. (2019). Performance and wake of a Savonius vertical-axis wind turbine under different incoming conditions. *Wind Energy*, *22*(9), 1260–1273.
- Bastankhah, M., & Porté-Agel, F. (2017). A new miniature wind turbine for wind tunnel experiments. Part I: Design and performance. *Energies*, *10*(7), 908.
- Bazilevs, Y., Korobenko, A., Deng, X., Yan, J., Kinzel, M., & Dabiri, J. O. (2014). Fluid–structure interaction modeling of vertical-axis wind turbines. *Journal of Applied Mechanics*, *81*(8), 081006.
- Brownstein, I. D., Kinzel, M., & Dabiri, J. O. (2016). Performance enhancement of downstream vertical-axis wind turbines. *Journal of Renewable and Sustainable Energy*, *8*(5), 053306.
- Castro, I. P., & Robins, A. G. (1977). The flow around a surface-mounted cube in uniform and turbulent streams. *Journal of Fluid Mechanics*, *79*(2), 307–335.
- Cheng, H., & Castro, I. P. (2002). Near wall flow over urban-like roughness. *Boundary-Layer Meteorology*, *104*(2), 229–259.
- Cheng, Y., Lien, F. S., Yee, E., & Sinclair, R. (2003). A comparison of large Eddy simulations with a standard $k-\epsilon$ Reynolds-averaged Navier–Stokes model for the prediction of a fully developed turbulent flow over a matrix of cubes. *Journal of Wind Engineering and Industrial Aerodynamics*, *91*(11), 1301–1328.
- Chicco, G., & Mancarella, P. (2009). Distributed multi-generation: A comprehensive view. *Renewable and Sustainable Energy Reviews*, *13*(3), 535–551.
- Dabiri, J. O. (2011). Potential order-of-magnitude enhancement of wind farm power density via counter-rotating vertical-axis wind turbine arrays. *Journal of Renewable and Sustainable Energy*, *3*(4), 043104.
- Danao, L. A., Eboibi, O., & Howell, R. (2013). An experimental investigation into the influence of unsteady wind on the performance of a vertical axis wind turbine. *Applied Energy*, *107*, 403–411.
- Ferreira, M. A., & Ganapathisubramani, B. (2021). Scale interactions in velocity and pressure within a turbulent boundary layer developing over a staggered-cube array. *Journal of Fluid Mechanics*, *910*, A48.
- Fuka, V., Xie, Z.-T., Castro, I. P., Hayden, P., Carpentieri, M., & Robins, A. G. (2018). Scalar fluxes near a tall building in an aligned array of rectangular buildings. *Boundary-Layer Meteorology*, *167*(1), 53–76.
- Gambuzza, S., & Ganapathisubramani, B. (2021). The effects of free-stream turbulence on the performance of a model wind turbine. *Journal of Renewable and Sustainable Energy*, *13*(2), 023304.
- Ge, M., Gayme, D. F., & Meneveau, C. (2021). Large-eddy simulation of wind turbines immersed in the wake of a cube-shaped building. *Renewable Energy*, *163*, 1063–1077.
- Glumac, A.Š., Hemida, H., & Höffer, R. (2018). Wind energy potential above a high-rise building influenced by neighboring buildings: An experimental investigation. *Journal of Wind Engineering and Industrial Aerodynamics*, *175*, 32–42.
- Hearst, R. J., Gomit, G., & Ganapathisubramani, B. (2016). Effect of turbulence on the wake of a wall-mounted cube. *Journal of Fluid Mechanics*, *804*, 513–530.
- Hemida, H., Glumac, A.Š., Vita, G., Kostadinović Vranešević, K., & Höffer, R. (2020). On the flow over high-rise building for wind energy harvesting: An experimental investigation of wind speed and surface pressure. *Applied Sciences*, *10*(15), 5283.

- Hui, I., Cain, B. E., & Dabiri, J. O. (2018). Public receptiveness of vertical axis wind turbines. *Energy Policy*, 112, 258–271.
- International Energy Agency (IEA) (2020). *World energy outlook 2020 – analysis*. Paris, France: OECD Publishing.
- Kalmikov, A., Dupont, G., Dykes, K., & Chan, C. (2010). Wind power resource assessment in complex urban environments: MIT campus case-study using CFD analysis. In *AWEA 2010 Windpower Conference, Dallas, USA, May 2010*.
- Kc, A., Whale, J., & Urmee, T. (2019). Urban wind conditions and small wind turbines in the built environment: A review. *Renewable Energy*, 131, 268–283.
- Kinzel, M., Mulligan, Q., & Dabiri, J. O. (2012). Energy exchange in an array of vertical-axis wind turbines. *Journal of Turbulence*, 13, N38.
- Kooiman, S., & Tullis, S. (2010). Response of a vertical axis wind turbine to time varying wind conditions found within the urban environment. *Wind Engineering*, 34(4), 389–401.
- Kumburnuss, J., Chen, J., Yang, H. X., & Lu, L. (2012). Investigation into the relationship of the overlap ratio and shift angle of double stage three bladed vertical axis wind turbine (VAWT). *Journal of Wind Engineering and Industrial Aerodynamics*, 107-108, 57–75.
- Ledo, L., Kosasih, P. B., & Cooper, P. (2011). Roof mounting site analysis for micro-wind turbines. *Renewable Energy*, 36(5), 1379–1391.
- Li, D., Wang, S., & Yuan, P. (2010). A review of micro wind turbines in the built environment. In *2010 Asia-Pacific Power and Energy Engineering Conference*, pp. 1–4. Chengdu, China: Institute of Electrical and Electronics Engineers (IEEE). ISSN: 2157-4847.
- Loganathan, B., Mustary, I., Chowdhury, H., & Alam, F. (2017). Effect of turbulence on a savonius type micro wind turbine. *Energy Procedia*, 110, 549–554.
- Lu, L., & Ip, K. Y. (2009). Investigation on the feasibility and enhancement methods of wind power utilization in high-rise buildings of Hong Kong. *Renewable and Sustainable Energy Reviews*, 13(2), 450–461.
- Martinuzzi, R. J., & Havel, B. (2000). Turbulent flow around two interfering surface-mounted cubic obstacles in tandem arrangement. *Journal of Fluids Engineering*, 122(1), 24.
- Martinuzzi, R. J., & Havel, B. (2004). Vortex shedding from two surface-mounted cubes in tandem. *International Journal of Heat and Fluid Flow*, 25(3), 364–372.
- Medici, D., Ivanell, S., Dahlberg, J.-A., & Alfredsson, P. H. (2011). The upstream flow of a wind turbine: Blockage effect. *Wind Energy*, 14(5), 691–697.
- Meinders, E. R., & Hanjalić, K. (1999). Vortex structure and heat transfer in turbulent flow over a wall-mounted matrix of cubes. *International Journal of Heat and Fluid Flow*, 20(3), 255–267.
- Mertens, S. (2003). The energy yield of roof mounted wind turbines. *Wind Engineering*, 27(6), 507–518.
- Millward-Hopkins, J. T., Tomlin, A. S., Ma, L., Ingham, D., & Pourkashanian, M. (2012). The predictability of above roof wind resource in the urban roughness sublayer. *Wind Energy*, 15(2), 225–243.
- Musial, W., & Ram, B. (2010). *Large-scale offshore wind power in the United States: Assessment of opportunities and barriers* (Technical report). Springfield, USA: U.S. Department of Commerce National Technical Information Service.
- Oke, T. R. (1976). The distinction between canopy and boundary-layer urban heat islands. *Atmosphere*, 14(4), 268–277.
- Oke, T. (1988). The urban energy balance. *Progress in Physical Geography: Earth and Environment*, 12(4), 471–508.
- Pagnini, L. C., Burlando, M., & Repetto, M. P. (2015). Experimental power curve of small-size wind turbines in turbulent urban environment. *Applied Energy*, 154, 112–121.
- Pellegrini, M., Guzzini, A., & Saccani, C. (2021). Experimental measurements of the performance of a micro-wind turbine located in an urban area. *Energy Reports*, 7, 3922–3934.
- Porté-Agel, F., Bastankhah, M., & Shamsoddin, S. (2020). Wind-turbine and wind-farm flows: A review. *Boundary-Layer Meteorology*, 174(1), 1–59.
- Raupach, M. R., Antonia, R. A., & Rajagopalan, S. (1991). Rough-wall turbulent boundary layers. *Applied Mechanics Reviews*, 44(1), 1–25.
- Rolin, V. F. -C., & Porté-Agel, F. (2018). Experimental investigation of vertical-axis wind-turbine wakes in boundary layer flow. *Renewable Energy*, 118, 1–13.
- Scheurich, F., & Brown, R. E. (2013). Modelling the aerodynamics of vertical-axis wind turbines in unsteady wind conditions. *Wind Energy*, 16(1), 91–107.
- Shamsoddin, S., & Porté-Agel, F. (2014). Large eddy simulation of vertical axis wind turbine wakes. *Energies*, 7(2), 890–912.
- Shamsoddin, S., & Porté-Agel, F. (2020). Effect of aspect ratio on vertical-axis wind turbine wakes. *Journal of Fluid Mechanics*, 889, R1.
- Simley, E., Angelou, N., Mikkelsen, T., Sjöholm, M., Mann, J., & Pao, L. Y. (2016). Characterization of wind velocities in the upstream induction zone of a wind turbine using scanning continuous-wave lidars. *Journal of Renewable and Sustainable Energy*, 8(1), 013301.
- Stathopoulos, T., Alrawashdeh, H., Al-Quraan, A., Blocken, B., Dilimulati, A., Paraschivoiu, M., & Pilay, P. (2018). Urban wind energy: Some views on potential and challenges. *Journal of Wind Engineering and Industrial Aerodynamics*, 179, 146–157.
- Toja-Silva, F., Peralta, C., Lopez-Garcia, O., Navarro, J., & Cruz, I. (2015). On roof geometry for urban wind energy exploitation in high-rise buildings. *Computation*, 3(2), 299–325.
- Vita, G., Glumac, A.Š., Hemida, H., Salvadori, S., & Baniotopoulos, C. (2020). On the wind energy resource above high-rise buildings. *Energies*, 13(14), 3641.

- Wang, L., Li, D., Gao, Z., Sun, T., Guo, X., & Bou-Zeid, E. (2014). Turbulent transport of momentum and scalars above an urban canopy. *Boundary-Layer Meteorology*, *150*(3), 485–511.
- Wekesa, D. W., Wang, C., Wei, Y., & Zhu, W. (2016). Experimental and numerical study of turbulence effect on aerodynamic performance of a small-scale vertical axis wind turbine. *Journal of Wind Engineering and Industrial Aerodynamics*, *157*, 1–14.
- West, G. S., & Apelt, C. J. (1982). The effects of tunnel blockage and aspect ratio on the mean flow past a circular cylinder with Reynolds numbers between 104 and 105. *Journal of Fluid Mechanics*, *114*, 361–377.
- Xie, Z., & Castro, I. P. (2006). LES and RANS for turbulent flow over arrays of wall-mounted obstacles. *Flow, Turbulence and Combustion*, *76*(3), 291.
- Xie, Z.-T., Coceal, O., & Castro, I. P. (2008). Large-eddy simulation of flows over random urban-like obstacles. *Boundary-Layer Meteorology*, *129*(1), 1.
- Yakhot, A., Liu, H., & Nikitin, N. (2006). Turbulent flow around a wall-mounted cube: A direct numerical simulation. *International Journal of Heat and Fluid Flow*, *27*(6), 994–1009.
- Yan, S., Shi, S., Chen, X., Wang, X., Mao, L., & Liu, X. (2018). Numerical simulations of flow interactions between steep hill terrain and large scale wind turbine. *Energy*, *151*, 740–747.
- Yang, A.-S., Su, Y.-M., Wen, C.-Y., Juan, Y.-H., Wang, W.-S., & Cheng, C.-H. (2016). Estimation of wind power generation in dense urban area. *Applied Energy*, *171*, 213–230.

**Influence of position and wind
direction on the performance of a
roof-mounted vertical axis wind
turbine**

Yannick Jooss, Eivind Berg Rønning, R. Jason Hearst, Tania Bracchi

*Under consideration for publication in:
Journal of Wind Engineering & Industrial Aerodynamics.*

This article is awaiting publication and is not included in NTNU Open

Influence of incoming turbulence and shear on the flow field and performance of a lab-scale roof-mounted vertical axis wind turbine

Yannick Jooss, R. Jason Hearst, Tania Bracchi

*Under consideration for publication in:
Wind Energy.*

This article is awaiting publication and is not included in NTNU Open

